Abstract

Jet measurements in pp and Pb–Pb collisions in ALICE

Rongrong Ma

2014

Lattice-QCD predicts the existence of a new form of hot, dense matter called the Quark Gluon Plasma (QGP) above a critical energy density. Such matter is believed to be created in relativistic heavy-ion collisions, where sufficient energy is expected to be deposited by colliding ions in a limited volume. To study the properties of the QGP, high transverse momentum (p_{T}) partons produced at the early stage of the collisions are used as probes. Since partons are not directly measurable, jet reconstruction, which assembles the hadron fragments of a parton into a "jet", provides an experimental tool to reconstruct the parton kinematics. When traversing the colored medium, partons lose energy via both induced gluon radiation and elastic scatterings. Consequently jet structure is modified relative to jets generated in vacuum. The inclusive differential jet cross section in pp collisions at $\sqrt{s} =$ 2.76 TeV is measured, which serves as a reference for jet measurements in Pb–Pb collisions at the same $\sqrt{s_{\mathrm{NN}}}$. Two jet cone radii are used to reconstruct jets, and the ratio of the cross sections is formed. The good agreement between these results and perturbative QCD calculations at Next-to-Leading Order confirms the validity of the theoretical calculations in a new energy regime. Performing the same analysis in Pb–Pb collisions is challenging because of the large background. Therefore, a novel approach using the difference of the jet distributions recoiling from trigger hadrons in two disjoint p_{T} intervals is developed to remove the contribution of background jets. In this thesis, azimuthal correlations between trigger hadrons and recoil jets are studied, and seen to remain essentially the same in pp and Pb–Pb collisions, implying that jets are not further deflected in the medium. These results are consistent with radiating multiple relatively soft (low p_{T}) gluons instead of a single hard (high p_{T}) one as the preferred way for partons to lose energy in the medium.

Jet measurements in pp and Pb–Pb collisions in ALICE

A Dissertation

Presented to the Faculty of the Graduate School

of

Yale University

in Candidacy for the Degree of

Doctor of Philosophy

By

Rongrong Ma

Dissertation Director: John Harris

May 2014

Acknowledgements

First to my parents, who have been there with me all along the way. You have been supportive of every choice I have made, and forgiving of every mistake I have made. I really appreciate the freedom you have given me to choose the life I want to live. I would never be able to achieve what I have today if you were not there. Most thanks to my wife Fanli, who enlightened up my life. Marrying you was the best luck I ever had, and since then my heart has a home. Thanks very much for making a colorful life in the family. There will be ups and downs in the future, but your company is my source of strength and determination. My daughter Dorothy was born during the preparation of this thesis. You are the most precious gift I have even received. You have brought so much joy and laughter to the family, and made me the happiest father in the world. I will always miss the time when you sleep like an angel in my arms. I want to express my very special thanks to the RHI group at Yale. To this day, I have felt very lucky to have chosen to join this productive, creative, and extremely friendly group when I first came to Yale. It has been the best five and half years of my life being part of the group. Many thanks to John and Helen, from whom I have learnt so much both academically and socially. You are always a model for my career, and it was my great honor to be your student. Last but not least, to Peter with whom I have worked very closely during my Ph.D. study. Your enthusiasm in research has inspired me and your adventurous, yet rigorous, attitude towards science is the quality I will insist on throughout my career.

Contents

List of Figures

List of Tables

1 Introduction

The theory of strong interactions, Quantum ChromoDynamics (QCD) [1], predicts a phase transition between confined hadronic matter and a deconfined state of matter, the Quark Gluon Plasma (QGP), when the relevant scale of the system becomes much smaller than the range of the strong force. In this regime of asymptotic freedom, quarks and gluons are not confined in color-neutral objects and become the relevant degrees of freedom for the QGP. This phase transition is illustrated in a QCD phase diagram shown in Fig. 1, where the x-axis is the baryon chemical potential (μ_{B}) and the y-axis is the temperature of the QCD matter [2]. It suggests that the phase transition can be triggered by either compressing

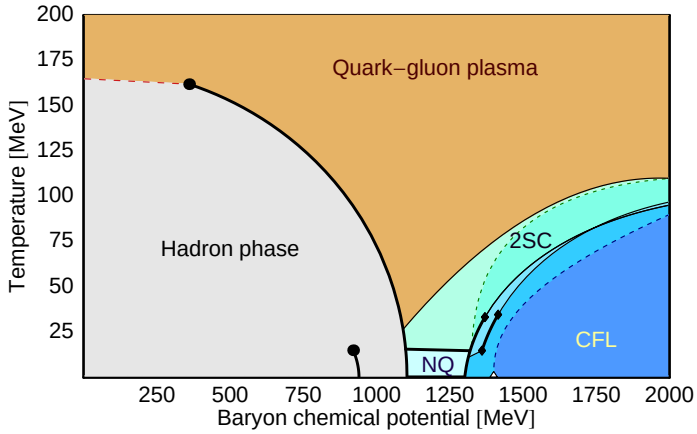

Figure 1: QCD phase diagram where a transition between hadronic matter and QGP occurs at high temperature or large baryon chemical potential [2].

the hadronic matter to large density (large μ_{B}) or heating it to high temperature. This deconfined state of matter is believed to exist in the cosmological era from electro-weak decoupling (10^{-12} s) to hadron formation ($0.5 \cdot 10^{-5}$ s). Further calculations from Lattice-QCD (LQCD) at zero μ_{B} predicts that the transition happens at a critical temperature $T_{\mathrm{c}} \sim 170$ MeV or a critical energy density $\epsilon_{\mathrm{c}} \sim 0.6$ GeV/fm^3 as shown in Fig. 2 [3]. The energy density of QCD matter rises rapidly to a plateau within a narrow temperature interval. The fact that it deviates from the Stefan-Boltzmann limit, labelled ϵ_{SB}, well above the critical temperature implies that the constituents of the QGP interact strongly, as opposed to an ideal gas.

In order to create such matter in a terrestrial laboratory, one collides heavy ions at rela-

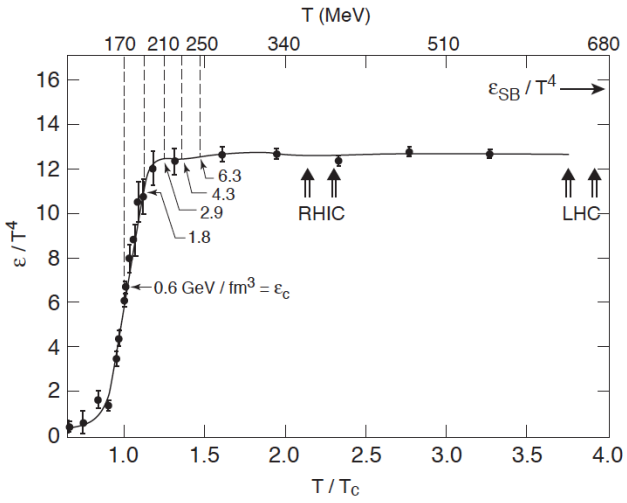

Figure 2: LQCD calculation for the energy density (ϵ) divided by T^4 as a function of temperature (T) scaled by the critical temperature T_c with three light quark flavors. The horizontal arrow on the right-side indicates the value of the Stefan-Boltzmann limit for an ideal quark-gluon gas [3].

tivistic energies as first suggested by T. D. Lee in 1974: "We should investigate phenomena by distributing high energy or high nucleon density over a relatively large volume". The primary goal of heavy-ion physics is to map out the phase transition from hadronic matter to QGP, and study the properties of the QGP. In the last three decades, heavy ions were accelerated and collided at several facilities around the world with gradually increasing energy to generate such deconfined matter for study in the laboratory. The first big facility to provide high-energy heavy-ion collisions is the Alternating Gradient Synchrotron (AGS) at Brookhaven National Laboratory (BNL), where the center-of-mass energy per nucleon pair ($\sqrt{s_{\rm NN}}$) ranges between 2.5 and 4.3 GeV for the Au–Au system. The next increase in energy occurred at the Super Proton Synchrotron (SPS) located at the European Organization for Nuclear Research (CERN), where a top energy of $\sqrt{s_{\rm NN}} = 17.3$ GeV is achieved for Pb–Pb collisions. For the first time, the energy of the colliding system exceeds 10 GeV, which is the minimal colliding energy required to reach critical energy density for the phase transition [4, 5]. Around 2000, the Relativistic Heavy Ion Collider (RHIC) at BNL was commissioned and began to deliver Au–Au collisions up to $\sqrt{s_{\rm NN}} = 200$ GeV, featuring a factor of 10 increase in $\sqrt{s_{\rm NN}}$ compared to SPS. While the vicinity of the phase transition is sampled at SPS, the dynamical evolution at RHIC goes deeply into the deconfined region.

After ten years of great success of the RHIC program that vastly explored the new physics of the QGP, the investigation to the QCD diagram has been further extended by the Large Hadron Collider (LHC) at CERN, where Pb ions have been collided at $\sqrt{s_{\rm NN}} = 2.76$ TeV in 2010, and will reach the design energy of 5.5 TeV in 2015.

The overall dynamic evolution of a relativistic heavy-ion collision can be characterized in several stages. Figure 3 is a schematic light cone diagram that captures the main features of such a high energy collision. The two reactant nuclei approach each other along the $z = t$

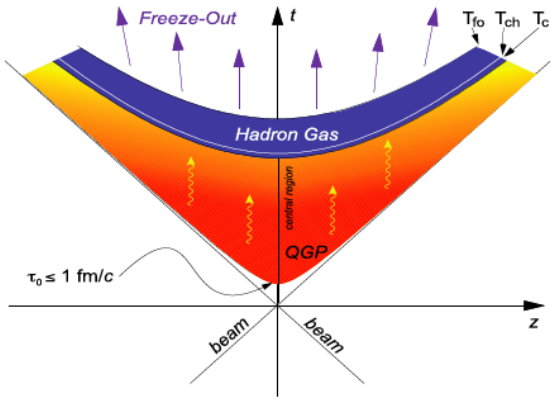

Figure 3: The dynamic evolution of a relativistic heavy-ion collision sketched as a light cone diagram.

trajectories, where t is the proper time and z is the beam direction. For the lead ions colliding with $\sqrt{s_{\rm NN}} = 2.76$ TeV, the Lorentz factor is:

$$\gamma = \frac{E}{m_0 c^2} \sim 2760 \tag{1}$$

Therefore, we can assume that the interaction happens at the point $t = z = 0$ since the nuclei are extremely contracted. Within the course of the initial interpenetration of the two colliding ions, hard scatterings occur, which give rise to outgoing partons (i.e. quarks and gluons) with large transverse momentum ($p_{\rm T}$). These hard-scattered partons acquire virtual mass, populate the transverse phase space, and undergo inelastic QCD shower multiplication. So far, the system is not in thermal equilibrium. As the two nuclei pass by each other, a large energy density at mid-rapidity[1] ($y = 0$) is generated from the inelastic inter-

[1]Rapidity y is defined as $y = \frac{1}{2} \ln \frac{E+p_z}{E-p_z}$, where E is the energy of the particle, and p_z is the momentum

actions of the two parton fields, which are opposing each other in the longitudinal phase space. Due to this mutual stopping of the parton fields, and the concurrent decrease of the parton virtuality, the time scale governing the evolution of the system slows down, which could lead to equilibrium. The time that the QCD system takes to reach this stage is less than 1 fm/c for RHIC energies and above [6]. The system then immediately cools down by expanding both longitudinally and radially. Hadrons and hadronic resonances are formed when the temperature of the system drops down to the parton-hadron transition line ($T_{\rm c}$). At the chemical freeze-out temperature ($T_{\rm ch}$) which is close to $T_{\rm c}$, hadrons decouple from further transmutations and their relative yields stay unchanged. Further expansion dilutes the system to the kinetic freeze-out at $T_{\rm fo}$, where the strong interactions cease altogether, and the spectra of the hadrons are fixed.

In December 2010, the first Pb–Pb collisions at $\sqrt{s_{\rm NN}} = 2.76$ TeV were delivered at the LHC, which marked a new era of heavy-ion physics in an unprecedented energy regime. The QGP produced at RHIC in Au–Au collisions at $\sqrt{s_{\rm NN}} = 200$ GeV was established to be a hot, dense, strongly-coupled colored matter exhibiting nearly-perfect liquid behavior [7]. Studying the properties of the QGP created at the LHC using a different system (Pb–Pb) at different energies would shed light on the field.

Energy density: the primordial energy density (ϵ) of head-on collisions can be related to the transverse energy density ($dE_{\rm T}/dy$) measured at mid-rapidity using the Bjorken model [8]:

$$\epsilon = \frac{1}{\tau_0 \pi R^2} \frac{dE_{\rm T}}{dy} \tag{2}$$

where the initial geometry is considered as a cylinder of length $dz = \tau_0 dy$ and transverse area πR^2. τ_0 denotes the thermalization time, and is conservatively assumed to be 1 fm/c. R is the same as the radius of the Pb nucleus for head-on collisions. The transverse energy density can be deduced from the charged particle pseudo-rapidity[2] (η) density ($dN_{\rm ch}/d\eta$):

$$\frac{dE_{\rm T}}{dy} \sim \frac{3}{2} \langle E_{\rm T} \rangle \frac{dN_{\rm ch}}{d\eta} \tag{3}$$

of the particle along the beam direction.

[2]Pseudo-rapidity η is defined as $\eta = \frac{1}{2} \ln \frac{p+p_z}{p-p_z}$, where p is the momentum of the particle, and p_z is the momentum of the particle along the beam direction. For massless particles, pseudo-rapidity is the same as rapidity.

The factor 3/2 comes from the assumption that charged particles carry about 2/3 of the total energy. The charged particle pseudo-rapidity density in the 0-5% most central[3] Pb–Pb collisions, normalized by the number of nucleon pairs participating in the collision, is shown in Fig. 4 [9, 10]. The resulting density is ~ 1600 as the number of participating pairs is

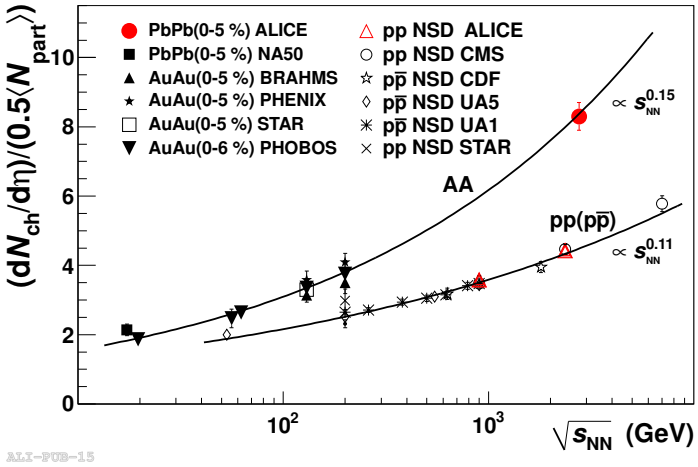

Figure 4: Charged particle pseudo-rapidity density per participant pair for 0-5% most central Pb–Pb collisions (red solid circle).

estimated to be 191 ± 1.9 using a Glauber model [11]. With the mean transverse energy $\langle E_{\mathrm{T}} \rangle$ of the charged particles approximately 1 GeV, the initial energy density is:

$$\epsilon \sim \frac{1}{1 \times \pi \times 7^2} \times \frac{3}{2} \times 1 \times 1600 \sim 16 \text{ GeV/fm}^3 \tag{4}$$

It is well above the critical energy density for the phase transition.

Initial temperature: as a dense hot medium, QGP should emit thermal photons [12] throughout its entire dynamic evolution. These thermal photons are primarily at low p_{T}, and their spectrum is determined by the temperature of the QGP. The spectrum of the direct photons, consisting of photons from both thermal radiation and parton fragmentation, is shown in Fig. 5 for 0-40% central Pb–Pb collisions [13]. An exponential function is fitted to the spectrum below 2 GeV/c, where the thermal photons are expected to dominate. The inverse slope T is the temperature of the radiating system, which turns out to be 304 ± 51

[3]Heavy-ion collisions are usually classified into centrality classes according to their collision geometry. Different centrality classes correspond roughly to different impact parameter ranges. Central collisions refer to collisions with small impact parameters, and peripheral collisions are those with large impact parameters.

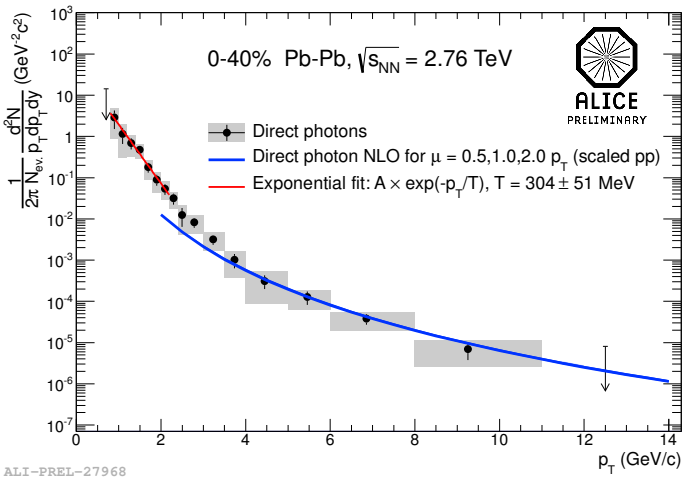

Figure 5: Direct photon spectrum for 0-40% central Pb–Pb collisions, fitted with an exponential function below 2 GeV/c.

.

MeV for the QGP produced at the LHC. Since thermal photons can be emitted by the QGP at any stage of its evolution, the parameter T is to some extent the average temperature of the system, which sets a lower bound for the initial temperature as the system cools down along the evolution. Clearly, the initial temperature is above T_c.

Anisotropic flow: the overlap area of a heavy-ion collision with non-zero impact parameter is not azimuthally symmetric due to the finite size of the colliding nuclei. An example is shown in the left panel of Fig. 6 where the z-axis is along the beam direction

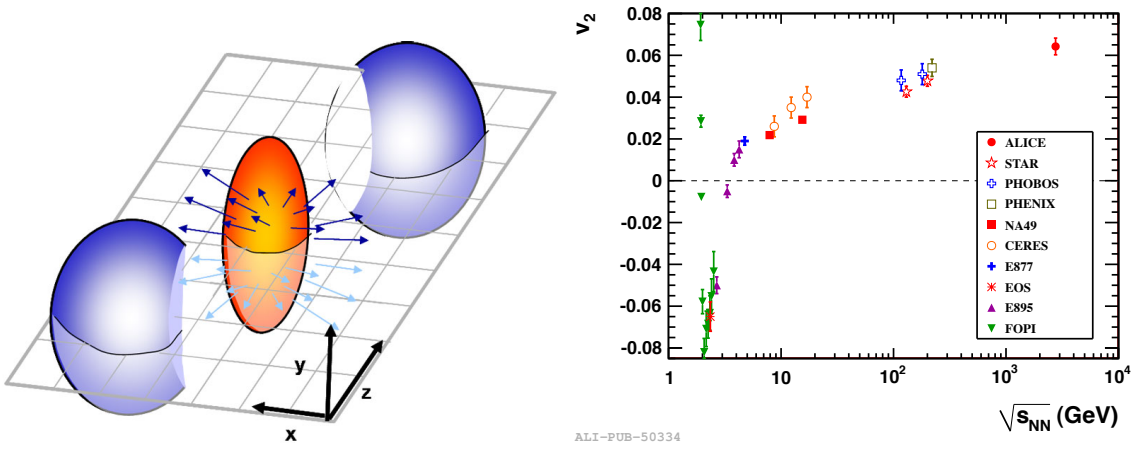

Figure 6: Left: geometry of a heavy-ion collision with non-zero impact parameter. The overlap region has an almond shape. Right: measurement of integrated v_2 for 20-30% semi-central Pb–Pb collisions (red solid circle), compared to similar measurements at lower energies.

and the x-axis is aligned with the impact parameter vector. The plane defined by the x and z axes is usually referred to as the "reaction plane", and the colliding geometry is symmetric with respect to this plane. The almond shape of the overlap area leads to pressure gradients between the center of the overlap zone and its periphery, which vary with azimuth being strongest along the reaction plane (the minor axis of the almond). The resulting collective flow is therefore strongest in the reaction plane, and pushes particles the most. Consequently, the initial anisotropy of the collision geometry in the coordinate space is transferred into the anisotropy in the momentum space of the outgoing particles, whose spectrum can be decomposed via a Fourier expansion [14]:

$$E\frac{d^3N}{d^3p} = \frac{1}{2\pi}\frac{d^2N}{p_{\mathrm{T}}dp_{\mathrm{T}}dy}(1 + \sum_{n=1}^{\infty} 2v_n \cos[n(\varphi - \Psi_R)]) \tag{5}$$

where φ is the azimuthal angle of the outgoing particles, and Ψ_R the azimuthal angle of the reaction plane. Due to the symmetry of the collision geometry, the main contribution comes from v_2 (often referred to as *"elliptic flow"*), and a measurement of the integrated v_2 over p_{T} and rapidity is shown in the right panel of Fig. 6 for 20-30% semi-central Pb–Pb collisions (red solid circle) [15]. The large elliptic flow indicates that the system is equilibrated very early and η/s (shear viscosity η over entropy density s) of the system is very small, such that the pressure gradients originating form the initial geometry could lead to significant collective flow, and the flow pattern survives the later evolution without being dissipated away. For a quantum system, a lower bound on η/s, i.e. $4\pi\eta/s \geq 1$, is calculated using AdS/CFT [16]. Calculations from hydrodynamic models constrain η/s to be $4\pi\eta/s \leq 2$ by comparing to data [17, 18], which confirms the discoveries made at RHIC that the QGP behaves as nearly a "perfect fluid". It is worth mentioning that higher-order harmonic coefficients were also found to be non-zero due to the fluctuations of the initial collision geometry which could lead to higher-order initial pressure gradients [19, 20].

Chemical freeze-out: the relative abundance of hadron species becomes stationary after the hadrons decouple from inelastic transmutations at T_{ch}. It can be successfully described by a statistical hadronization model using grand canonical ensemble [21]. The model assumes that particles are produced in thermal equilibrium governed by a parameter

T, interpreted as the temperature. Fitting this model to data gives $T_{\rm ch} = 152$ MeV with $\mu_{\rm B} = 1$ MeV fixed in the fitting, as shown in Fig. 7 [22].

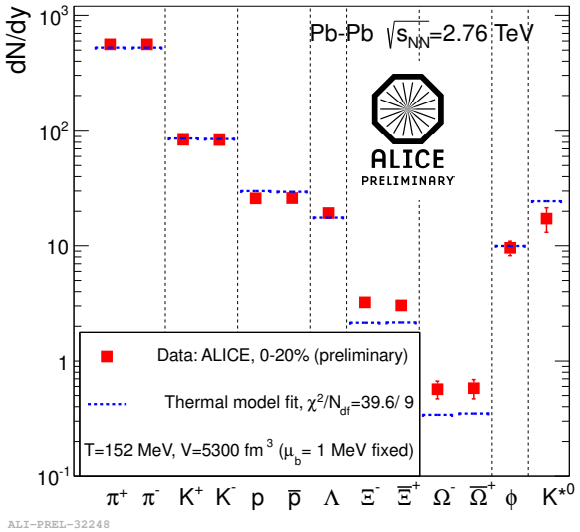

Figure 7: Yields of various hadron species measured in 0-20% most central Pb–Pb collisions. A statistical thermal model fit gives $T_{\rm ch} = 152$ MeV.

Kinetic freeze-out: particle spectra are fixed at kinetic freeze-out, when elastic scatterings end. On the other hand, particles tend to move collectively in both space and momentum due to the hydrodynamic nature of the medium evolution. Hence, the spectra of identified particles at low $p_{\rm T}$ encode information about both the radial flow, quantified by the average transverse velocity $\langle\beta_{\rm T}\rangle$, and the temperature ($T_{\rm fo}$) at the kinetic freeze-out [23, 24]. By fitting the measured spectra with a "blast wave" function [23], the resulting $T_{\rm fo}$ and $\langle\beta_{\rm T}\rangle$ are shown in Fig. 8 for Pb–Pb collisions of different centralities [25, 26]. For the 0-5% most central events, the transverse velocity is about $0.65c$ (c = speed of light) and the kinetic freeze-out temperature is about 95 MeV.

Identical particle correlations: for identical bosons (fermions), quantum statistics results in an enhancement (depletion) for the emitted particles close-by in phase space. This modifies the two-particle correlation functions measured in energy and momentum variables (also called Hanbury-Brown-Twiss or HBT correlations [27]), which are used to extract the freeze-out volume (the size of the system at the time when the strong interactions cease) and the life-time of the system. As shown in Fig. 9 for 0-5% most central Pb–Pb collisions

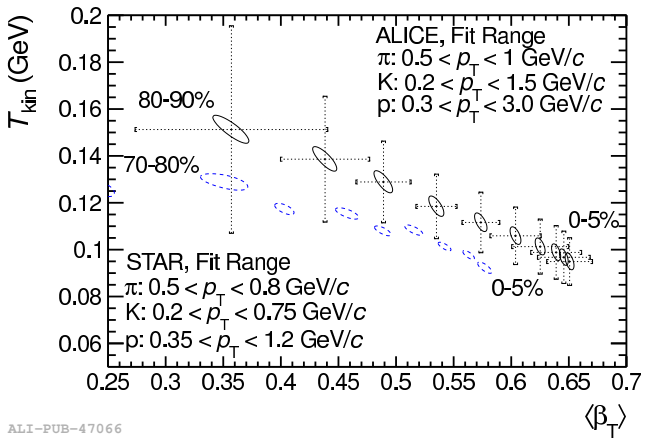

Figure 8: The kinetic freeze-out temperature $T_{\rm fo}$ (T_{kin}) vs average transverse velocity $\langle\beta_{\rm T}\rangle$ in different Pb–Pb centralities (black). The 1-sigma uncertainty ellipses reflect the bin-to-bin systematic uncertainties.

(red solid circle), the freeze-out volume is about 300 fm^3 and the life-time is over 10 fm/c [28].

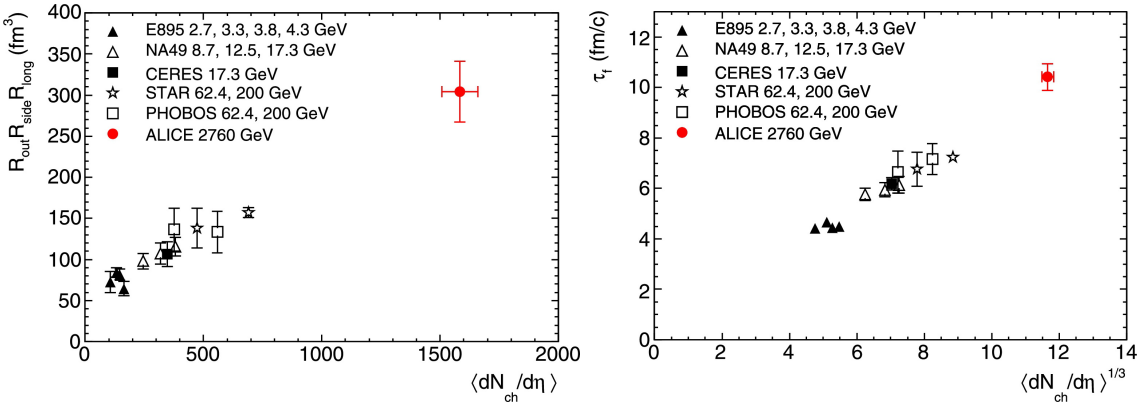

Figure 9: The freeze-out volume (left) and life-time (right) of the 0-5% most central Pb–Pb collisions (red solid circle) [28]. Results from lower energies are also shown for comparison.

We can now compare some global properties of the QGP created at RHIC [29, 30, 31, 32, 28] and the LHC [10, 13, 15, 22, 25, 33], as listed in Table 1. It can be seen that the QGP formed at the LHC is hotter, lives longer and expands to a larger final volume as compared to RHIC.

So far, we have been using the low $p_{\rm T}$ particles ("bulk" production) to deduce the global properties of the QGP. There is another type of probe, namely the high $p_{\rm T}$ partons created in the hard scatterings at the early stage of the collisions. As they travel through the medium,

Table 1: Comparison of the global properties of the QGP created at RHIC and LHC. The percentage in the parentheses corresponds to the centralities used for analysis.

Global properties	RHIC (Au–Au 0.2 TeV)	LHC (Pb–Pb 2.76 TeV)
Primordial energy density	5.4 GeV/fm^3 (0-5%)	16 GeV/fm^3 (0-5%)
Initial temperature	$>$ 221 MeV (0-20%)	$>$ 304 MeV (0-40%)
Elliptic flow	0.045 (20-30%)	0.065 (20-30%)
T_{ch}	157 MeV (0-5%)	152 MeV (0-20%)
T_{fo}	89 MeV (0-5%)	95 MeV (0-5%)
$\langle\beta_{\mathrm{T}}\rangle$	0.59 (0-5%)	0.65 (0-5%)
System size	150 fm^3 (0-5%)	300 fm^3 (0-5%)
Life time	7 fm/c (0-5%)	11 fm/c (0-5%)

they interact with the medium and serve as diagnostic tracers. Since the partons are not directly measurable, jets, which are defined as the sprays of hadrons originating from the parton fragmentation, are often used as a proxy. Some theoretical considerations for hard probes are discussed in Chapter 2, followed by the introduction of jet-finding algorithms in Chapter 3. A Large Ion Collider Experiment (ALICE) [34] used to measure the hadrons comprising jets is introduced in Chapter 4. Chapters 5 to 11 are dedicated to the first inclusive jet cross section measurement at $\sqrt{s} = 2.76$ TeV in pp collisions [35]. Hadron-jet coincidence measurements are developed to study the influence of the medium on jets in Pb–Pb collisions, as detailed in Chapter 12 [36]. A summary is given in Chapter 13.

2 QCD and hard probes

2.1 QCD

In the Standard Model, QCD is a gauge theory based on "color" charges (SU(3)) describing the strong interactions that bind the nucleons (i.e. protons and neutrons) in the nuclei and also the quarks in the nucleons. There are six "flavors" of quarks, each has three colors, divided into three families based on their mass and charge. Gluons are vector gauge bosons that mediate strong interactions between colored objects, analogous to the exchange of photons in the electromagnetic force between charged particles in Quantum ElectroDynamics (QED). There are eight gluons, one for each color state. Unlike photons in QED, gluons themselves carry color charges, therefore they also participate in strong interactions besides being a mediator. The strength of strong interactions is defined by the QCD coupling constant α_s, whose value depends on the relevant scale of the processes.

The lowest order Feynman diagram of an annihilation process for a quark anti-quark pair ($q + \bar{q} \rightarrow q + \bar{q}$) is shown in the left panel of Fig. 10. Each vertex contributes a factor $\sqrt{\alpha_s}$ to the matrix element for the cross section of the process. A brief fluctuation

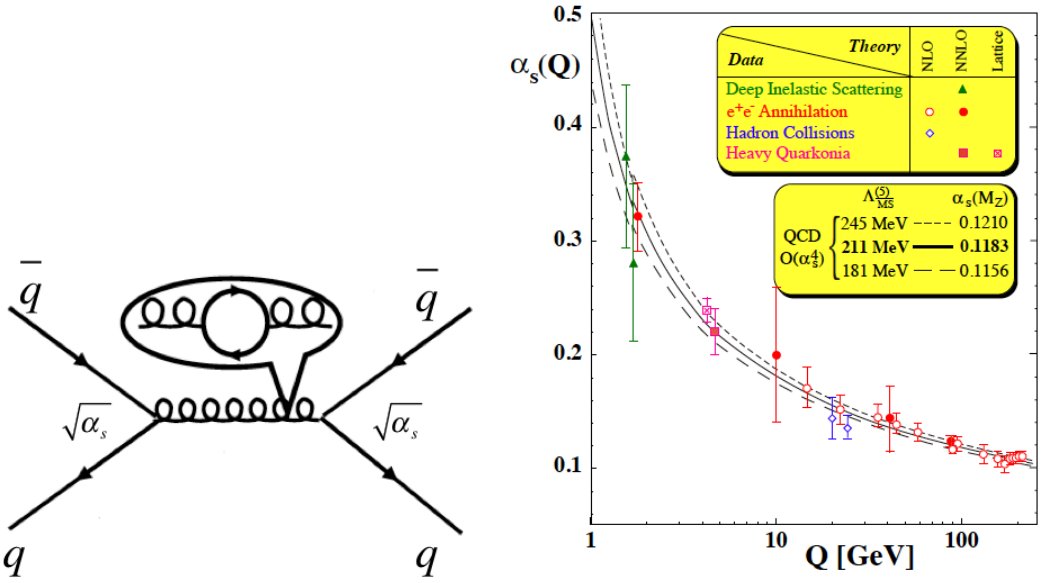

Figure 10: Left: lowest order Feynman diagram for the quark anti-quark annihilation process. Each vertex contributes a factor $\sqrt{\alpha_s}$ to the matrix element. Right: dependence of the strong coupling constant on the energy scale Q of the process of interest [37].

of the gluon to a fermion anti-fermion pair can be resolved if one is able to probe the process at small distance scales, as shown in the diagram inset in Fig. 10 (left). As a matter of fact, more fermion anti-fermion pairs emerge as the distance scale gets even smaller. Contributions of these higher-order processes are divergent, which is overcome by introducing a renormalization scale μ into the calculation. However, any physical observable ("σ") should be independent of the arbitrarily chosen renormalization scale, leading to the renormalization group equation:

$$\mu^2 \frac{d}{d\mu^2}\sigma(\frac{Q^2}{\mu^2}, \alpha_{\rm s}) = (\mu^2 \frac{\partial}{\partial \mu^2} + \mu^2 \frac{\partial \alpha_{\rm s}}{\partial \mu^2}\frac{\partial}{\partial \alpha_{\rm s}})\sigma = 0 \tag{6}$$

By including only the 1-loop contribution, the dependence of $\alpha_{\rm s}$ on the renormalization scale becomes:

$$\alpha_{\rm s}(Q^2) = \frac{\alpha_{\rm s}(\mu^2)}{1 + \frac{\alpha_{\rm s}(\mu^2)}{12\pi}(11N_c - 2n_f)\log(Q^2/\mu^2)} \tag{7}$$

where N_c is the number of colors, and n_f the number of relevant quark flavors. Introducing an overall scale of $\Lambda_{\rm QCD} \sim 0.2$ GeV:

$$\alpha_{\rm s}(Q^2) = \frac{12\pi}{(11N_c - 2n_f)\log(Q^2/\Lambda^2_{\rm QCD})},\ \Lambda^2_{\rm QCD} = \mu^2 e^{-12\pi/[(11N_c - 2n_f)\alpha_{\rm s}(\mu^2)]} \tag{8}$$

The dependence of $\alpha_{\rm s}(Q^2)$ on the relevant scale Q^2 of the process under study is shown in the right panel of Fig. 10, confronted with the data, where a good agreement is seen [37]. At long distances (small Q^2), $\alpha_{\rm s}$ grows almost linearly as the distance gets larger, which makes it energetically impossible to separate two color charges. This phenomenon, called "confinement", is responsible for the fact that only color neutral hadrons are measurable. No isolated colored charge can exist as a free particle. On the other hand, as the distance gets very small (large Q^2), the magnitude of $\alpha_{\rm s}$ decreases to about 0.1, entering the regime of "asymptotic freedom", where QCD becomes perturbative, thus calculable. Theoretical predictions made at this energy scale can be expressed as an expansion in powers of the coupling constant, and the major contributions come from the first few terms.

2.2 Hard probes

Hard partons (large p_{T}), produced in partonic scattering with large momentum transfer, constitute valuable tools to study QGP since they are produced in the very early stage of the collisions: $\tau \sim 1/p_{\mathrm{T}} \sim 0.1$ fm/c, allowing them to propagate through the medium. The potential modification to the parton energy and fragmentation pattern by the medium can be utilized to deduce the medium properties. The fragmentation process of the energetic partons can be described in a simple view: as the outgoing partons move away from each other in the center-of-mass frame, it soon becomes energetically favorable to produce additional quark anti-quark pairs distributed between the two leading charges. The virtuality of the parent parton decreases as the pair production repeats itself, leading to a collimated spray of final-state color-neutral hadrons, which is defined as a "jet".

Theoretically, these hard probes are well calibrated in the sense that their cross section can be calculated within the perturbative QCD (pQCD) framework as α_{s} is small for high-energy parton interactions. Using the QCD "factorization theorem" [38], the inclusive production cross section of a high p_{T} hadron ("h") or a jet originating from a hard parton takes the form:

$$d\sigma_{\mathrm{AA}\to\mathrm{h/jet}} \sim f_{\mathrm{a/A}}(x_1, Q^2) \otimes f_{\mathrm{b/A}}(x_2, Q^2) \otimes d\sigma_{\mathrm{ab}\to\mathrm{c+X}}(x_1, x_2) \otimes D_{\mathrm{c}\to\mathrm{h/jet}}(z, \mu_f^2) \qquad (9)$$

where $\sigma_{\mathrm{ab}\to\mathrm{c+X}}(x_1, x_2)$ is the perturbative cross section for the production of a parton c from the partonic scattering between partons a and b, calculable up to a given order in α_{s}. The two non-perturbative, universal (i.e. process independent) terms are:

- $f_{\mathrm{a/A}}(x, Q^2)$: the parton distribution function (PDF) [39], denoting the probability to find a parton of flavor a with momentum fraction $x = p_{\mathrm{a}}/p_{\mathrm{A}}$ inside a nucleus A.
- $D_{\mathrm{c}\to\mathrm{h/jet}}(z, \mu_f^2)$: the fragmentation function (FF), encoding the probability that a parton c fragments into a final-state hadron or jet with momentum fraction $z = p_{\mathrm{h/jet}}/p_{\mathrm{c}}$. In terms of a theoretical jet that contains all the fragments of the parent parton, FF collapses to a δ-function: $D_{\mathrm{c}\to\mathrm{h/jet}}(z, \mu_f^2) = \delta(1 - z)$.

The PDF and FF can be determined experimentally e.g. in deep inelastic $e^{\pm}$-nucleus scat-

tering and e^+e^- collisions, respectively, at some particular scales, and evolved to other scales via DGLAP equations [40, 41, 42]. The basic assumption underlying the factorized form of Eq. 9 is that the characteristic time for the parton-parton hard scattering is much shorter than any long-distance interactions before (parton interactions within a nucleus) and after (parton fragmentation into hadrons) the hard collisions. Therefore, the short- and long-distance effects do not interfere and can be evaluated separately. Since the partons are effectively "frozen" during hard scattering, they can be treated as free inside the nucleus, leading to the assumption that the parton density in a nucleus with mass number A can be viewed as an incoherent superposition of A independent nucleons:[4] $f_{\mathrm{a/A}}(x, Q^2) \sim A \cdot f_{\mathrm{a/p}}(x, Q^2)$. Thus:

$$d\sigma_{\mathrm{AA}\to\mathrm{h/jet}} \sim A \cdot A \cdot f_{\mathrm{a/p}}(x_1, Q^2) \otimes f_{\mathrm{b/p}}(x_2, Q^2) \otimes d\sigma_{\mathrm{ab}\to\mathrm{c+X}}(x_1, x_2) \otimes D_{\mathrm{c}\to\mathrm{h/jet}}(z, \mu_f^2) \quad (10)$$

which means the cross section of hard probes in a A–A collision scales simply as $A \cdot A$ times the corresponding cross section in pp collisions:

$$d\sigma_{\mathrm{AA}\to\mathrm{h/jet}} = A \cdot A \cdot d\sigma_{\mathrm{pp}\to\mathrm{h/jet}} \quad (11)$$

In heavy-ion experiments, usually the yield is measured for a given centrality (or impact parameter b). Hence the scaling can be rewritten as:

$$dN_{\mathrm{AA}\to\mathrm{h/jet}}(b) = \langle T_{\mathrm{AA}}(b) \rangle \cdot d\sigma_{\mathrm{pp}\to\mathrm{h/jet}} \quad (12)$$

where the nuclear overlap function is determined via $T_{\mathrm{AA}}(b) = N_{coll}(b)/\sigma_{NN}^{inel}$. $N_{coll}(b)$ is the number of binary nucleon-nucleon collisions that occur in a nucleus-nucleus collision at an impact parameter b. It can be calculated from the Glauber model. σ_{NN}^{inel} is the nucleon-nucleon inelastic cross section. The *nuclear modification factor*, used to quantify the effects

[4] In reality, initial state "(anti-)shadowing" effects modify the nuclear PDFs compared to the proton PDFs [43].

of the medium on the yield of the hard probes, is built as:

$$R_{\mathrm{AA}}(p_{\mathrm{T}}, \eta; b) = \frac{d^2 N_{\mathrm{AA}}/dp_{\mathrm{T}}d\eta}{\langle T_{\mathrm{AA}}(b)\rangle \cdot d^2\sigma_{\mathrm{pp}}/dp_{\mathrm{T}}d\eta} \tag{13}$$

By definition, R_{AA} is equal to unity if there are no medium effects. Such a measurement has been carried out for charged hadrons by the ALICE collaboration, and the resulting R_{AA} is shown in Fig. 11. A strong suppression of R_{AA} is present over the entire kinematic

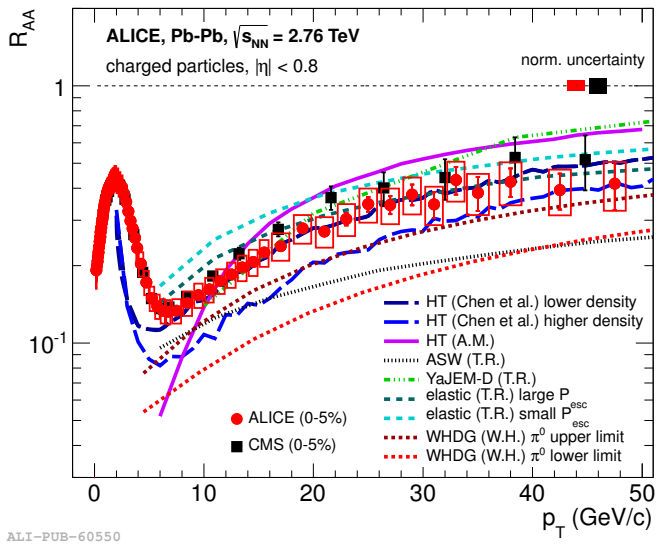

Figure 11: R_{AA} of charged hadrons measured by ALICE at mid-rapidity in the 0-5% most central Pb–Pb collisions (red solid circles). The boxes around the data points denote the systematic uncertainties. Measurements from CMS and predictions from various models are shown for comparison.

range, reaching a minimum of about 0.13 around $6-7$ GeV/c. Such a large suppression indicates that the kinematics and/or the fragmentation pattern of the probing partons are modified dramatically by the strongly coupled medium. Any model correctly describing the energy loss mechanism must be able to reproduce such measurement.

2.3 Parton energy loss in the QGP

"Jet quenching" refers to the attenuation or disappearance of the spray of hadrons resulting from the fragmentation of the hard partons that have suffered significant energy loss in the QGP. This phenomenon is supported by the R_{AA} measurement presented in Fig. 11. The

two main mechanisms for energy loss are collisional and radiative, as shown in Fig. 12. The

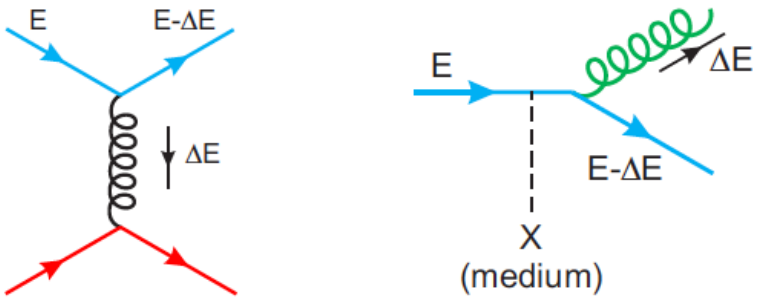

Figure 12: Schematic diagram for the collisional (left) and radiative (right) energy loss for a high p_{T} parton propagating through the QGP.

"scattering power" of the medium is quantified by the transport coefficient ($\hat{q}$), which is defined as the average transverse momentum squared transferred to the traversing partons per unit path-length:

$$\hat{q} = \frac{\langle q_{\perp}^2 \rangle_{\mathrm{med}}}{\lambda} \tag{14}$$

where λ is the mean free path. It is defined as $\lambda = 1/(\rho\sigma)$, where ρ is the medium density, and σ the cross section of parton-medium interaction. $\langle q_{\perp}^2 \rangle_{\mathrm{med}}$ is proportional to the medium temperature and $\sqrt{\alpha_{\mathrm{s}}}$. Apparently, $\hat{q}$ encodes the detailed intrinsic properties of the medium.

Collisional energy loss refers to the energy loss that occurs in the elastic scattering between the traversing parton and the medium constituents. For light quarks and gluons, the average collisional energy loss takes the form [44]:

$$\langle \Delta E_{coll} \rangle \sim \alpha_{\mathrm{s}} C_R \hat{q} L \ln E \tag{15}$$

where L is the length of the medium, $C_R = 4/3(3)$ the quark (gluon) color charge, and E the energy of the probe parton.

Radiative energy loss refers to the energy loss via induced gluon radiation by the traversing partons through inelastic scatterings with the medium. In the BDMPS model which computes the energy loss under a multiple soft-scatterings approximation, the radia-

tive energy loss scales with square of the medium length [45]:

$$\langle \Delta E_{rad} \rangle \sim \alpha_{\rm s} C_R \hat{q} L^2 \tag{16}$$

For partons above 5 GeV/c or so, the dominant energy loss is through the medium induced gluon radiation [46]. The characteristic L^2 dependence comes from the non-Abelian nature of QCD: the radiated gluon is itself color-charged, and its emission probability is enhanced by its subsequent interactions with the medium. Furthermore, the magnitude of the energy loss is dependent on the color charge, which is different for quarks and gluons.

In order to compare models with data, the effects of energy loss is usually convoluted into the medium-modified FF: $D_{\rm c\to h/jet}(z,\mu_f^2)^{\rm vac} \to D_{\rm c\to h/jet}(z',\mu_f^2)^{\rm med}$. The final hadronization of the parton is assumed to occur in the vacuum with degraded energy after the parton has escaped from the medium. In the ASW approach [47], the modification to the FF is encoded in the quenching weights $P(\epsilon,\hat{q})$, which represent the probability that the hard parton loses a fraction of its energy $\epsilon = \Delta E/E$ via multiple gluon emissions:

$$D_{\rm c\to h/jet}(z',\mu_f^2)^{\rm med} \sim P(\epsilon,\hat{q}) \otimes D_{\rm c\to h/jet}(z,\mu_f^2)^{\rm vac} \tag{17}$$

The medium expands concurrently as the hard partons travel through it, causing the density (ρ), thus $\hat{q}$, to decrease. Therefore, $\hat{q}$ evolves with time, and the traversing parton loses most energy in the early stage when $\hat{q}$ is the largest. This evolution is taken into account by replacing the static $\hat{q}$ with an effective, expansion time averaged $\hat{q}_{\rm eff}$ in the realistic case of an expanding fireball:

$$\hat{q}_{\rm eff} = \frac{2}{L^2}\int_{t_0}^{L} dt(t-t_0)\hat{q}(t) \tag{18}$$

To make better connection with experimental results, models should also take into account the position dependence of the medium length experienced by the partons produced at different locations within the fireball. A comparison of the ASW calculation with data is shown in Fig. 11, which helps to constrain the extracted value for $\hat{q}_{\rm eff}$ and understand the medium properties.

The measurement of medium properties using high p_{T} hadrons, which are usually the leading particles (highest p_{T}) of the parton fragmentation, is easy to be carried out experimentally, and has provided valuable constraints to model calculations. However, they only constrain the kinematics of the parent parton as a lower bound, and thus contain limited information about the parton-medium interactions. This motivates us to turn to full jet reconstruction which is designed to group as many fragments as possible from the parent parton to better reconstruct the parton kinematics, even though it is experimentally very challenging especially in heavy-ion collisions. It also provides an opportunity to directly measure the modification of the parton FF in the medium to help reveal the whole picture of jet quenching.

3 Jet finding algorithm

Experimentally there is no unambiguous way to distinguish on a particle-by-particle basis whether a particle comes from a hard jet or soft background. Therefore, jet algorithms, with a set of rules for grouping particles, are used to provide a collection of experimental jets for analyses. They usually involve a distance measure determining whether two particles belong to the same jet, and a recombination scheme, which indicates how to assign momentum to the final jets. The most important theoretical requirement for any reliable jet algorithm is InfraRed and Collinear (IRC) safety, namely the set of hard jets obtained by the algorithm should be insensitive to any soft emission or collinear splitting in the event [48]. Dating back to the first jet algorithm invented by Sterman and Weinberg in the 1970's [49], tens of different algorithms have been proposed in the subsequent years. They can be classified into two categories: cone algorithms and sequential recombination algorithms.

3.1 Cone algorithms

The most widely used cone algorithms are "iterative cones" (IC), in which the distance measure between particles i and j is:

$$\Delta R_{ij}^2 = (y_i - y_j)^2 + (\varphi_i - \varphi_j)^2 \tag{19}$$

where $(y_i,\ \varphi_i)$ and $(y_j,\ \varphi_j)$ are the coordinates of the particles i and j in rapidity[5] and azimuthal angle. Such an algorithm starts with a seed particle i, which sets the initial direction of the cone, and sums the momenta of all the particles j if their distance measures are smaller than a pre-defined resolution parameter R (a.k.a. jet radius). The direction of the cone is recalculated using all the particles in the cone, which then serves as a new seed. The procedure is iterated until the direction of the resulting cone is stable. This is done for all the seeds and the resulting stable cones are candidates for jets. No explicit energy scale is involved in this recipe, but usually only jets above a certain threshold are used for analyses. To be fully specified, two issues have to be settled: 1) what should be taken as

[5]In practice, pseudo-rapidity η is used more frequently since the particle identification is usually not available.

seeds? 2) what should be done to the particles that contribute to more than one stable cone (i.e. "cone overlapping")?

Progressive Removal (IC-PR): In this approach, the highest momentum (hardest) particle in the event is taken as the first seed. Once a stable cone is found around it, it is called a jet and all the particles inside of the cone is removed from the event. Then the hardest particle left in the event is used as the new seed, and a new stable cone is formed around it. The procedure is iterated until all the particles above an optional threshold are progressively removed [50]. By design, overlapping cones are avoided. However, this type of algorithm suffers from collinear unsafety, as illustrated in Fig. 13 [48]. If a collinear safe jet algorithm finds one jet in configuration (a), where a virtual loop is also drawn, it should also find one jet in configuration (b) with one collinear splitting. In a pQCD calculation, integrating over loop variables in (a) and the splitting angle in (b) leads to canceling divergences such that the 1-jet cross section remains finite. The particle composition in

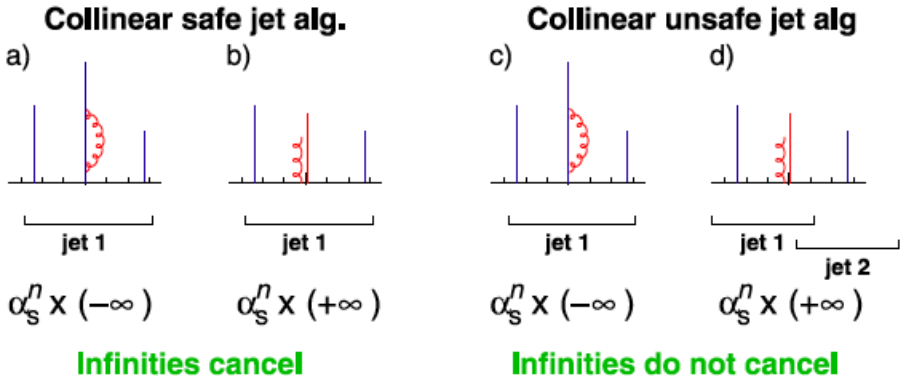

Figure 13: Illustration of collinear safe (left) and unsafe (right) jet algorithms, together with implications for pQCD calculations. Partons are the vertical lines with their heights proportional to their transverse momenta.

diagrams (c) and (d) are the same, but the IC-PR algorithm is used. In (c), the hardest particle is the middle one, which is taken as the seed. A stable cone containing all the particles is obtained by iterating, which renders a single jet. In configuration (d), due to the particle splitting, the leftmost particle becomes the hardest and provides the first seed. Iteration from this seed leads to a jet ("jet 1") that does not contain the rightmost particle. Therefore, the rightmost particle remains and forms a second jet ("jet 2") on its own [51].

As a consequence, the divergences of (c) and (d) now contribute to 1-jet and 2-jet cross sections separately, and lead to divergence in the pQCD calculation. *In general, all the seeded algorithms suffer from collinear unsafety.*

Split-Merge (IC-SM): In this second approach, if all the particles above an optional threshold in the events are chosen as seeds and all the stable cones are obtained by iterating from the seeds, it could happen that some cones overlap. This can be solved using a split-merge procedure, whose working principles are essentially the following [52]:

1. Start from the list of "protojets", which is just the list of all stable cones.
2. Take the protojet with the highest p_{T}, and label it a.
3. Find the next hardest protojet that overlaps with a, and label it b. If b does not exist, remove a from the list of the protojets, add it to the list of the final jets and restart from step 2.
4. Calculate the p_{T} sum of all the particles shared between a and b. If $p_{\mathrm{T}}^{share}/p_{\mathrm{T}}^{b} > f$, where f is the overlap threshold, replace protojets a and b with a single merged protojet. Otherwise, split the protojets by assigning the shared particles to the closest protojet.
5. Repeat from Step 2 until there are no protojets left.

The final set of jets depends on the initial set of stable cones. If the addition of a new soft seed particle leads to a new stable cone, it could change the final jet list, which makes the IC-SM type of algorithms infrared unsafe [52, 48]. This is illustrated in Fig. 14. In an

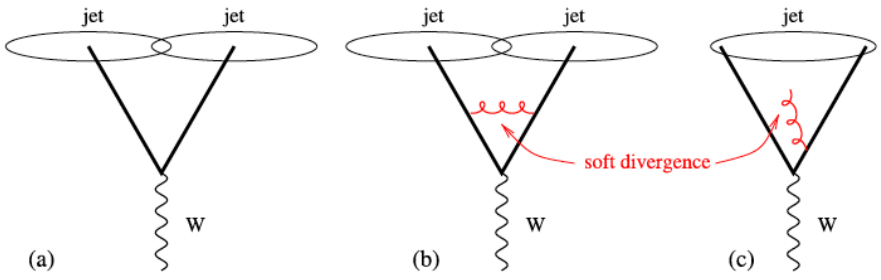

Figure 14: Illustration of the infrared unsafety for IC-SM type of algorithms. The addition of the soft emission merges two jets into one, which makes the pQCD calculation divergent.

event (a), the two hard partons act as seeds, and two jets are found. The same occurs in diagram (b) which contributes negative infinity to the 2-jet cross section due to the loop. However, in (c) the appearance of the additional soft particle provides a new seed, causing a new stable cone to be found containing the two hard partons as long as they have similar momenta and are separated by less than $2R$. This new stable cone overlaps with the two original cones, and only one jet is found after the split-merge procedure. Consequently, there will be non-canceling infinite contributions to 1-jet and 2-jet cross sections in pQCD calculations [53].

SISCone: one full solution to infrared unsafety is a Seedless Infrared-Safe Cone jet algorithm (SISCone [54]), which avoids the usage of seeds and iterations. It first finds all the stable cones of radius R, which is defined as a circle in the (y,φ) plane whose summed momenta of all the particles inside of the cone is the same as the center of the cone. Then the split-merge procedure [52] is utilized to deal with the overlapping cones. Since no seeds are used, this algorithm is collinear safe.

3.2 Sequential recombination algorithms

Sequential recombination algorithms are IRC safe, and run much faster than the cone algorithms [48]. The distance measure used in sequential recombination algorithms is:

$$d_{ij} = \min(p_{T,i}^{2k}, p_{T,j}^{2k}) \frac{\Delta R_{ij}^2}{R^2}, \ \Delta R_{ij}^2 = (y_i - y_j)^2 + (\varphi_i - \varphi_j)^2 \tag{20a}$$

$$d_{iB} = p_{T,i}^{2k} \tag{20b}$$

where k is a parameter that is 1 for the $\mathrm{k_T}$ algorithm [55], 0 for the Cambridge/Aachen algorithm [56, 57], and -1 for the anti-k_T algorithm [51]. The jet finding procedure follows:

1. Start with a list of pre-clusters, i.e. 4-vectors of particles
2. Calculate d_{iB} for each pre-cluster and d_{ij} for each pair (i, j) of pre-clusters
3. Find the minimum of all the d_{iB} and d_{ij} and label it $d_{\min}$. If $d_{\min}$ is a d_{ij}, remove pre-clusters i and j from the list and replace them with a new merged pre-cluster. If $d_{\min}$ is a d_{iB}, the pre-cluster i cannot be merged and is added to the list of jets.

4. Repeat the procedure until the list of pre-clusters is empty

The anti-k_{T} algorithm is predominantly used by all the LHC experiments for jet measurements, including this thesis [35, 58, 59, 60].

3.3 Recombination scheme

The recombination scheme is an integral part of any jet algorithm, which dictates how the particles are combined to give the kinematics of the resulting jets. The most used scheme nowadays is the E-scheme [61], which simply adds the four-vectors of the particles together. Another useful recombination scheme provided by the FastJet package [61, 62] is the boost invariant p_{T} scheme (BIpt-scheme), which defines the combination of the particles as:

$$p_{\mathrm{T}}^{r} = \sum_{i} p_{\mathrm{T}}^{i} \tag{21a}$$

$$y^{r} = \sum_{i} \frac{p_{\mathrm{T}}^{i}}{p_{\mathrm{T}}^{r}} y^{i} \tag{21b}$$

$$\varphi^{r} = \sum_{i} \frac{p_{\mathrm{T}}^{i}}{p_{\mathrm{T}}^{r}} \varphi^{i} \tag{21c}$$

where p_{T}^{r}, y^{r} and φ^{r} are the transverse momentum, rapidity and azimuthal angle of the resulting jets.

4 Experimental setup

4.1 LHC

The LHC is located at CERN on the French-Swiss border near Geneva, Switzerland. Being the largest synchrotron accelerator in the world, the LHC recycles the old Large Electron-Positron Collider (LEP) tunnel, which is 27 km in circumference and on average 100 meters underground. The LHC employs a collider model, instead of a fixed-target setup, to maximize the energy carried by the colliding objects to produce new particles. The two counter-rotating beams travel in individual rings, and collide at four interaction points where the four major experiments are located.

The layout of the LHC is illustrated in Fig. 15, where the four main experiments are shown. They are the Compact Muon Solenoid (CMS) [63], A Toroidal LHC Apparatus (ATLAS) [64], ALICE [34] and Large Hadron Collider beauty (LHCb) [65]. CMS and ATLAS are large general-purpose particle physics detectors, which are aimed to discover new particles, e.g. the Higgs Boson, super-symmetry particles, etc. LHCb is a specialized experiment designed to study CP violation involving bottom quarks, which will provide insights into the matter-antimatter asymmetry in the universe today. ALICE is specially built to explore the new deconfined matter created in heavy-ion collisions.

In order to produce high-energy, high-intensity proton and Pb ion beams, the LHC uses 1232 magnetic dipoles, 858 quadrupoles, and 8 Radio Frequency (RF) cavities per ring to bend, focus and accelerate beams [67, 68].

4.1.1 Magnetic dipole

Since the LHC beam pipe inside the tunnel follows a closed circle, a magnetic field is needed to bend the particles such that their trajectory is a closed loop with a fixed radius defined by the tunnel. This bending magnetic field is provided by the superconducting dipoles.

It is customary to discuss the motion of the particles in a synchrotron using the coordinate system displayed in Fig. 16, where x and y are the horizontal (h) and vertical (v) axes in the transverse plane, and s or θ is the longitudinal axis. Assuming that the constant magnetic field ($\vec{B}$) provided by a dipole is along the vertical axis and that a particle moves

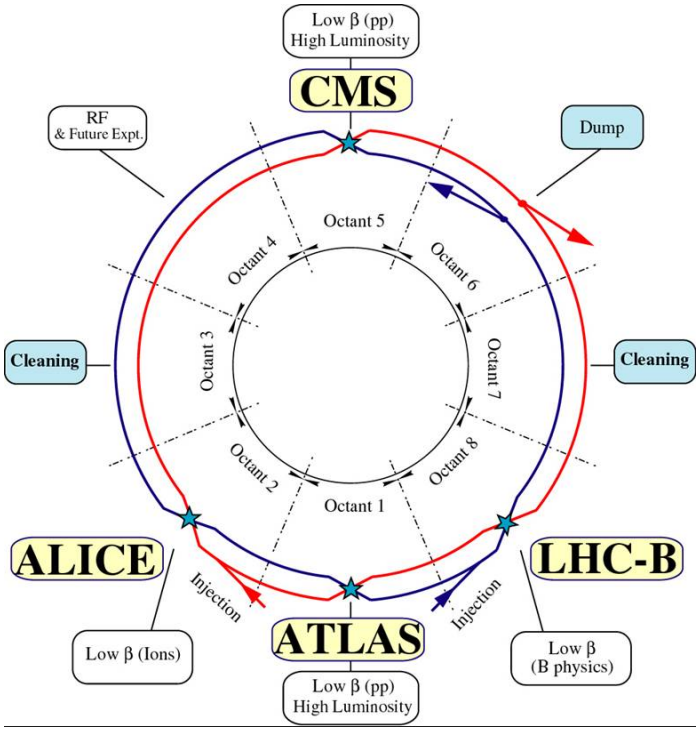

Figure 15: The layout of the LHC [66].

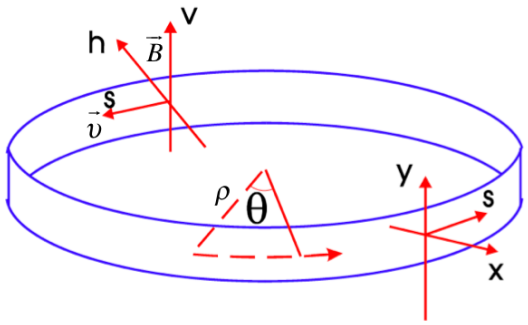

Figure 16: Coordinate system for particles traveling in a synchrotron.

along the longitudinal axis with velocity $\vec{v}$, the Lorentz force exerted on this particle is:

$$\vec{F} = q\vec{v} \times \vec{B} = qvB \tag{22}$$

where q is the charge of the particle.

On the other hand, for such a particle traveling along a circular orbit with a fixed radius ρ, the centripetal force needed is:

$$\vec{F}_{\mathrm{c}} = \frac{mv^2}{\rho} \tag{23}$$

where m is the mass of the particle. If the centripetal force comes solely from the dipoles, the magnetic field should meet the requirement:

$$B\rho = \frac{mv}{q} = \frac{p}{q} \tag{24}$$

"$B\rho$" is called "Magnetic Rigidity", which is related to the momentum (p) of the particles. If we want to increase the particle momentum while still keeping them in the beam pipe, the magnetic field should be increased accordingly. At the LHC, a magnetic field of 8.33 T is needed to bend the proton beam at 7 TeV [67]. A series of dipole magnets are used to bend the beam around a closed path.

4.1.2 Magnetic quadrupole

Dipole magnets keep the motion of the particles stable along the longitudinal axis. However, if the particles have transverse velocities, dipoles alone will not be able to prevent them from being lost. Therefore, extra focusing in the transverse plane is needed to pull the particles back to the ideal trajectory when they drift away. This can be achieved by using quadrupole magnets.

A quadrupole magnet has four poles, two North and two South. The magnetic field inside a quadrupole magnet is shown in the left panel of Fig. 17, and its strength is given by:

$$B_{\mathrm{x}} = Ky, \; B_{\mathrm{y}} = Kx \tag{25}$$

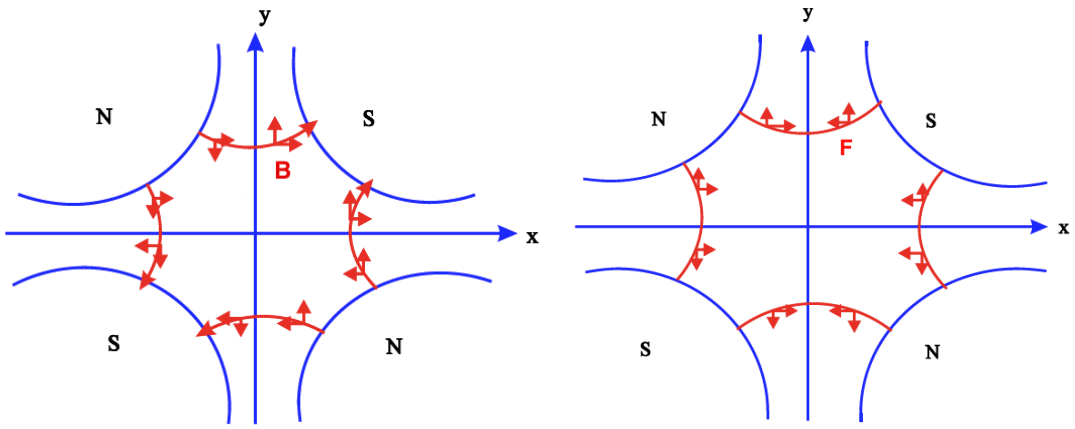

Figure 17: The magnetic fields (left) and forces (right) generated by a quadrupole magnet.

Assuming a particle moves along the longitudinal axis (perpendicular to the xy plane), the forces that act on the particle by the magnetic field are shown in the right panel of Fig. 17. If the particle moves away from the center along the x-axis, it will be deflected back by the restoring forces. So the quadrupole focuses the beam horizontally. Unfortunately, the opposite is true along the y-axis, i.e. the quadrupole defocuses the beam vertically. Such a quadrupole is called a "Focusing Quadrupole (QF)". If we rotate a QF by 90°, it will become a "Defocusing Quadrupole (QD)", which provides a focusing force in the vertical direction, but a defocusing force in the horizontal direction. In order to focus the beam in both horizontal and vertical directions, a combination of QF and QD, a FODO cell as shown in Fig. 18, is commonly used.

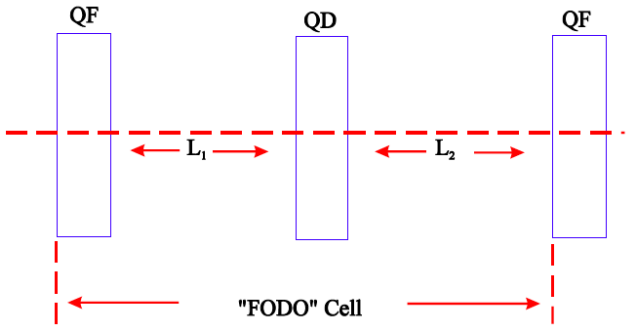

Figure 18: Layout of a FODO cell consisting of a focusing quadrupole, a defocusing quadrupole and drift sections.

The restoring force that a particle experiences in a quadrupole is proportional to its

deviation from the central trajectory, which is very similar to a simple harmonic motion. Therefore, the particle actually oscillates around the central path in the transverse plane as it moves along ("Betatron Oscillation" [69]). Two variables are used to characterize this oscillation: position or the displacement (x) of the particle from the central path, and the angle (θ) with respect to the central path, as shown in Fig. 19:

$$x' = \frac{dx}{ds} = tan(\theta) \approx \theta \tag{26}$$

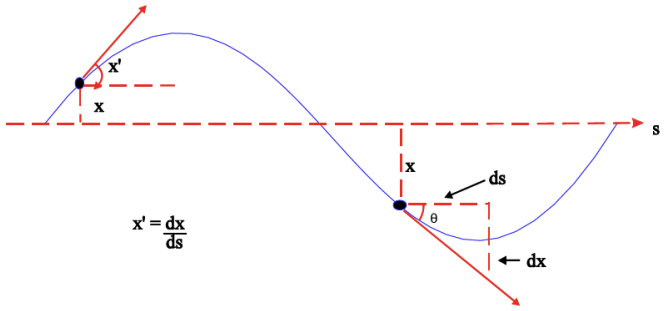

Figure 19: Displacement and angle with respect to the central path in the transverse plane as a particle moves around the accelerator.

A general equation to describe the motion of such a particle is Hill's equation:

$$\frac{d^2x}{d^2s} + k(s)x = 0 \tag{27}$$

where $k(s) = K(s)/B\rho$ is purely determined by the layout of the magnets. The restoring force varies along the accelerator, e.g. it is zero outside of the quadrupole magnets, therefore K can be viewed as a function of s. The solution to Hill's equation has the form:

$$x = \sqrt{\epsilon\beta(s)}\cos(\Psi(s) + \phi) \tag{28}$$

where ϵ is the "transverse emittance", determined solely by the initial conditions. The "Beta function" ($\beta(s)$) and the phase advance ($\Psi(s)$) depend on the restoring force. If the oscillation amplitude, regulated by $\beta(s)$, is large, the phase advance is small. This leads

to the conclusion that the rate of phase advance is proportional to the inverse of the Beta function:

$$\frac{d\Psi(s)}{ds} = \frac{1}{\beta(s)} \tag{29}$$

Taking the derivative of x gives:

$$x' = \frac{1}{2}\frac{d\beta(s)}{ds}\sqrt{\frac{\epsilon}{\beta(s)}}\cos(\Psi(s)+\phi) - \sqrt{\frac{\epsilon}{\beta(s)}}\sin(\Psi(s)+\phi) \tag{30}$$

In the places where $\frac{d\beta(s)}{ds} = 0$, the phase space of the particle in the transverse plane is an ellipse:

$$\frac{x^2}{(\sqrt{\epsilon\beta(s)})^2} + \frac{x'^2}{(\sqrt{\epsilon/\beta(s)})^2} = 1 \tag{31}$$

As the particle moves along the accelerator, the value of $\beta(s)$ varies, which in turn changes the shape of the phase space ellipse. But the area of the ellipse remains the same ($\pi\epsilon$).

This regulation of the beam size can be better understood if we view the quadrupoles as optical lenses. The left panel of Fig. 20 shows the effects of a FODO cell on the motion of the particles along the horizontal axis. By design, the beam envelope is focused at the

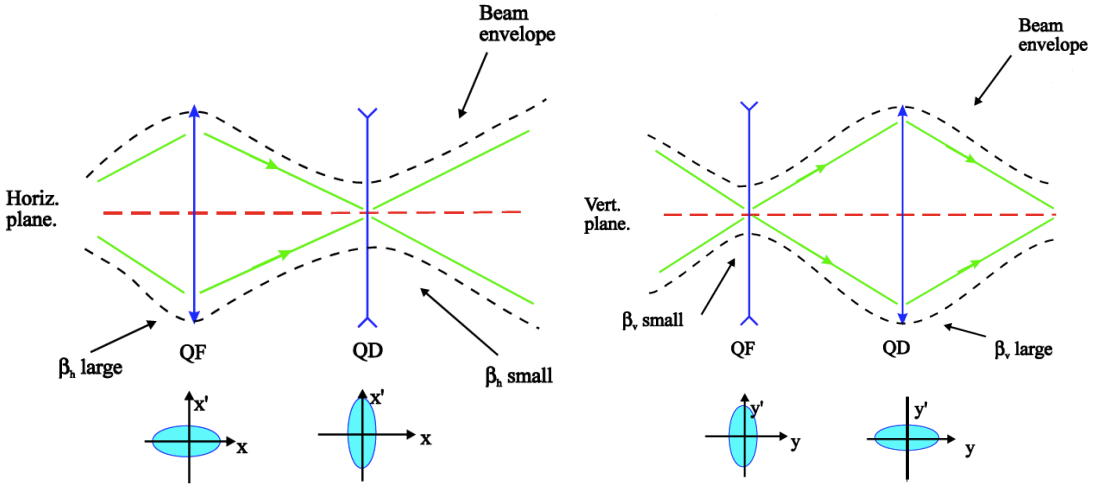

Figure 20: Effects of a FODO cell on the transverse motion of the particles in the horizontal (left) and vertical (right) directions.

QF as it goes through, but defocused at the QD. The situation is the opposite along the vertical axis as shown in the right panel of Fig. 20, namely the beam is defocused at the QF, but focused at the QD. Since the beam always travels near the center of the quadrupole

where it gets defocused, the defocusing effect is largely reduced. Therefore, the net effect of a FODO cell is to reduce the beam size along both horizontal and vertical axes.

In order to deliver beams with high luminosity, it is essential to focus the beam substantially. The key parameters that control the profile of the beam in a synchrotron are the transverse emittance (ϵ) and the beta function ($\beta(s)$). ϵ determines the overall beam profile, while $\beta(s)$ sets the maximum oscillation amplitude for a given emittance. This is particularly important because the beam has to fit the aperture of the magnets in the accelerator.

4.1.3 Radio frequency system

The magnetic field bends the particle trajectory, but it does not change the particle momentum. In order to accelerate the particles in the longitudinal direction, an electric field is needed, which can be obtained by applying a longitudinal voltage across an isolated gap in the vacuum chamber (a RF system). Usually a resonating cavity is utilized to increase the accelerating voltage. To make sure the particles see an accelerating voltage every time they arrive at the RF system, the frequency of the RF system should always be an integer multiple of the particles' revolution frequency. In reality, there are many particles circulating in the ring, and the momentum spread results in a distribution of revolution frequencies. Therefore, not all the particles are synchronized with the RF system, which could potentially cause particle loss.

Before we examine how particles with different momenta react to the RF system, we need to deduce how the revolution frequency changes with momentum. The revolution frequency is:

$$f = \frac{v}{r} \tag{32}$$

Therefore:

$$\frac{\Delta f}{f} = \frac{\Delta v}{v} - \frac{\Delta r}{r} \tag{33}$$

where v is the particle velocity and $r = 2\pi\rho$ is the orbit length. From relativity:

$$\beta = \frac{v}{c} \;\Rightarrow\; \frac{\Delta v}{v} = \frac{\Delta \beta}{\beta} \tag{34}$$

$$p = mv = m_0\gamma v = m_0\frac{1}{\sqrt{1-\beta^2}}\beta c \;\Rightarrow\; \frac{\Delta\beta}{\beta} = \frac{1}{\gamma^2}\frac{\Delta p}{p} \tag{35}$$

On the other hand, the change in the orbit length with respect to the change in the momentum is connected by the "momentum compaction factor" α_p:

$$\frac{\Delta r}{r} = \alpha_p \frac{\Delta p}{p} \tag{36}$$

Plugging in all the expressions, we have:

$$\frac{\Delta f}{f} = (\frac{1}{\gamma^2} - \alpha_p)\frac{\Delta p}{p} \tag{37}$$

At low energies, β is small and $\frac{1}{\gamma^2}$ is large, so the revolution increases as the momentum increases. This makes sense since for low energy particles, the increase in velocity is more prominent compared to the increase in momentum. The opposite is true for high energy particles.

Now, let's examine the energy evolution of two high energy particles, A and B, in the RF system, as shown in Fig. 21. Assume that whenever particle A passes through the

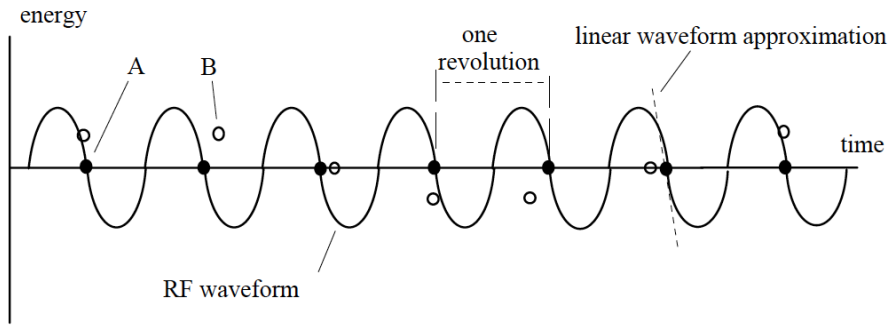

Figure 21: Energy evolution of two particles over several turns in a RF system. Accelerating (decelerating) voltage is above (below) the central line. The energy of the particles above the central line is higher than those below.

cavity, the accelerating voltage is zero. In this case, particle A is synchronized with the cavity. Particle B arrives at the cavity at the same time as A but with a slightly higher energy on the first turn. As deduced above, a higher energy particle has a smaller revolution frequency and needs longer time to finish one orbit. So on the second turn, B arrives later

than A and sees a decelerating voltage, which reduces its energy to exactly the same as A. On the third turn, B still reaches the cavity later than A since it has the same energy. Thus B is decelerated even more and has a lower energy than A after the third turn. Now particle B travels with a larger revolution frequency, and it arrives at the same time as A in the fourth turn. In this case, it sees no voltage and remains at a lower energy state compared to A. In the fifth turn, particle B arrives earlier than A and sees an accelerating force, which pushes its energy back to the same as A. Therefore, on the sixth turn particle B still reaches the cavity before A and is accelerated again. Now B has a higher energy and thus a lower frequency. On the seventh turn, it arrives at the same time as A but with a higher energy, which is exactly the same situation as we start with. As illustrated, particle B oscillates around the synchronous particle A in the RF cavity ("synchrotron oscillation"). Instead of being lost in the cavity due to momentum spread, particles are trapped by the RF system in forms of synchrotron oscillation. But there is a limit of momentum spread for the particles that can be trapped by the cavity, which largely depends on the RF voltage.

In the discussion above, the energy of the particles is not increased in the RF cavity (particle A). If we increase the magnetic field smoothly with the RF on, the particles will follow a shorter path, hence arrive earlier at the RF. This looks exactly as if they have lost energy and increased the revolution frequency. The RF cavity compensates the apparent energy loss and puts the particles back on the correct frequency. In this way, the RF system accelerates the particles in the beam.

4.1.4 Injection chain

Protons and lead ions are sent to the LHC via slightly different injection chains, as shown in Fig. 22 [67]. Protons are produced using a duoplasmatram from hydrogen gas, and extracted in pulses. After being accelerated and focused through a radio frequency quadrupole, they are sent to a linear accelerator (LINAC 2), which increases the proton energy to 50 MeV. Then the proton pulses are transferred into the proton synchrotron booster (PS Booster), in which the protons travel in a closed orbit and are consistently focused as well as accelerated. Leaving the PS Booster at a energy of 1.4 GeV, the proton beam continues to circulate in the proton synchrotron (PS), gaining additional energy to reach 25 GeV. The beam is then

injected into the super proton synchrotron (SPS), and accelerated further to 450 GeV. Finally the beam leaves the SPS, and enters the LHC, in which it reaches an energy up to 7 TeV.

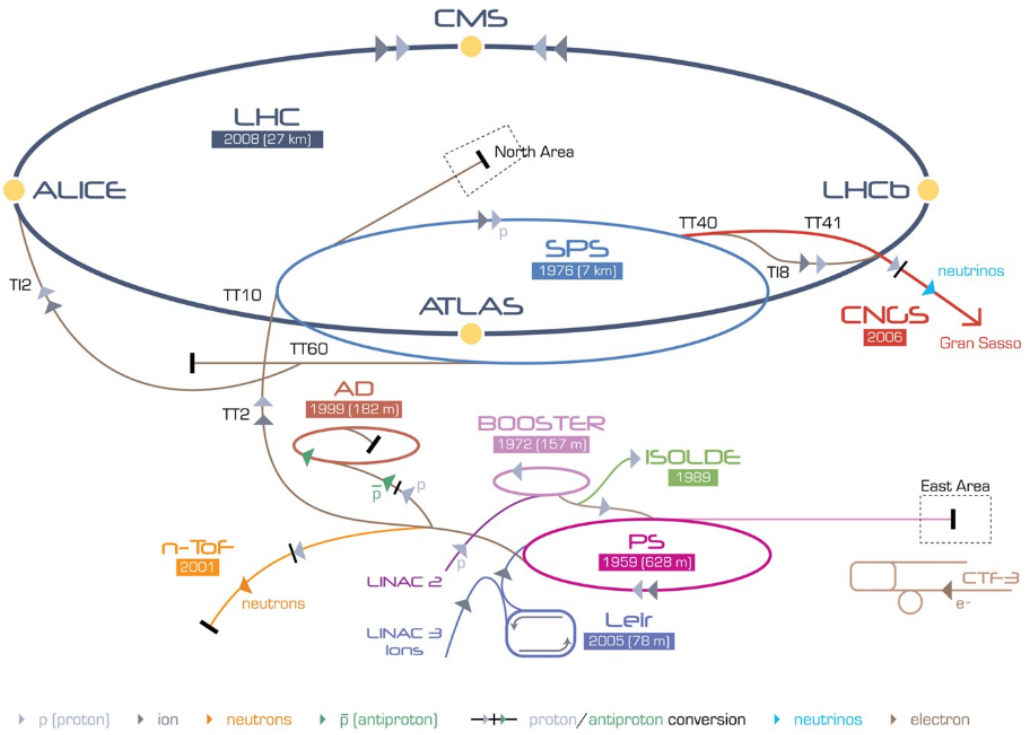

Figure 22: The layout of the LHC injection chain for protons and lead ions.

The injection chain for the lead ion is a bit different in the early stage of the operation. The lead ions start from a source of vaporized lead (Pb^{27+}) with energy 2.5 KeV/n (per nucleon) and enter a different linear accelerator, LINAC 3. After traveling through LINAC 3 (Pb^{54+}, 4.2 MeV/n), they are collected, accelerated and spaced in the low energy ion ring (LEIR). Leaving LEIR with energy 72 MeV/n (Pb^{54+}), the ion beam then follows exactly the same route to the maximum energy as the protons: PS (Pb^{54+}, 6 GeV/n) $\rightarrow$ SPS (Pb^{82+}, 177 GeV/n) $\rightarrow$ LHC (Pb^{82+}, up to 2.76 TeV/n).

4.2 ALICE

ALICE at the LHC is a large general-purpose experiment built specifically to investigate the properties of the QGP [34]. Its layout is shown in Fig. 23, where all the main sub-detectors are labelled. The coordinate system used by ALICE is a right-handed Cartesian system,

with the interaction point (IP) located at the center of the detector as the origin. The z-axis is along the beam direction, pointing away from the muon spectrometer. The x-axis is perpendicular to the z-axis and points to the accelerator center, while the y-axis points upward and is perpendicular to both x and z axes.

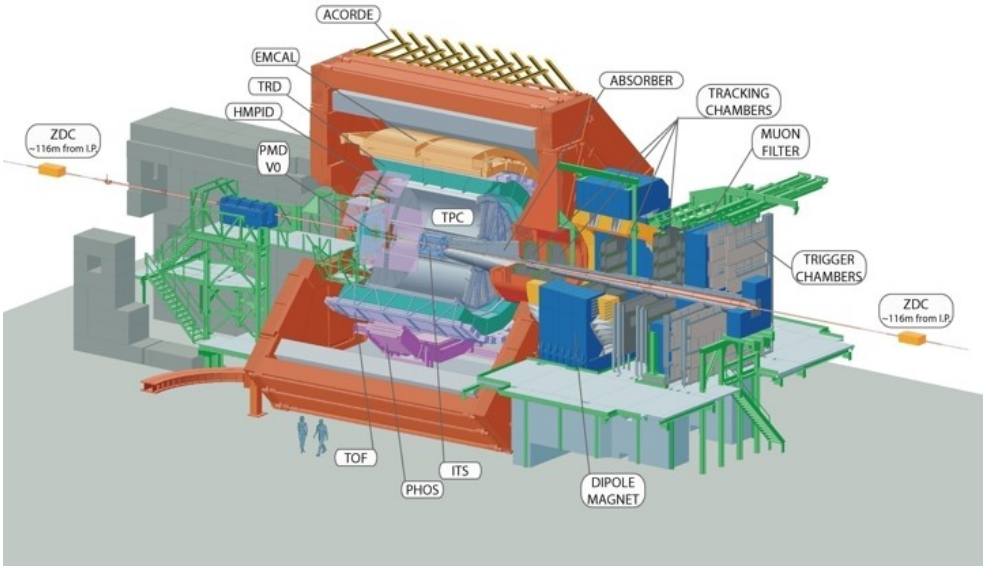

Figure 23: The layout of the ALICE detector at the LHC.

A muon spectrometer [70] is used to detect and identify muons to study open heavy flavor and quarkonia productions via muon-decay channels. It covers a pseudo-rapidity range of $-4.0 < \eta < -2.4$, and consists of five components: an absorber, a dipole magnet, tracking chambers, a muon filter and trigger chambers.

At mid-rapidity ($|\eta| < 0.9$), hadrons, photons and electrons are measured and identified in a series of detectors with different technologies immersed in a moderate magnetic field (0.5 T). The momentum of the charged particles is measured by three high-granularity detectors at different radii covering full azimuth: the Inner Tracking System (ITS) [71] consisting of six layers of silicon detectors and closest to the IP; the large-volume Time Projection Chamber (TPC) [72], a gaseous three-dimensional tracking chamber outside of the ITS; and the Transition Radiation Detector (TRD) [73] just outside the TPC. The identification of charged particles uses different techniques: specific energy loss (dE/dx) in the ITS and TPC; transition radiation in the TRD; time-of-flight of the particles using a high-resolution Time-

Of-Flight (TOF) detector [74]; and Cherenkov radiation with a High-Momentum Particle Identification Detector (HMPID) [75]. All these measurements combine together to provide excellent identification of pions, kaons, protons and electrons over a broad kinematic range. The energy measurement and identification of neutral pions and photons are realized in a crystal PHOton Spectrometer (PHOS) [76] and an ElectroMagnetic Calorimeter (EMCal) [77, 78], which cover different azimuthal (PHOS: $220^\circ < \varphi < 320^\circ$, EMCal: $80^\circ < \varphi < 180^\circ$) and pseudo-rapidity acceptances (PHOS: $|\eta| < 0.12$, EMCal: $|\eta| < 0.7$). Specifically, the EMCal extends the electron identification capability in ALICE to high momentum.

Additional detectors located at larger pseudo-rapidities are complementary to the central detectors for characterizing events and providing interaction triggers. The Forward Multiplicity Detector (FMD) [79] measures the charged particle multiplicity in the pseudo-rapidity ranges $-3.4 < \eta < -1.7$ and $1.7 < \eta < 5.1$, which allows for study of the multiplicity fluctuations on an event-by-event basis. Another forward detector, the Photon Multiplicity Detector (PMD) [80], measures the multiplicity and spatial distribution of photons in the range $2.3 < \eta < 3.5$. The T0 detector [81], consisting of two arrays of Cherenkov counters, is mounted to cover $-5 < \eta < -4.5$ and $2.9 < \eta < 3.3$. It measures the starting time of a collision (with a fixed time delay), which is then fed back to the TOF to calculate particles' time-of-flight. Two arrays of scintillators compose the VZERO detector [81], covering the full azimuth over $2.8 < \eta < 5.1$ (VZERO-A) and $-3.7 < \eta < -1.7$ (VZERO-C), which is mainly used to provide interaction triggers. The Zero-Degree Calorimeter (ZDC) [82], sitting at 116 m away from the IP, detects the spectator neutrons at beam rapidity.

For the jet measurement, the charged constituents are detected by the ITS and TPC, and most of the neutral constituents are measured in the EMCal. These most relevant sub-detectors are discussed in detail in the following sections.

4.2.1 Inner Tracking System

The ITS (see Fig. 24) is located closest to the IP, and is made up of six cylindrical layers of silicon detectors [71]. It covers the central rapidity range ($|\eta| < 0.9$) for interactions whose vertices are located within 10.6 cm ($\pm 1\sigma$) of the nominal IP along the beam direction. The main functionalities of the ITS are to: 1) determine the primary vertex of the triggered

collisions; 2) provide dE/dx measurements, especially for low momentum tracks; 3) extend the track trajectory between the TPC and the IP.

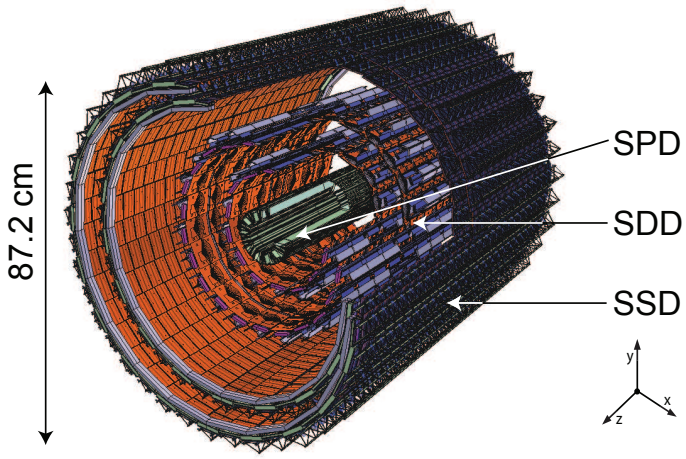

Figure 24: The layout of the ITS.

In principle, a silicon detector is a solid state ionization chamber, taking advantage of the special material structure of a semiconductor. For semiconductors, a junction between p-type and n-type silicon creates a diode, in which a depletion region is built up due to the diffusion of majority carriers across the interface. When an external reverse-biased voltage is applied, a diode can be fully depleted of free carriers, which is usually the working state of a silicon detector. As shown in Fig. 25, when a charged particle traverses a silicon detector, it ionizes the silicon and creates thousands of electron-hole pairs. Driven by the electric field, the holes are collected on the p-side and electrons on the n-side. A signal of the passing particle is therefore generated. The diodes used in real-life experiments are usually manufactured by implanting different shapes of p^+-type silicon on an n-type bulk.

The Silicon Pixel Detectors (SPD) [71] comprise the two innermost layers of the ITS and are located at an average distance of 3.9 cm and 7.6 cm from the beam axis, respectively. It is made from hybrid silicon pixels in the form of two dimensional matrices of reverse-biased diodes. A pixel cell is 50 μm in the $r\varphi$ direction and 425 μm in the z direction. The resulting spatial precision is 12 (100) μm and the two-track resolution is 100 (850) μm in the $r\varphi$ (z) direction. In total, there are 9.8M pixel cells, which ensures large acceptance coverage and high granularity. The SPD is able to determine the primary vertices of the interactions

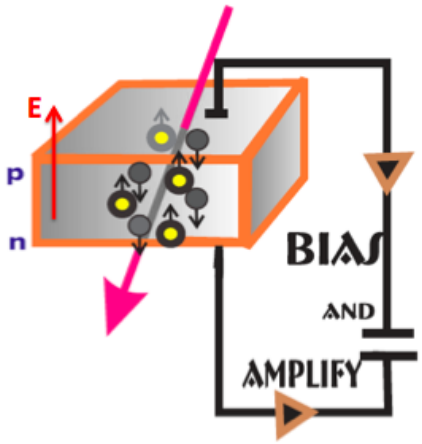

Figure 25: Working principle of a silicon detector. An external voltage is applied to fully deplete the diode, and creates an electric field causing the electron-hole pairs to migrate. The dark gray circles with yellow inside represent holes, while the solid gray circles are electrons.

with resolution better than 100 μm, and contribute to the tracking of charged particles by providing the first two points on their trajectories. The average amount of material experienced by a straight track perpendicular to the SPD is about 1% of a radiation length per layer. The read-out of the SPD is logical, therefore it does not provide any information for the energy loss measurements. One unique feature of the SPD is that it generates a prompt trigger based on an internal Fast-OR, which is widely used in the current trigger configuration deployed by ALICE.

The intermediate two layers of the ITS are equipped with silicon drift detectors (SDD) [71, 83] for its good multi-track capability and energy loss sampling ability. They sit at average radii of 15.0 cm and 23.9 cm, respectively. The schematic working principle of a silicon drift detector is shown in Fig. 26. Unlike the pixel detectors where rectangular p^+-

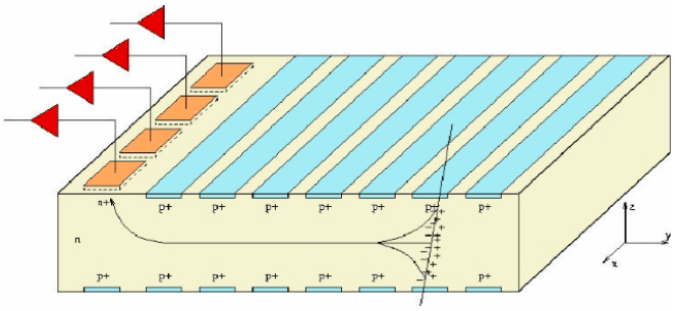

Figure 26: Schematic working principle of a silicon drift detector.

type silicon is implanted on one side, strips of p^+-type silicon are attached to the n-type bulk on both sides. These p^+ strips are used to fully deplete the detector volume and generate an electric drift field parallel to the surface. When a charged particle goes through the sensitive volume, pairs of electrons and holes are produced during ionization. The holes are collected by the nearest p^+ electrode, while the electrons are forced into the middle plane and drift to the edge of the detector in the electric field. An array of anodes made from n^+ pads along the edge collects the electrons and sends the signals to next-level electronics. Due to the diffusion and the repulsive forces, the electrons reach the anodes with a Gaussian distribution spreading over multiple anodes. The coordinate perpendicular to the drifting direction can be reconstructed as the centroid of the collected charges in all the anodes, whose resolution is much better than the size of the anode itself. The coordinate along the drift direction is calculated using the drift time of the charge centroid given that the drift velocity is constant. In this way, a silicon drift detector can measure two coordinates of the passing particle. Furthermore, the number of generated electron-hole pairs is proportional to the energy of the incoming particles, which makes the energy loss measurements possible via the amplitude of the electronic signals. The layout of the SDD used in ALICE is shown in Fig. 27, where the sensitive volume is divided into two regions by the central cathode strip with a nominal bias voltage of -2.4 kV. The nominal drift velocity is 8.1 μm/ns, and

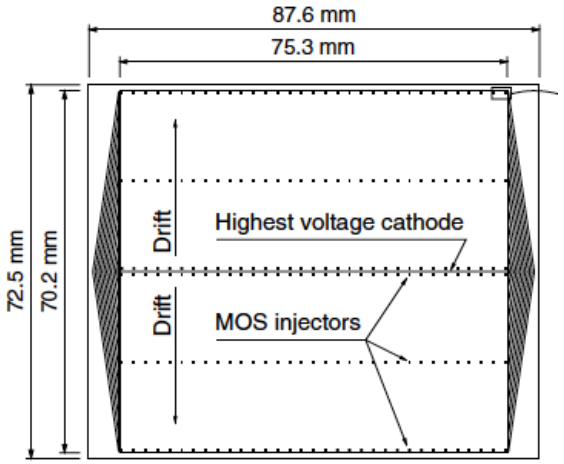

Figure 27: Layout of the SDD. The sensitive area of 75.3×70.2 mm^2 is split into two drift region by the central cathode.

varies with the temperature under which the detector is operated. The nominal maximum

drift time is 4.3 μs, which is relatively slow. Nevertheless, it is suitable in this case since ALICE is designed to take high multiplicity events with relatively low event rates. The SDD is aligned such that the drifting direction is along the bending direction of the charged particles. The average position resolutions along the drift direction ($r\varphi$) and anode axis (z) are 35 μm and 25 μm, respectively. The two-track resolution is 200 (600) μm in the $r\varphi$ (z) direction. The material budget amounts to 1.13% of a radiation length per layer.

Double-sided silicon strip detectors (SSD) [71] are used for the two outer layers of the ITS where the requirement for the granularity is less stringent. The two layers are located at average radii of 38 cm and 43 cm. The SSD makes the connection for track reconstruction between the ITS and TPC, and provides energy loss measurement needed for particle identification along with the SDD. The working principle of a double-sided silicon strip detector is shown in the left panel of Fig. 28. P^+-type and n^+-type silicon strips are implanted on both sides of the n-type bulk. Once a charged particle passes by the sensitive volume, ionized electrons and holes are collected at the n^+-type and p^+-type strips, respectively. Thus, signals are produced on both sides, which can be used to measure both the position and the energy of the particles. The actual alignment of the n^+-type and

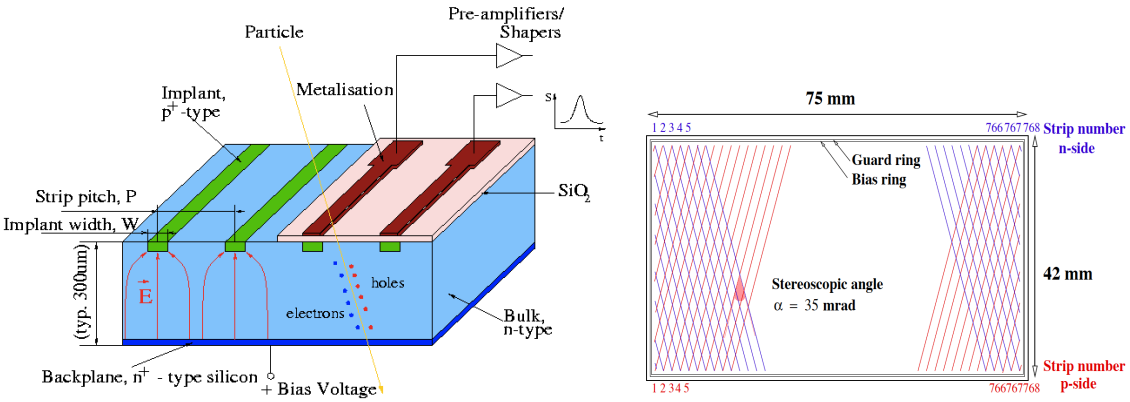

Figure 28: Left: the working principle of a double-sided silicon strip detector. Right: the alignment of the strips employed by the SSD in ALICE.

p^+-type strips in ALICE is shown on the right panel of Fig. 28. The impact points of the passing particles are reconstructed by associating hits from both n^+-type and p^+-type strips [84]. The correlation between the amplitudes of the signals produced on both sides

is utilized to reduce "ghosts", namely the false association. A small stereoscopic angle (35 mrad) is optimized to reduce the number of ambiguous associations in the high particle-density environment. Due to the alignment, the spatial resolution perpendicular to the strips is much better than along the strips. Therefore, the strips are mounted along the beam direction such that the best position resolution is achieved in the bending direction. Spatial resolution of 20 (830) μm, and two-track resolution of 300 (2400) μm are achieved along the $r\varphi$ (z) direction. The material budge is about 0.8% of a radiation length for each SSD layer.

4.2.2 Time Projection Chamber

After traversing the ITS, the charged particles continue to travel in the TPC [72], which is a gaseous drift chamber measuring momenta and energy loss of the traversing particles. In ALICE, the magnetic field ($\vec{B} = B\vec{z}$) along the beam direction bends the charged particles in the xy (or $r\varphi$) plane. The transverse momentum of the bending particle is given by (see Eq. 24):

$$p_T = qB\rho \tag{38}$$

Therefore, by measuring the radius of the circle along which the particle bends, we can deduce the transverse momentum of the particle. However, what is really measured in the TPC is the sagitta of the trajectories, shown as "s" in Fig. 29. It relates to the radius as:

$$s = \rho - \rho\cos(\theta/2) \tag{39}$$

If the radius is much larger than the distance over which the trajectory is measured ($\rho >> L$), θ is small and can be approximated as:

$$\theta \approx 2\sin(\theta/2) = 2\frac{L/2}{\rho} = L/\rho \tag{40}$$

Plug in $\cos(\theta/2) = 1 - 2\sin^2(\theta/4)$, we get

$$s = 2\rho\sin^2(\theta/4) \approx \rho\frac{\theta^2}{8} \approx \frac{L^2}{8\rho} \tag{41}$$

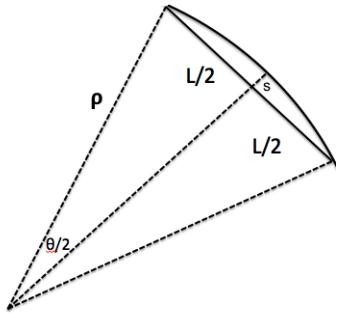

Figure 29: Particle trajectory in a magnetic field. The sagitta "s" is measured in the TPC.

The p_{T} resolution coming from the sagitta measurement is:

$$\frac{\Delta p_{\mathrm{T}}}{p_{\mathrm{T}}} = \frac{\Delta s}{s} \approx \frac{8\rho}{L^2}\Delta s = \frac{8p_{\mathrm{T}}}{qBL^2}\Delta s \tag{42}$$

Larger distance (L), larger magnetic field and better resolution on the sagitta measurement would all result in a better momentum resolution. An additional contribution to the momentum resolution is the multiple scattering between the incident particles and the medium (i.e. gas for TPC), which motivates minimal material budget for the device. This is particularly important for low momentum particles since the multiple scattering is the dominant source of the resolution.

Particle identification in a drift chamber utilizes the energy loss of the particle in the medium during traversal. The mean energy loss for a charged particle in intermediate-Z medium is well described by the Bethe-Bloch formula in the region $0.1 < \beta\gamma < 1000$ [85]:

$$-\langle\frac{dE}{dx}\rangle = Kz^2\frac{Z}{A}\frac{1}{\beta^2}[\frac{1}{2}\ln\frac{2m_ec^2\beta^2\gamma^2T_{max}}{I^2} - \beta^2 - \frac{\delta(\beta\gamma)}{2}] \tag{43}$$

where

- $K = 4\pi N_A r_e^2 m_e c^2 = 0.307$ MeV g^{-1} cm^2
- N_A is Avogardo's number
- $r_e = 2.8$ fm is the classical electron radius
- $m_e c^2 = 0.51$ MeV is the electron mass

- z is the charge of the incident particle
- Z is the atomic number of the medium
- A is the atomic mass of the medium
- I is the mean excitation energy of the medium
- $T_{max} = 2m_e c^2\beta^2\gamma^2/(1 + 2\gamma m_e/M + (m_e/M)^2)$ is the maximum energy that could be imparted to a free electron from the incident particle in a single collision
- M is the mass of the incident particle
- $\beta = v/c$ is the velocity of the incident particle
- $\gamma = \frac{1}{\sqrt{1-\beta^2}}$ is the Lorentz factor
- $\delta(\beta\gamma)$ is the density effect correction to the ionization energy loss

A minor dependence on the mass of the incident particle is introduced through T_{max} at highest energies. For all the practical measurements, $\langle\frac{dE}{dx}\rangle$ is only dependent on β. An example of the energy loss measurement is shown in Fig. 30 for charged pions in copper [85]. There are three distinguished regions: i) at low velocity, the energy loss decreases: $-\langle\frac{dE}{dx}\rangle \propto \frac{1}{\beta^2}$; ii) at $\beta\gamma \sim 3 - 4$, the minimum energy loss is reached and a particle in this region is called a "Minimum Ionizing Particle (MIP)"; iii) at high velocity, the energy loss undergoes a relativistic rise: $-\langle\frac{dE}{dx}\rangle \propto \ln\beta$, which is compensated by the correction factor $\delta(\beta\gamma)$. In the drift chamber, the energy evolution of the particle along the trajectory can be measured via the magnitude of the signals induced by the particle at each sampling point, which is in turn used to calculate the energy loss. In practice, the mean of the energy loss is affected strongly by rare processes where large energy deposition happens in a single scattering. To overcome this instability, a truncated mean is usually used, which is the mean of a pre-defined fraction of the dE/dx measurements at the lower end. By plotting the mean energy loss as a function of the momentum instead of β, the distributions for different particle species can be separated in certain momentum regions.

As the main tracking detector in ALICE, the TPC is the largest time projection chamber that has been built. Its layout is shown in Fig. 31. It measures 5 meters in the beam (z)

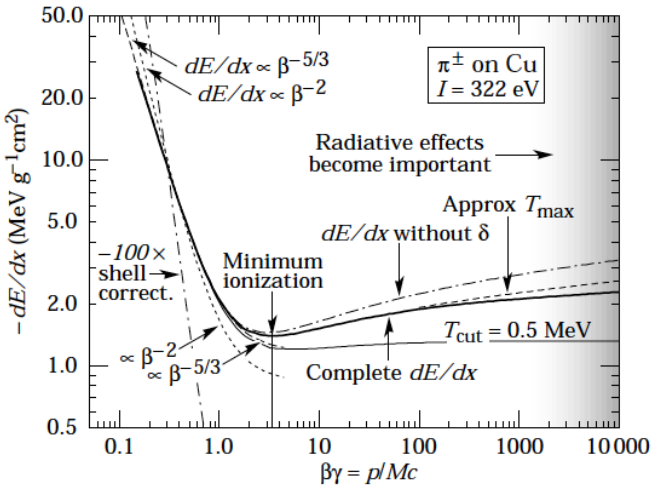

Figure 30: Mean energy loss of charged pions in copper as a function of $\beta\gamma$.

direction, and has a cylindrical structure with inner and outer radii of 0.85 and 2.5 meters respectively for the active volume. The central electrode divides the active volume into two

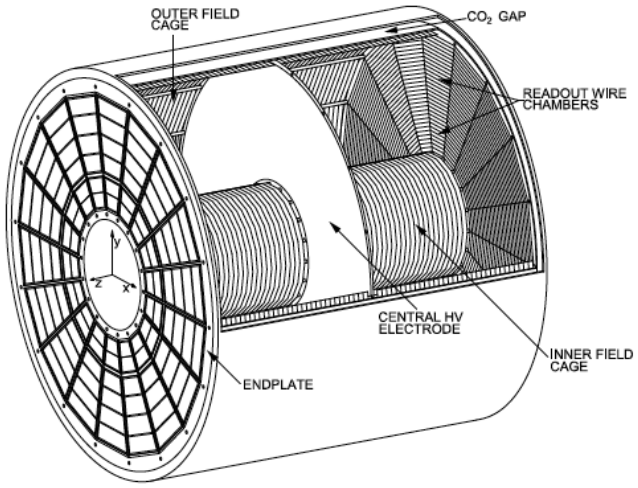

Figure 31: The layout of the ALICE TPC.

identical drift regions and is charged to -100 kV during nominal operation. A total of 72 rods are placed axially on the internal walls of the inner and outer field cage. They are used to hold the field cage strips, which define a highly uniform electric field of 400 V/cm in the drift volume. The containment vessels surrounding the field cage vessels are used to provide gas tight and grounded enclosures. They are separated from the field cage using CO_2. The volume of the gas, which is a mixture of Ne-CO_2-N_2 (85.7-9.5-4.8), contained in the drift

region is 90 m^3. The choice of the gas mixture is a compromise between drift velocity, space charge effects, aging, cost, etc. As the incident charged particle goes through the active volume, it loses energy by ionizing the gas, and produces electron-ion pairs whose number is proportional to the energy of the particle. Driven by the electric field, the free electrons drift towards the endplates with a constant velocity of about 2.65 cm/μs (for the chamber gas used). The drift time from the center to the endplate is about 90 μs, which limits the readout rate of the TPC.

The readout system adopts Multiple Wire Proportional Chambers (MWPC) [86] with cathode pads, as shown in Fig. 32. When the TPC is in the readout mode, the electrons

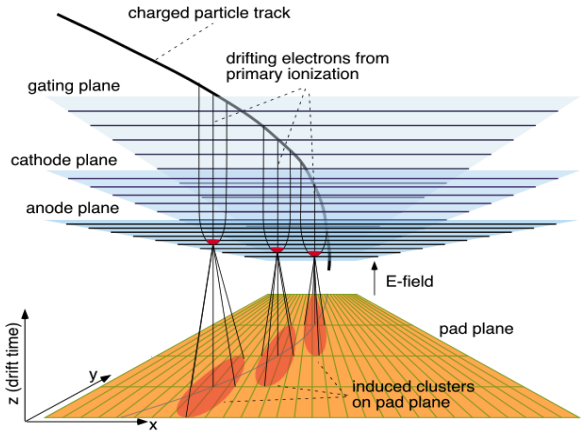

Figure 32: The MWPC readout system of the TPC.

enter the amplification region through the "open" gating grid, namely all the wires are held at the nominal potential defined by the electric field. In the amplification region, the electrons are accelerated near the anode wires and start avalanche processes, during which thousands more electron-ion pairs are produced per parent electron. The signals induced on the readout pads are therefore largely amplified and the signal-to-noise ratio is greatly enhanced. Along with the electrons, a large number of ions are also produced in the avalanche processes. Without further treatment, they would drift back into the active volume and distort the uniformity of the electric field ("space charge" effects [87]). The main mechanism to overcome this problem is to "close" the gating grid, during which the gating wires are biased with a bipolar potential such that they are nontransparent to the electrons in the drift region and the ions in the amplification region. Furthermore, the cathode wires

collect the ions produced in the avalanche amplification. As shown in Fig. 32, the trajectory of the incident particle in the xy plane is given by the signals on the readout pads, while the z-coordinate is given by the drift time as the drift velocity is constant: $z = v_{drift} \times t_{drift}$. Since the drift velocity of the electrons is very sensitive to the temperature, the variation of the temperature throughout the entire TPC volume should be controlled within 0.1 K. For the dE/dx sampling, 70% of the distribution is used to calculate the truncated mean. An example of the energy loss measurement in Pb–Pb collisions is shown in Fig. 33.

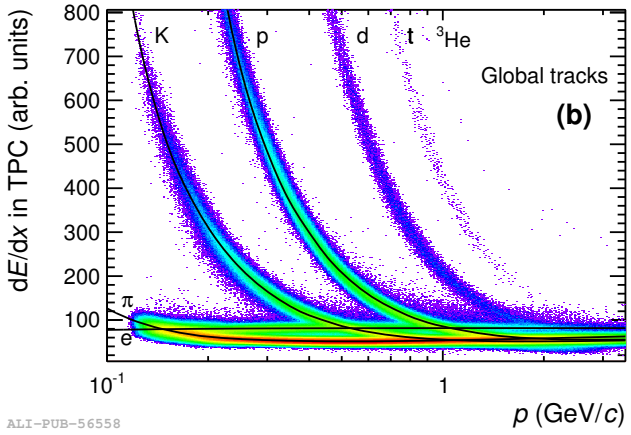

Figure 33: Mean energy loss as a function of momentum measured using the TPC for various charged-particle species in Pb–Pb collisions at $\sqrt{s_{\rm NN}}$= 2.76 TeV.

4.2.3 Electromagnetic Calorimeter

The EMCal [77] is used to measure the energy of the electrons and photons through electromagnetic showers. The average energy loss by electrons in lead is shown in the left panel of Fig. 34 [88]. In the low energy region ($E \lesssim 10$ MeV), the ionization process dominates, while bremsstrahlung is the main mechanism for energy loss at higher energies ($E > 10$ MeV). On the other hand, as shown in the right panel of Fig. 34 [89], the photons lose energy in matter predominantly via Compton scattering at low energies ($E < 5$ MeV), and electron-positron pair production at higher energies. In the energy region in which ALICE experiment is most interested ($E > 100$ MeV), electrons produce secondary photons via bremsstrahlung and photons produce secondary electrons and positrons by pair production. These secondary particles undergo the same mechanism to produce more photons and

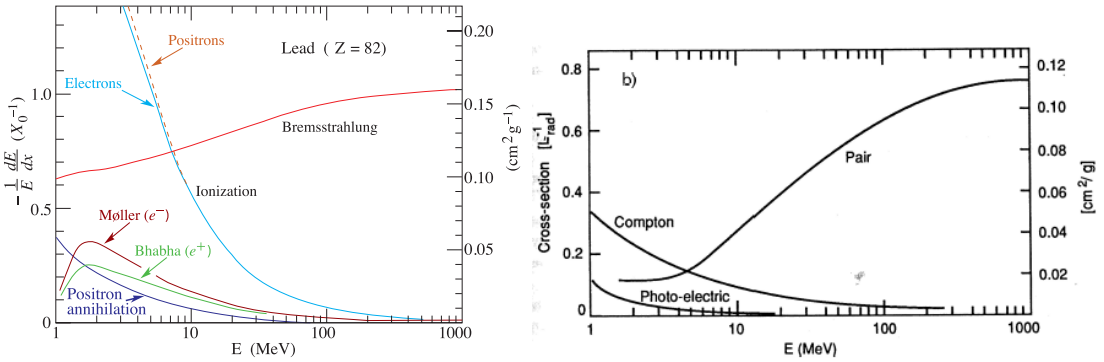

Figure 34: Left: mean energy loss of electrons in lead as a function of the electron energy. Right: cross section of different processes for photons interacting with matter.

electron-positron pairs with progressively degraded energies, thus giving rise to a cascade (shower). The shower stops when the energy of the electrons falls below a critical energy, where ionization and excitation become the main process of energy dissipation. An example of an electromagnetic shower initiated by a positron is shown in Fig. 35

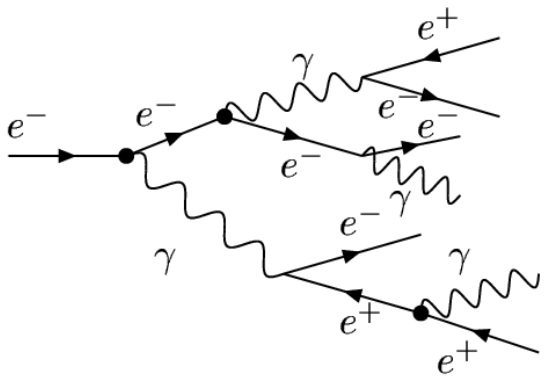

Figure 35: Schematic profile of an electromagnetic shower initiated by a positron.

The radiation length X_0 can be approximated as [85]:

$$X_0 \approx \frac{716 \cdot A}{Z(Z+1)\ln(287/\sqrt{Z})}\ \mathrm{g \cdot cm^{-2}} \tag{44}$$

where Z and A are the atomic number and atomic mass of the material. It represents the mean distance over which a high energy electron reduces its energy to $1/e$ of its original energy via bremsstrahlung. It is also 7/9 of the mean free path for electron-positron pair

production by a high energy photon. Another useful parameter is the critical energy E_c, which is defined as the energy at which the electron ionization loss equals bremsstrahlung loss. An approximation to the critical energy is [85]:

$$E_c \approx \frac{800}{Z+1}\text{MeV} \tag{45}$$

Usually two variables are used to quantify electromagnetic showers. The first is the shower maximum depth, i.e. the depth at which the largest number of secondary particles is produced, which is approximately located at [85, 90]:

$$d = X_0 \times (\ln \frac{E}{E_c} + C_j)\ \text{g} \cdot \text{cm}^{-2} \tag{46}$$

where E is the energy of the incoming particle, and $C_j = -0.5(+0.5)$ for electrons (photons). It quantifies the longitudinal profile of the shower. Since the bremsstrahlung cross section is larger than pair production, the shower initiated by an electron develops earlier in the material than that by a photon. The second variable is the Molière radius (R_M) which is used to quantify the transverse size of the shower [91]:

$$R_M \approx X_0 \times \frac{21(\text{MeV})}{E_c}\ \text{g} \cdot \text{cm}^{-2} \tag{47}$$

On average, about 90% of the shower energy is contained in a cylinder of radius R_M. The main contribution to the transverse spread is the multiple scatterings of electrons and positrons off the material.

The ALICE EMCal is a Pb-scintillator sampling calorimeter covering $80^\circ < \varphi < 180^\circ$ and $|\eta| < 0.7$ using ten full-size super modules (SM) in the 2011 data taking. Each SM spans $\Delta\varphi = 20^\circ$ and $\Delta\eta = 0.7$. The arrangement of the SM's is shown in the left panel of Fig. 36, where the two small 1/3 SM's are also shown. The small SM's were installed in early 2012, and extend the EMCal coverage by another 7° in azimuth. An end view of the EMCal in 2011, after ten full-size SM's were installed, is shown in the right panel of Fig. 36 along with other sub-detectors. Each full-size SM is made of 24×12 modules, and a module contains 2×2 towers. The profile of the mechanical structure of a module is shown

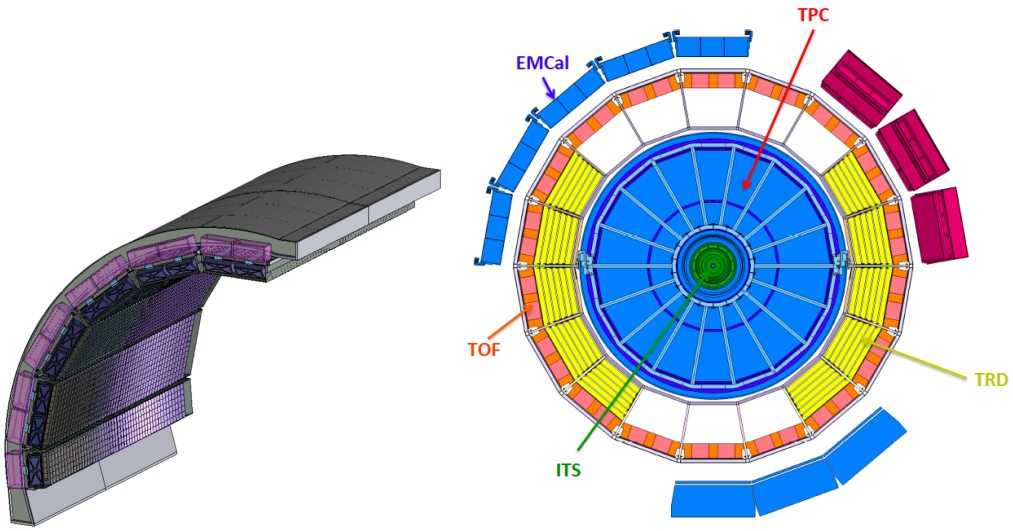

Figure 36: Left: arrangement of the EMCal SM's, including ten full size and two one-third size. Right: end view of the EMCal in 2011 along with other main sub-detectors in ALICE.

in Fig. 37, which contains in total 20 parts and 831 components.

A tower is the building block that detects the energy deposition in the EMCal. It measures 6 cm $\times$ 6 cm in cross-section and 24.6 cm long. Each tower is constructed of 76 layers of Pb with 1.44 mm pitch interleaved between 77 layers of scintillators with 1.76 mm pitch. The Pb layers act as absorbers to degrade the energy of incoming particles via induced electromagnetic showers, while the scintillator layers are the active volume that converts the energy deposited by the incoming particles into light. The name "sampling calorimeter" comes from the fact that only the energy deposited in the active volume is measured, which is a fraction of the energy of the incident particle. With the $\sim 1:1.22$ Pb to scintillator volume ratio, the effective radiation length is 1.23 mm giving rise to the detector thickness of $20.1X_0$. The critical energy for the EMCal is $E_c \sim 8$ MeV, and the shower maximum depth is about $10X_0$ for a 100 GeV photon. The Molière radius is about 3.2 cm, which means the transverse size of an electromagnetic shower is close to the size of a tower.

The relative energy resolution of the EMCal can be parameterized as [92]:

$$\frac{\sigma}{E} = \frac{a}{E} \oplus \frac{b}{\sqrt{E}} \oplus c \tag{48}$$

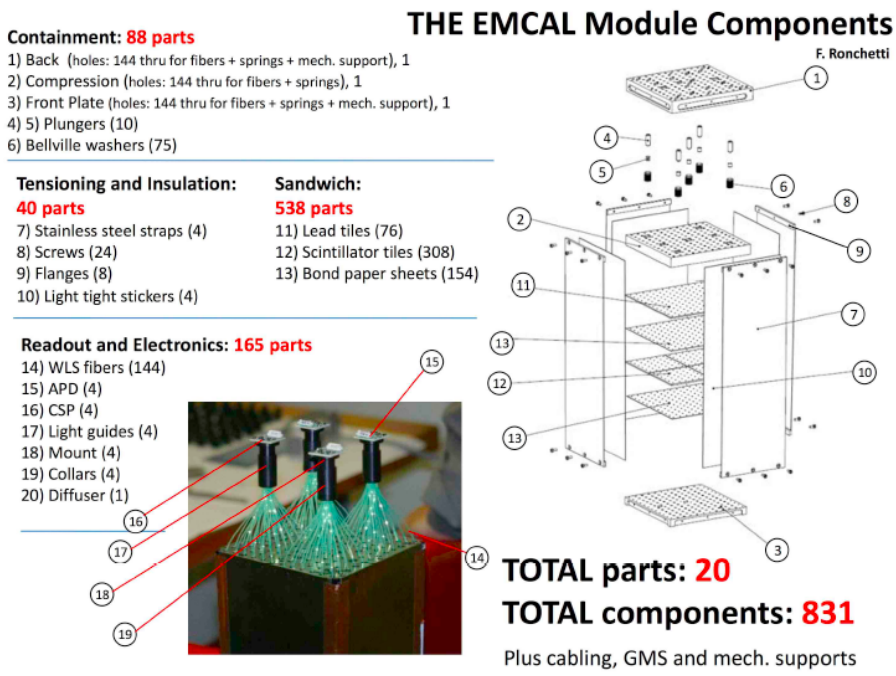

Figure 37: Mechanical structure of an EMCal module.

where E is the shower energy. The first term, a, arises from the electronic noise of the readout system, and depends on the features of the readout circuit. The second term, b, originates from the stochastic processes involved in the measurement, e.g. the number of particles produced in the shower, the fraction of energy sampled by the active volume, the conversion of light to electrons, etc. The third term, c, is independent of the shower energy, and mainly comes from the systematic effects, such as detector response non-uniformity, calibration errors, etc. The EMCal resolution is measured using the 2010 test beam and fitted with the parametrization (Eq. 48), as shown in Fig. 38. A relative energy resolution of about 4% is achieved for 10 GeV showers.

The naming convention for the ten SM's in the EMCal is shown in Fig. 39, where the labeling runs from positive η to negative η, and from small φ to large φ.

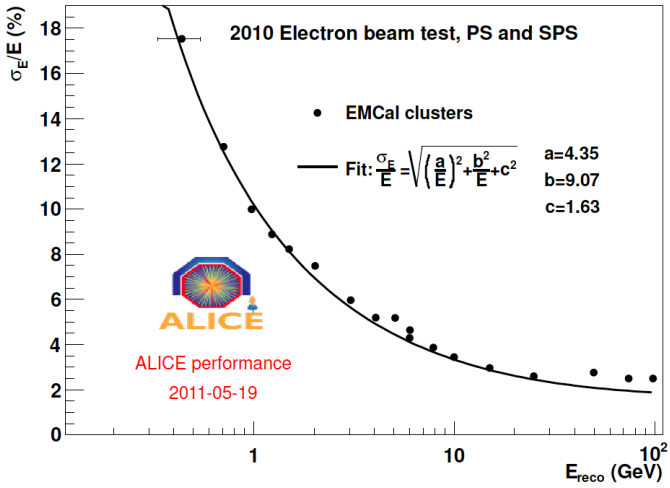

Figure 38: Energy resolution of the EMCal measured using the 2010 test beam.

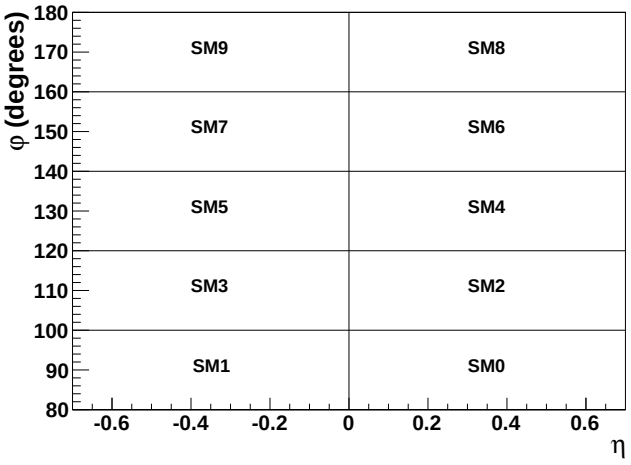

Figure 39: Naming convention for the ten SM's in the EMCal.

5 Jet cross section in pp collisions

In March 2011, the LHC delivered a three-day run with pp collisions at $\sqrt{s} = 2.76$ TeV, the same per nucleon-nucleon center-of-mass energy as the available Pb–Pb data up to 2013. The jet cross section measurement using this brief run offers a unique opportunity to test QCD calculations in an unprecedented energy regime. Since the QGP is not expected to be created in the small pp system, the measurement also serves as the baseline for the same analysis in the Pb–Pb collisions for investigating the modification to the jets by the medium.

The recipe used to measure the jet cross section is the following:

$$\frac{\mathrm{d}\sigma^{\mathrm{jet}}}{\mathrm{d}p_{\mathrm{T}}} = \frac{\mathrm{d}N^{\mathrm{jet}}_{\mathrm{raw}}}{\mathrm{d}p_{\mathrm{T}}} \times \frac{A_{\mathrm{trigger}}}{\epsilon_{\mathrm{trigger}}\left(p_{\mathrm{T}}\right)} \times C_{\mathrm{MC}} \times \frac{1}{A\left(p_{\mathrm{T}}\right)} \times \frac{1}{L_{\mathrm{int}}} \tag{49}$$

where

- $\frac{\mathrm{d}N^{\mathrm{jet}}_{\mathrm{raw}}}{\mathrm{d}p_{\mathrm{T}}}$ is the raw jet yield in data.
- $\epsilon_{\mathrm{trigger}}\left(p_{\mathrm{T}}\right)$ is the efficiency of the event triggers for the jet production.
- A_{trigger} is the acceptance of the event triggers. It corrects for the inefficiency of the trigger itself, which is mainly due to the non-functioning electronics.
- C_{MC} is used to correct for all the detector effects that distort the jet spectrum, such that the results can be compared to other experiments and theoretical calculations.
- $A\left(p_{\mathrm{T}}\right)$ corrects for the detector acceptance and is obtained via geometrical scaling.
- L_{int} is the integrated luminosity sampled by the data set used.

In the following chapters, the determination of each component is discussed.

6 Jet raw yield

6.1 Event selection

The data were taken by the ALICE detector for pp collisions, and several trigger detectors were utilized: VZERO, SPD and EMCal. The EMCal Single Shower (SSh) trigger system generates an energy sum for overlapping groups of 4×4 ($\eta \times \varphi$) adjacent EMCal towers, followed by comparison to a threshold energy. Two different trigger conditions were used to initiate event recording: (i) the Minimum-Bias (MB) trigger requiring a signal in either the VZERO-A, VZERO-C or SPD, in coincidence with the presence of a bunch crossing, and (ii) the EMCal SSh trigger, which requires that the MB trigger condition is satisfied and that at least one SSh sum exceeds a nominal threshold energy of 3 GeV. Due to the improperly functioning Trigger Region Units (TRU) [77], about 10% of the trigger system is masked out in the offline analysis. This is shown in Fig. 40, where the empty areas correspond to the masked regions. Any accepted triggered event for analysis is required to

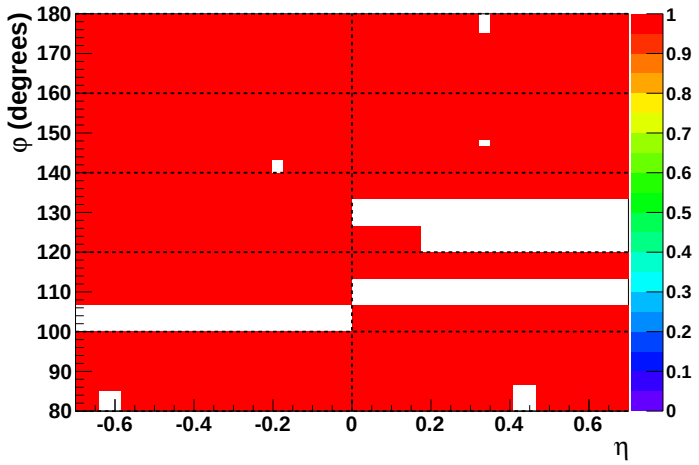

Figure 40: Trigger mask used to select good EMCal-triggered events for offline analysis. The empty areas correspond to the regions that are masked out. The trigger mask is extracted from data.

contain at least one valid SSh overlapping with an EMCal cluster (see section 6.3) that has passed quality cuts.

An LED system is incorporated into the EMCal for calibration purposes. LED events are events contaminated by the LED signals during data taking, and should be rejected. To

identify the LED events, the number of towers with energy deposition more than 0.1 GeV in each SM is used as the discriminator, and the distributions are shown in Fig. 41 and Fig. 42. It turned out that the data set can be divided into two categories:

- Run group 1 (RG1)[6]: only SM4[7] is affected. Events are rejected if they contain more than 100 towers in SM4 with energy deposition above 0.1 GeV.
- Run group 2 (RG2)[8]: both SM3 and SM4 are affected. Events are rejected if they contain more than 100 towers in SM4, or more than 20 (34) towers in SM3 for MB (EMCal-triggered) events with energy deposition above 0.1 GeV.

The vertical dashed lines in the figures indicate the rejection cuts.

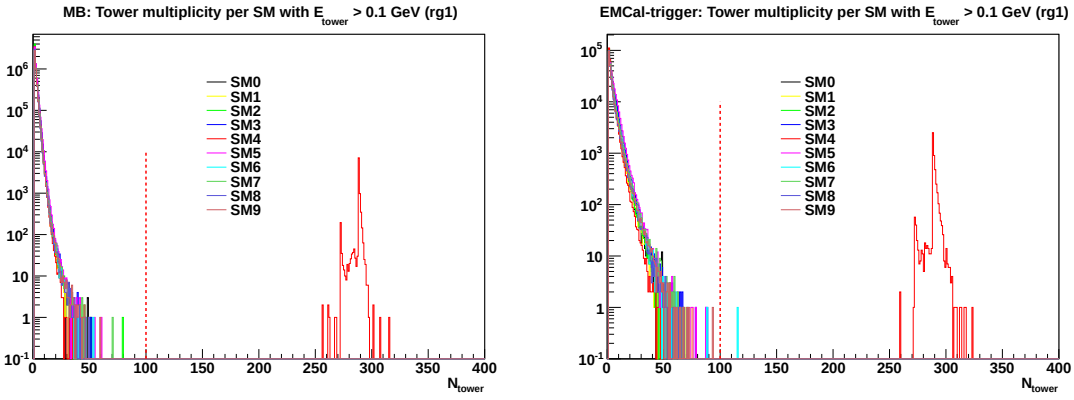

Figure 41: Number of towers with energy deposition more than 0.1 GeV in each SM for MB (left) and EMCal-triggered (right) data from RG1. Vertical dashed lines show rejection threshold.

Events with multiple, reconstructed vertices are tagged as pile-up events, and removed from analysis. For the remaining good events, the reconstructed primary vertex is required to be within 10 cm of the nominal IP along the beam axis.

6.2 Charged track selection

The charged constituents of the jets are measured in the ALICE central tracking system (TPC + ITS) as tracks. The Kalman filtering approach [93], as a local track-finding method,

[6]Run list: 146746, 146747, 146748, 146801, 146802, 146803, 146804, 146805, 146806, 146807, 146817, 146824, 146856.

[7]See Fig. 39 for naming convention.

[8]Run list: 146858, 146859, 146860.

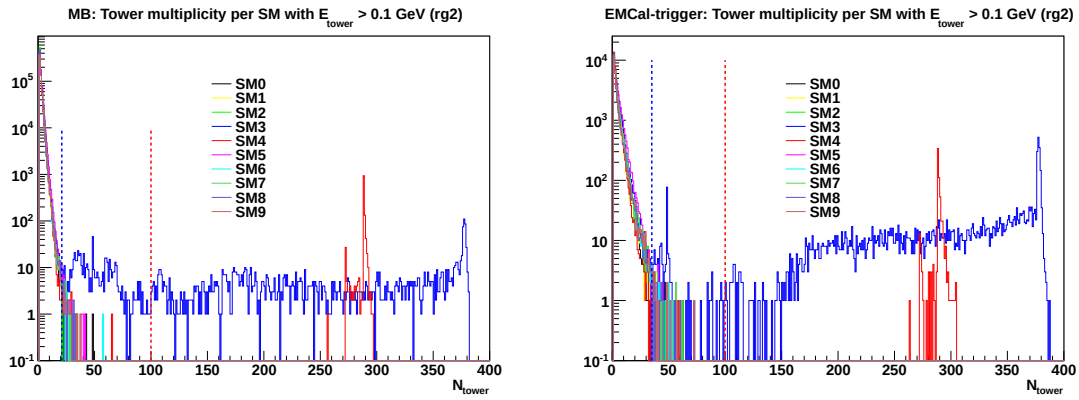

Figure 42: Number of towers with energy deposition more than 0.1 GeV in each SM for MB (left) and EMCal-triggered (right) data from RG2. Vertical dashed lines show rejection threshold.

is chosen for the track reconstruction, for its ability to handle all the local peculiarities, e.g. energy losses, multiple scatterings, dead detector regions, etc. The track reconstruction is done in three passes [94]. In the first pass, the track candidates ("seeds") at the outer radius of the TPC are found, where the track density is minimal. Then tracking proceeds inwards in the TPC, and new TPC hits are assigned to the track candidates using the Kalman filter method whenever possible. The track parameters are gradually refined as more TPC hits are assigned. When all the seeds are extrapolated to the inner wall of the TPC, the tracking in the ITS takes over, which extends the TPC tracks to the primary vertex as close as possible. Meanwhile, the ITS hits are associated to the track candidates, which further improves the estimation of the track parameters. In the second pass, tracking starts from the primary vertex, projects back to the outer radius of the ITS, and extends all the way to the outer wall of the TPC. At this stage, the track parameters are precise enough that they can be extrapolated to the outer detectors for further usage. In the final pass, all the tracks are refitted with the Kalman filter backwards to the primary vertex, and all the track parameters are finalized.

In order to achieve high and azimuthally uniform tracking efficiency required for jet reconstruction, charged track selection utilizes a hybrid approach that compensates for local inefficiencies in the ITS. Two distinct track classes are accepted in the hybrid approach: (i) global tracks containing at least three hits in the ITS, including at least one hit in the SPD,

with momentum determined without the primary vertex constraint, and (ii) complementary tracks containing less than three hits in the ITS or no hit in the SPD, with the primary vertex included in the momentum determination. Class (i) contains 90%, and class (ii) 10%, of all accepted tracks, independent of p_{T}. Track candidates have Distance of Closest Approach (DCA) to the primary vertex less than 2.4 cm in the plane transverse to the beam, and less than 3.0 cm in the beam direction. Accepted tracks have measured $p_{\mathrm{T}} > 0.15$ GeV/c, with a p_{T}-dependent minimum number of TPC hits ranging from 70 at $p_{\mathrm{T}} = 0.15$ GeV/c to 100 for $p_{\mathrm{T}} > 20$ GeV/c.

The DCA of the charged tracks to the primary vertex in the transverse plane (DCA_{xy}) is sensitive to the quality of the reconstructed tracks, especially at high p_{T}. The true high p_{T} tracks are dominated by tracks that originate from the primary vertex and whose redirection by multiple scatterings is small, and which therefore have small DCA_{xy}. Figure 43 shows the DCA_{xy} distribution of the global tracks as a function of p_{T}. At high p_{T}, the DCA_{xy} distribution is peaked at 0 with a very narrow width. Complementary tracks are

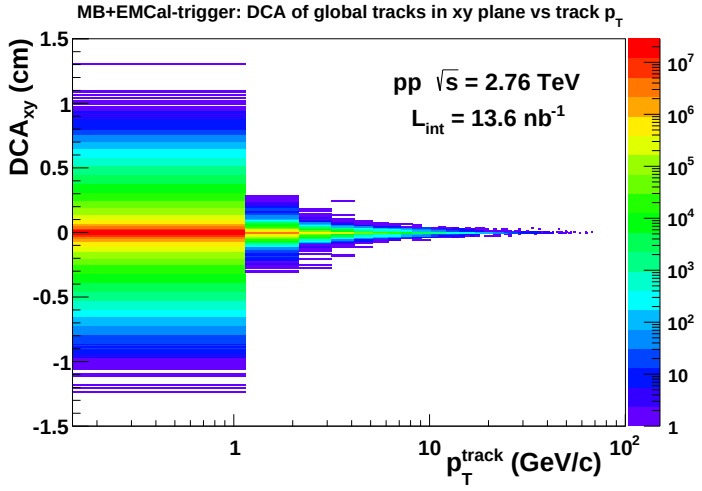

Figure 43: DCA_{xy} distribution as a function of track p_{T} for global tracks. It peaks at 0 with small width for high p_{T} tracks. The MB and EMCal-triggered data sets are combined.

constrained to the primary vertex, so their DCA_{xy} distribution must by construction be sharply peaked at 0. Since the background in this distribution is negligible for global tracks, a p_{T}-independent DCA_{xy} cut was applied.

The p_{T} distributions of the hybrid tracks are shown in Fig. 44, for MB and EMCal-

triggered data sets. The left panel is for the tracks in the TPC acceptance, while that on the right shows only tracks in the EMCal acceptance. The EMCal trigger is seen to bias towards events with a harder p_{T} spectrum, thus extending greatly kinematic reach.

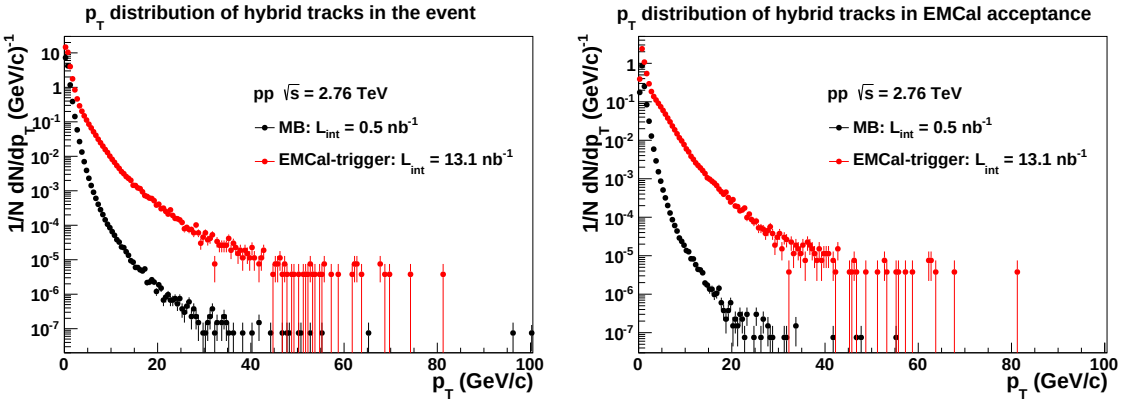

Figure 44: p_{T} distributions of hybrid tracks in the TPC (left) and EMCal (right) acceptances for MB (black) and EMCal-triggered (red) data sets.

The φ distributions of two track classes are shown in Fig. 45, 46, for $p_{\mathrm{T}} > 0.15$ GeV/c and $10 < p_{\mathrm{T}} < 20$ GeV/c respectively. For the MB data sample, the combination of global and complementary tracks results in a uniform distribution in φ. For the EMCal-triggered data set, the φ distribution is significantly biased towards the EMCal acceptance ($80^\circ < \varphi < 180^\circ$), together with an enhancement in the opposite azimuthal direction due to the di-jet production. The regions of reduced rate for global tracks correspond to dead zones in the SPD, which by design is compensated for by complementary tracks.

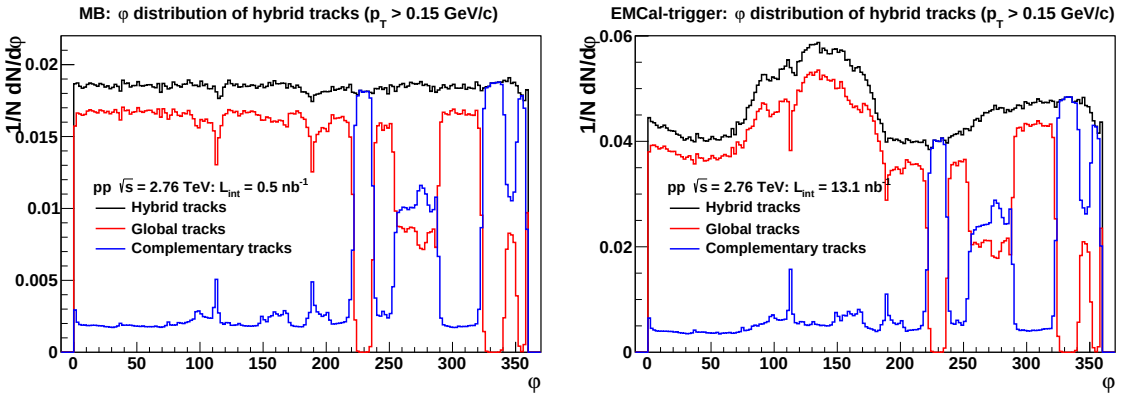

Figure 45: φ distributions of tracks with $p_{\mathrm{T}} > 0.15$ GeV/c in MB (left) and EMCal-triggered (right) data sets. The hybrid track population, which is the sum of the global and complementary distributions, is seen to be uniform in MB events.

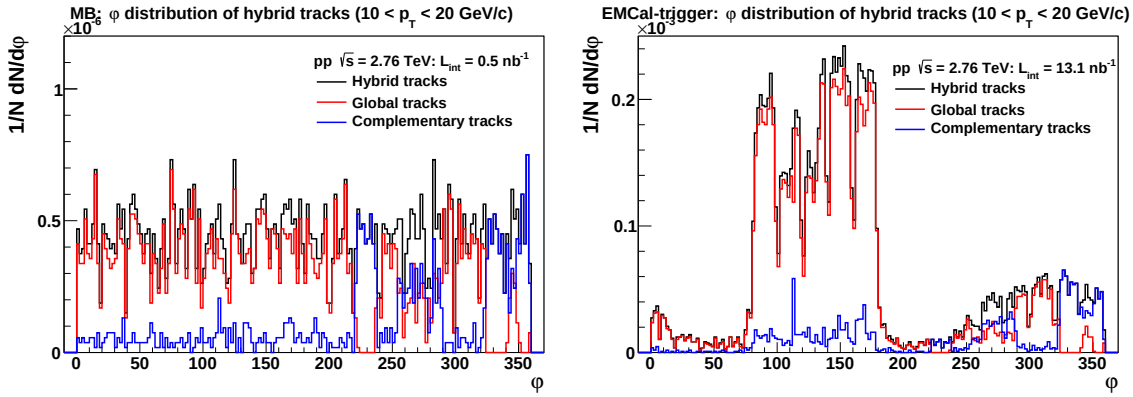

Figure 46: φ distributions of hybrid tracks with $10 < p_{\mathrm{T}} < 20$ GeV/c in MB (left) and EMCal-triggered (right) data sets. Di-jet production is observed in the triggered events.

Figure 47 shows the η distributions of the hybrid tracks from the MB and EMCal-triggered data samples in two representative p_{T} intervals: $p_{\mathrm{T}} > 0.15$ GeV/c and $10 < p_{\mathrm{T}} < 20$ GeV/c. For the MB data, the distribution is highly uniform over the region where the TPC is fully efficient, namely $|\eta| < 0.9$. For the EMCal-triggered data, an enhancement is observed in the EMCal acceptance $|\eta| < 0.7$. The non-uniformity at $\eta \sim 0$ is due to the inefficiency caused by the central membrane of the TPC.

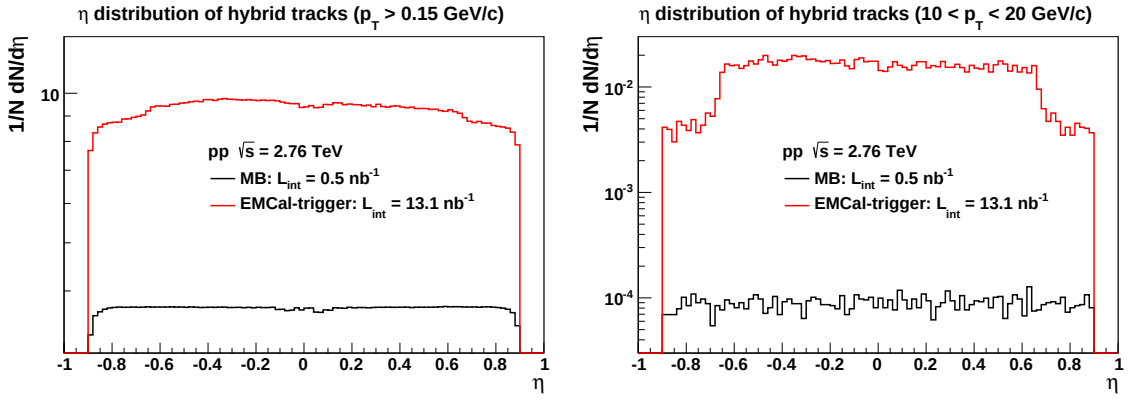

Figure 47: η distributions of hybrid tracks in MB (black) and EMCal-triggered (red) data sets in two p_{T} intervals: $p_{\mathrm{T}} > 0.15$ GeV/c (left) and $10 < p_{\mathrm{T}} < 20$ GeV/c (right).

The tracking system does not measure all the charged particles produced in the acceptance, therefore the energy carried by the missing tracks needs to be accounted for. As shown in the right panel of Fig. 44, very few tracks are above 40 GeV/c, which sets the upper limit for which quantification of the tracking performance is needed. Simulations

based on the PYTHIA [95] (Perugia-2010 tune, version 6.425) Monte Carlo (MC) event generator and GEANT [96] for particle transport and detector response are used to estimate the tracking efficiency. Figure 48 shows the estimated tracking efficiency, where three

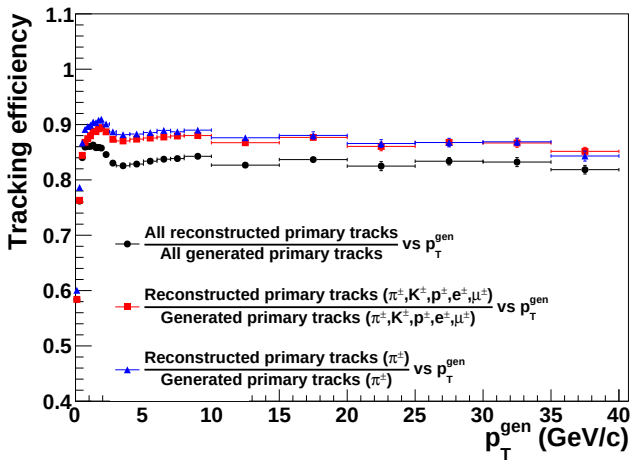

Figure 48: Three definitions of tracking efficiency for primary charged particles, from a detector-level simulation of PYTHIA pp events.

definitions of tracking efficiency are explored using primary charged particles[9] within the TPC acceptance:

- Blue points: fraction of all the primary $\pi^{\pm}$ at the particle level[10] that are matched to the accepted tracks at the detector level,[11] as a function of the particle-level track p_{T}.
- Red points: fraction of the selected primary charged particles ($\pi^{\pm}, K^{\pm}, p^{\pm}, e^{\pm}, \mu^{\pm}$) at the particle level that are matched to the accepted tracks at the detector level, as a function of the particle-level track p_{T}. Sizable differences show up at low p_{T} compared to the blue points.
- Black points: fraction of all primary charged particles at the particle level that are matched to the accepted tracks at the detector level, as a function of the particle-level

[9] ALICE definition of primary particles: particles that are produced in the collision including products of strong and electromagnetic decay and excluding feed-down from weak decays of strange particles.

[10] Information extracted directly from the PYTHIA generated events. It is also referred to as the generator level.

[11] Information extracted after the generated events go through the GEANT simulation of the ALICE detector. It is also referred to as the reconstruction level.

track p_{T}. The $\sim$ 4% efficiency loss above 1 GeV/c is due to the primary charged hyperons that decay before being detected, thus lost in the tracking system.

The figure shows no significant p_{T} dependence of the efficiency at high p_{T}, up to 40 GeV/c, for all three definitions.

Another important aspect of the tracking performance is the track p_{T} resolution, which dictates how well p_{T} is measured. The covariance matrix from the Kalman filter is used to estimate the p_{T} resolution on a track-wise basis. The left panel of Fig. 49 shows the p_{T} resolution of the hybrid tracks as a function of the track p_{T} for combined MB and EMCal-triggered data sets. The band with the best resolution is from the global tracks, while the other bands corresponding to poorer resolutions are from the complementary tracks. To further quantify the resolution, the profiles of the resolution for global and complementary tracks are shown in the right panel of Fig. 49 separately. The relative p_{T} resolution $\delta p_{\mathrm{T}}/p_{\mathrm{T}}$ is $\sim$ 1% at p_{T} = 1.0 GeV/c and $\sim$ 4% at p_{T} = 40 GeV/c for global tracks, and $\sim$ 1% at p_{T} = 1.0 GeV/c and $\sim$ 7% at p_{T} = 40 GeV/c for complementary tracks.

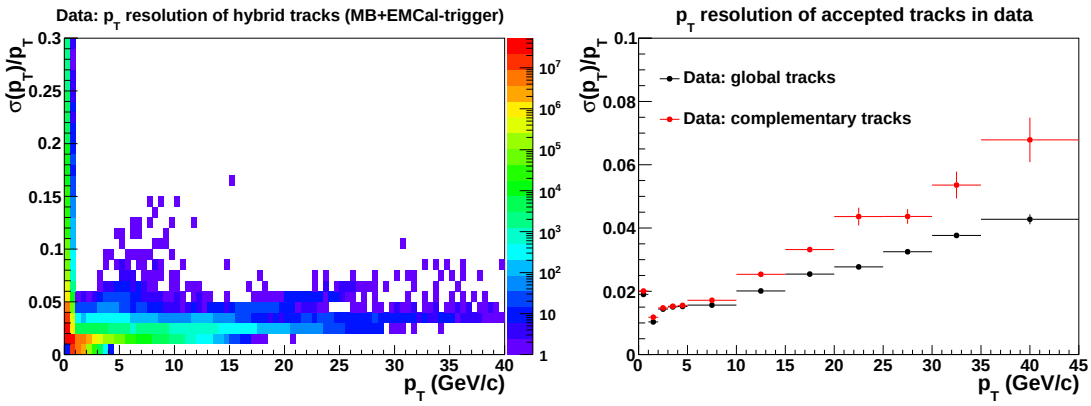

Figure 49: Left: relative p_{T} resolution as a function of track p_{T} for the hybrid tracks using combined MB and EMCal-triggered data. Right: the profiles of the relative p_{T} resolution for global and complementary tracks separately. Better resolution is seen for the global tracks.

6.3 EMCal cluster selection

Jet fragments of the neutral pions and photons are measured in the EMCal, which comprise a large fraction of the neutral constituents of the jets. The missing part of the neutral energy is mainly carried by the neutrons and $\mathrm{K}^0_{\mathrm{L}}$'s, which can only be detected in a hadronic

calorimeter. The input to the jet-finding algorithm are the EMCal clusters, which represent the full electromagnetic showers initiated by the incoming photons or electrons. A clustering algorithm that combines the signals from adjacent EMCal towers is used to form clusters, whose size is limited by the requirement that each cluster can only contain one local energy maximum. This clustering algorithm is chosen to prevent unwanted interferences between the clustering algorithm and the jet-finding algorithm, especially for small values of R.

6.3.1 Cluster reconstruction and calibration

Towers that give false signals all the time are called "hot" towers, and need to be identified and removed from the analysis. 97 known problematic towers have already been masked out online, although additional hot tower candidates may emerge in offline analysis. To identify such hot towers, the firing frequency for each tower, namely the number of times in an event sample that a tower registers energies above 0.1 GeV, is used as the discriminator, shown in Fig. 50. The distribution is fitted using a Gaussian distribution, and the outliers above

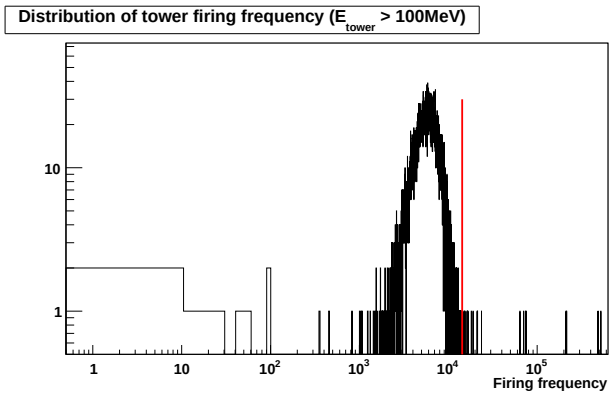

Figure 50: Distribution of the firing frequency for all the towers. The measured energy is required to be above 0.1 GeV. The vertical red line indicates a 5σ cut, used to identify the hot tower candidates.

5σ, indicated by the red vertical line in Fig. 50, are selected as the hot tower candidates. By looking at the energy distribution of each hot tower candidate individually, 24 towers are identified as hot, and excluded from the analysis.

With 121 hot towers, comprising about 1% of all EMCal towers, masked out, the clustering algorithm takes over and reconstructs the clusters as follows:

- Start from the list of good towers whose energies are above 0.05 GeV. No cut on the tower time is applied due to the very low pile-up rate and the limited time information in the simulations.

- Find the tower with the highest energy in the list as the seed, whose energy should exceed 0.1 GeV.

- Expand from the seed in all directions by absorbing the neighboring towers until the local minima are reached. Call this group of towers a cluster and remove all the towers in the cluster from the tower list.

- Repeat the procedure until no towers are left in the list. Then a list of EMCal clusters is built.

Various calibration factors are applied to correct for the measurement errors in energy and position. The positions of the clusters are calculated using the nominal coordinates of the EMCal SM's. But there could be misalignment due to various aspects, e.g. gravity, which can be extracted from in-situ survey measurements and applied to the position calculation. The energy calibration factor for each tower is determined such that the reconstructed π^0 peak in each tower is centered at the nominal value of 0.135 GeV, which fixed the relative energy response of all the towers. The energy non-linearity curve extracted from 2010 electron beam test data is used to account for the non-uniform energy response of the EMCal, shown in Fig. 51.

Following the above energy corrections, the absolute EMCal energy scale needs to be fixed via comparisons between data and simulation. The left panel of Fig. 52 shows the mean of the ratio between the cluster energy and the matched track momentum (E/p) for electron candidates in data (black) and simulation (red). The right panel of the figure shows the reconstructed mass peak position for π^0, using the invariant mass of EMCal cluster pairs in data (black) and simulation (red). Both comparisons give $\sim 2\%$ discrepancy, which motivates scaling up the cluster energy by 2% in data.

In the end, only clusters with energy above 0.3 GeV are used for the jet finding, due to the large uncertainty associated with the large non-linearity corrections (see Fig. 51).

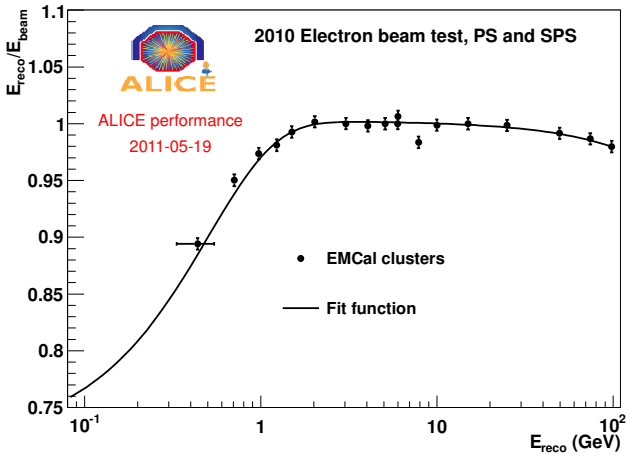

Figure 51: Non-linearity of the EMCal energy response obtained from 2010 electron test beam measurements. The black curve is a fit to the data points with the form: $f(x) = p_0 \times \frac{1}{1+p_1 e^{-x/p_2}} \times \frac{1}{1+p_3 e^{(x-p_4)/p_5}}$.

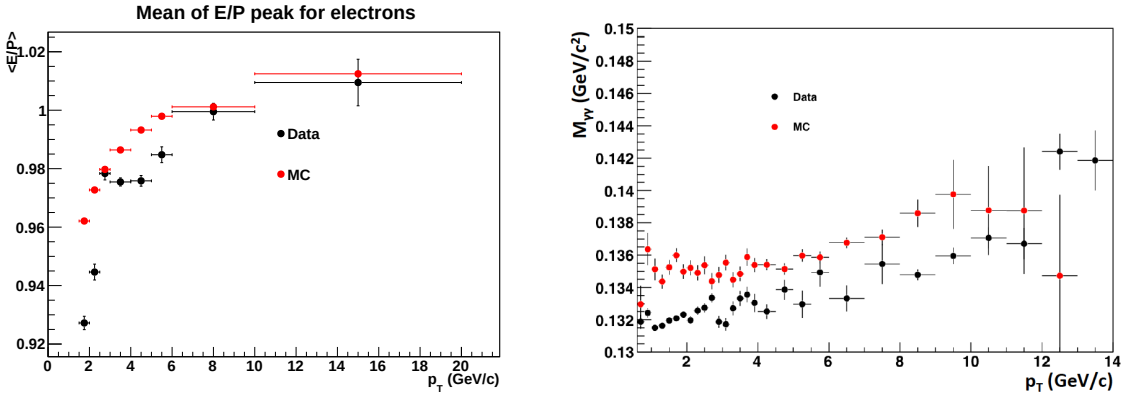

Figure 52: Left: Mean of the ratio of cluster energy and matched track momentum for electron candidates as a function of the matched track p_{T}. Right: π^0 mass positions via invariant mass method using EMCal cluster pairs as a function of π^0 p_{T}. Data are shown in black, and simulation is shown in red.

6.3.2 Exotic clusters

Clusters with large apparent energy but anomalously small number of contributing towers are attributed to the interactions of slow neutrons or highly ionizing particles in the avalanche photodiode (APD) of the corresponding towers. These "exotic" clusters have to be removed from the analysis since they are not part of the jet energy. Accurate simulation of such processes is not possible currently, so a data-driven method is developed to identify and remove them. The rejection criterion to define such exotic clusters is based on the value of the quantity for each cluster:

$$F_{\text{cross}} = 1 - \frac{E_{\text{cross}}}{E_{\text{seed}}} \tag{50}$$

where E_{seed} is the energy of the most energetic tower in a cluster and E_{cross} is the summed energy of the towers in the cluster that share an edge with the seed. Figure 53 shows the distributions of F_{cross} as a function of the cluster energy. It can be seen that a large fraction of the energetic clusters have a value of F_{cross} close to unity, i.e. the seed towers carry most of their energies.

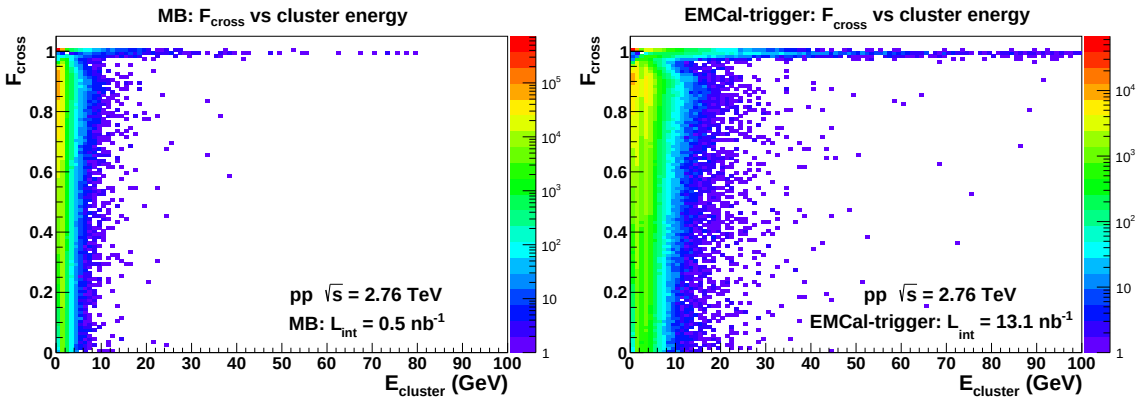

Figure 53: Distribution of F_{cross} as a function of cluster energy in MB (left) and EMCal-triggered (right) data sets.

To determine the cut value for the exclusion of the exotic clusters, the projected distribution of F_{cross} is shown in the left panel of Fig. 54. The blue vertical line, at the border of the discontinuity, indicates the rejection cut, with accepted clusters having $F_{\text{cross}} < 0.97$. Figure 54, right panel, shows the rejection rate, which increases with increasing cluster

energy. For clusters with $E > 30$ GeV, more than 80% of them are rejected as background by this cut. This is a large rejection factor, and its systematics will be discussed in section 6.4.1.

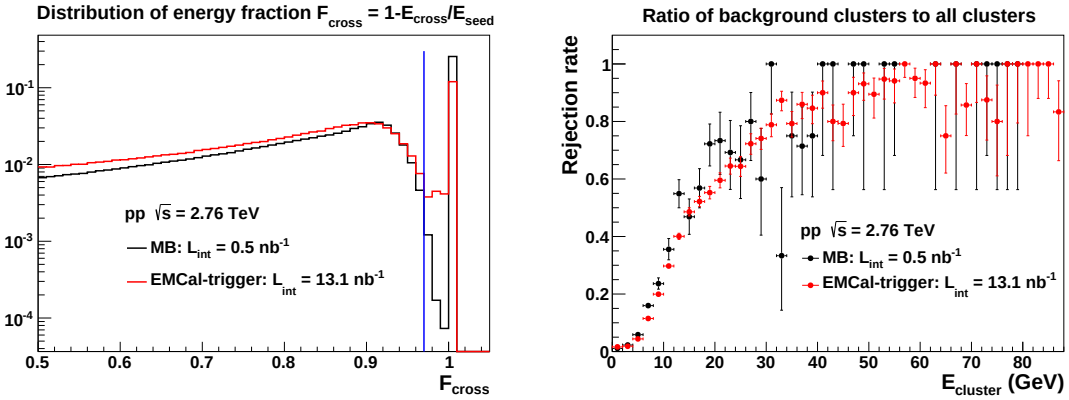

Figure 54: Left: distribution of F_{cross} for both MB and EMCal-triggered events. Right: EMCal cluster rejection rate as a function of the cluster energy, based on $F_{\text{cross}} < 0.97$ for accepted clusters.

6.3.3 Hadronic correction

Besides the neutral pions and photons, charged hadrons also deposit energy in the EMCal, mostly via minimum ionization but also via nuclear interactions generating partially-contained hadronic showers, while electrons induce full electromagnetic showers in the EMCal. However, charged hadrons and electrons are already measured in the tracking system with much better resolution, so corrections to the EMCal clusters, which are initiated by charged particles, must be applied to avoid double-counting of a fraction of their energy in the measured jet energy.

The correction procedure, which is similar in nature to "Particle Flow" algorithms for jet reconstruction [97], minimizes dependence on the simulation of hadronic and electromagnetic showers. Charged-track trajectories are propagated to the cluster positions in steps of 20 cm and corrected for the energy loss, assuming the pion mass, in the intervening material. Figure 55 shows the residual distributions for the closest track-cluster pairs, whose widths are fitted to be ~ 0.014 in $\Delta\varphi$ and ~ 0.007 in $\Delta\eta$. The double-peaked structure in the $\Delta\varphi$ distribution in the MB data set is due to the opposite bending direction of positive

and negative charged particles in the magnetic field, which gives displacement at the EMCal for low p_{T} tracks. Each charged track is matched to the closest EMCal cluster after propagation if their residuals are within $|\Delta\varphi| < 0.03$ and $|\Delta\eta| < 0.015$. This is illustrated by the blue vertical lines in Fig. 55. Multiple charged tracks can be matched to a single cluster, though the probability for this is less than 0.2%.

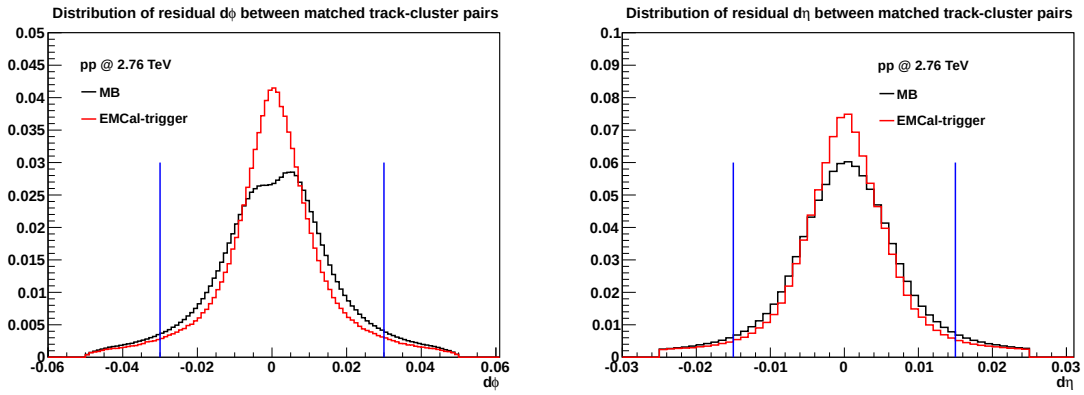

Figure 55: Residual distributions of the closest track-cluster pairs in $\Delta\varphi$ (left) and $\Delta\eta$ (right) after propagation of track trajectories. The vertical blue lines indicate the matching cuts.

Correction of cluster energy for charged energy double counting is based on the following quantity, which is calculated for each cluster having matched tracks:

$$E_{\mathrm{corr}} = E_{\mathrm{clust}} - f_{\mathrm{sub}} * \sum \mathrm{p} \tag{51}$$

where E_{clust} is the measured cluster energy and $\sum \mathrm{p}$ is the sum of the 3-momentum magnitude for all tracks matched to the cluster. Test beam measurements of single charged particle interactions in the EMCal show that the probability for the EMCal shower energy to exceed the particle momentum is negligible [77]. Therefore, $f_{\mathrm{sub}} = 1$ ("100% correction") is used for the nominal analysis, with smaller values of f_{sub} used to establish the systematic uncertainty due to this choice. If $E_{\mathrm{corr}} < 0$, the cluster is discarded, otherwise it is assigned energy E_{corr}. If a cluster is generated entirely by the measured charged tracks, the charged track energy is removed accurately from the EMCal clusters without any assumption about the shape of hadronic showers in the EMCal. However, if a cluster has additional contributions from neutral particles or unmeasured charged particles (i.e. "cluster pileup"),

over-subtraction of the charged energy deposition will occur, even though the rate is on the level of 1%.

The correction to the cluster energy, $\Delta E_{\rm corr} = E_{\rm clust} - E_{\rm corr}$, takes the following values:

$$\Delta E_{\rm corr} = \begin{cases} E_{\rm clust} \quad \text{for} \quad E_{\rm clust} < f_{\rm sub} * \sum \mathrm{p} \\ \\ f_{\rm sub} * \sum \mathrm{p} \quad \text{for} \quad E_{\rm clust} > f_{\rm sub} * \sum \mathrm{p} \end{cases} \tag{52}$$

To study the distribution of $\Delta E_{\rm corr}$, the following ratio, which is calculated on a cluster-by-cluster basis, is chosen:

$$R_{\rm corr} = \frac{\Delta E_{\rm corr}}{\sum \mathrm{p}}. \tag{53}$$

Figure 56 shows the normalized probability distribution of $R_{\rm corr}$, in four different bins of summed matched tracks $p_{\rm T}$ for the MB data sample, EMCal-triggered data sample, and simulation. For a cluster whose energy arises solely from the matched tracks, i.e. which does

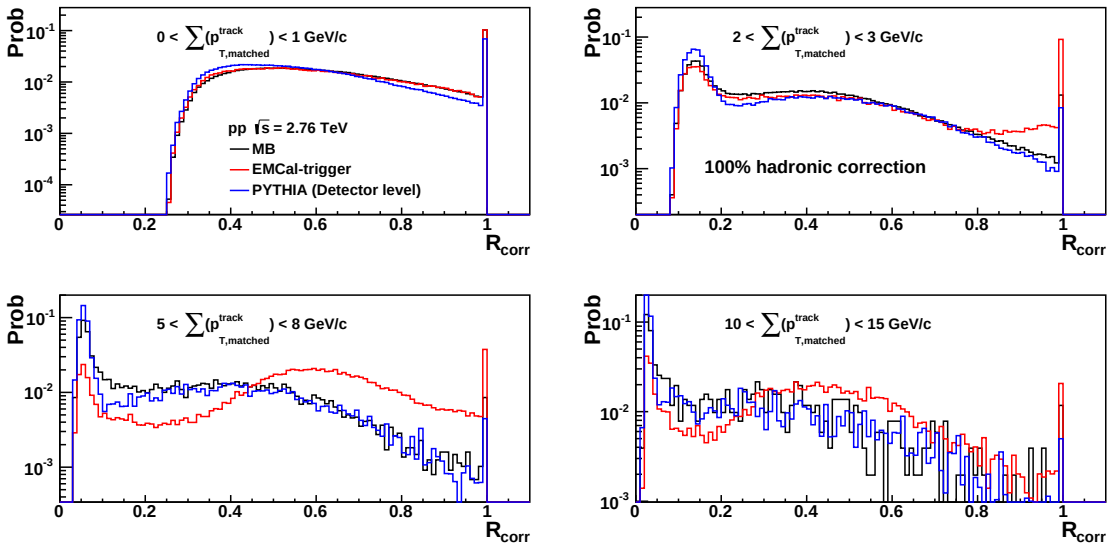

Figure 56: Probability distribution of $R_{\rm corr}$ (Eq. 53), in four different bins of summed matched track $p_{\rm T}$.

not contain "pileup" energy from photons or untracked charged particles, the distribution of $R_{\rm corr}$ is the in-situ measurement of E/p for the EMCal (in the range $E/p < 1$)[12]. The

[12]While the EMCal is a limited-resolution hadronic calorimeter and full containment of a hadronic shower is unlikely, we note that there is no physical reason to limit the choice of $f_{\rm sub}$ to $f_{\rm sub} < 1$, since the calorimeter response can fluctuate upward. The full distribution of E/p should be measured with a value of $f_{\rm sub}$ larger

peak at unity corresponds to 100% of the matched track momenta being subtracted from the cluster energy. The distribution below unity for the MB trigger is modeled quite well by the simulation. The variation in the distribution for the EMCal-triggered data is due to the trigger bias: the EMCal trigger at threshold favors low p_{T} (i.e. high rate) charged hadrons that deposit more energy in the EMCal than average.

The magnitude of the over-subtraction can be estimated in simulation, in which the particles that contribute to an EMCal cluster are known precisely. The variable used to quantify the over-subtraction is the difference of the subtracted energy following the correction scheme described above and the actual energy that should be subtracted based on the MC information. It is defined as:

$$\Delta E_{\mathrm{T}} = \Delta E_{\mathrm{T}}^{\mathrm{corr}} - E_{\mathrm{T,sub}}^{\mathrm{MC}} \tag{54}$$

where

$$E_{\mathrm{T,sub}}^{\mathrm{MC}} = E_{\mathrm{T}}^{\mathrm{clust}} - E_{\mathrm{T,reconstructed}}^{\mathrm{neutral}} \tag{55}$$

$E_{\mathrm{T,reconstructed}}^{\mathrm{neutral}}$ is the part of the cluster energy contributed by the neutral particles. The transverse energy is used here, which is very close to the full energy since the EMCal is located at mid-rapidity. The left panel of Fig. 57 shows the mean relative over-subtracted energy as a function of jet p_{T} ($R = 0.4$) at detector level. The MIP correction[13] and $f_{\mathrm{sub}} = 0.3$ are seen to substantially under-subtract the charged energy in the EMCal, while any choice between $f_{\mathrm{sub}} = 0.5$ and $f_{\mathrm{sub}} = 1$ correctly subtracts the charged energy within 3%. The right panel of Fig. 57 shows the RMS of the $\Delta E_{\mathrm{T}}/p_{\mathrm{T,jet}}$ distribution, which is the contribution to the jet energy resolution (JER) by the hadronic correction. Above 40 GeV/c, all choices between $f_{\mathrm{sub}} = 0.5$ and $f_{\mathrm{sub}} = 1$ give similar resolution. However, in the low p_{T} region, $f_{\mathrm{sub}} > 0.7$ is seen to minimize the resolution effects. The residual over-subtraction is corrected via simulation, as described in Section 8.2.4

than unity.

[13] In this correction scheme, the MIP energy (0.27 GeV) is subtracted from the cluster energy for each matched track.

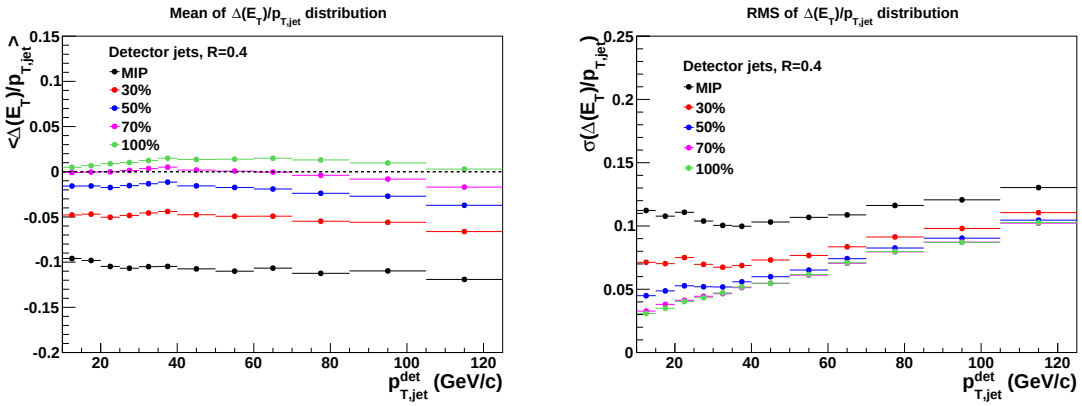

Figure 57: Left: mean relative over-subtracted energy as a function of jet p_{T} ($R = 0.4$) using detector-level simulation. Right: smearing effects on jet energy introduced by the hadronic correction.

6.3.4 Detailed features of EMCal clusters

The energy distribution of EMCal clusters for both MB and EMCal-triggered data sets are shown in Fig. 58. The peak at ~ 4 GeV in the triggered data set is due to the EMCal SSh trigger, which greatly extends the kinematic reach of the clusters, thus jets.

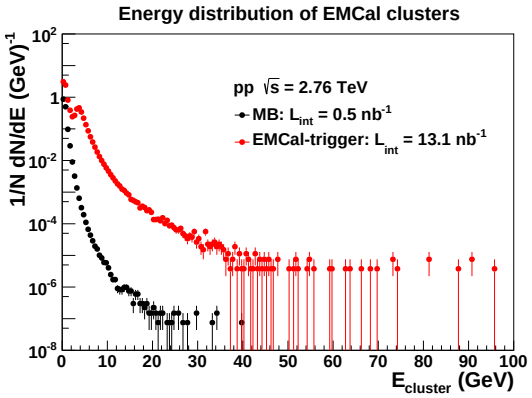

Figure 58: Energy distribution of EMCal clusters in MB (black) and EMCal-triggered (red) data sets.

Figure 59 shows the distributions of the number of towers per cluster as a function of the cluster energy in MB (left) and EMCal-triggered (right) data sets. More towers are contained in the clusters with larger energy.

The spatial distributions of EMCal clusters are shown in Fig. 60 and Fig. 61, for clusters with $E > 0.3$ GeV and $E > 5$ GeV respectively. The dead regions in SM0 ($\eta \sim 0.45, \varphi \sim 95°$) and SM5 ($\eta \sim -0.6, \varphi \sim 135°$) are excluded during the reconstruction. The readout

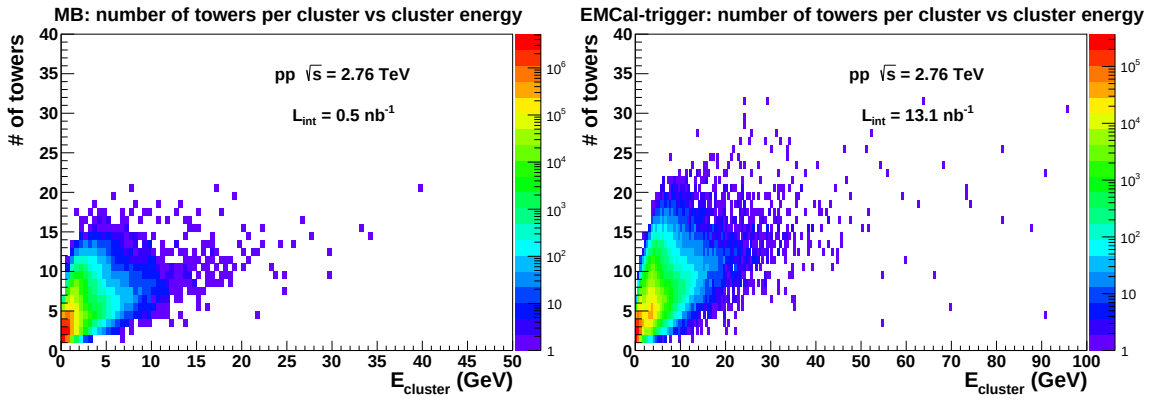

Figure 59: Distributions of the number of towers per EMCal cluster as a function of the cluster energy for MB (left) and EMCal-triggered (right) data sets.

region in SM4 ($\eta > 0, 120^\circ < \varphi < 126.7^\circ$) is excluded offline since it was reading signals from the wrong events. The regions of lower cluster density seen in Fig. 61, right panel, are due to the exclusion of the TRUs (see discussion in section 6.1). Since the EMCal readout was live for these regions, there is still a finite density of clusters with $E > 5$ GeV.

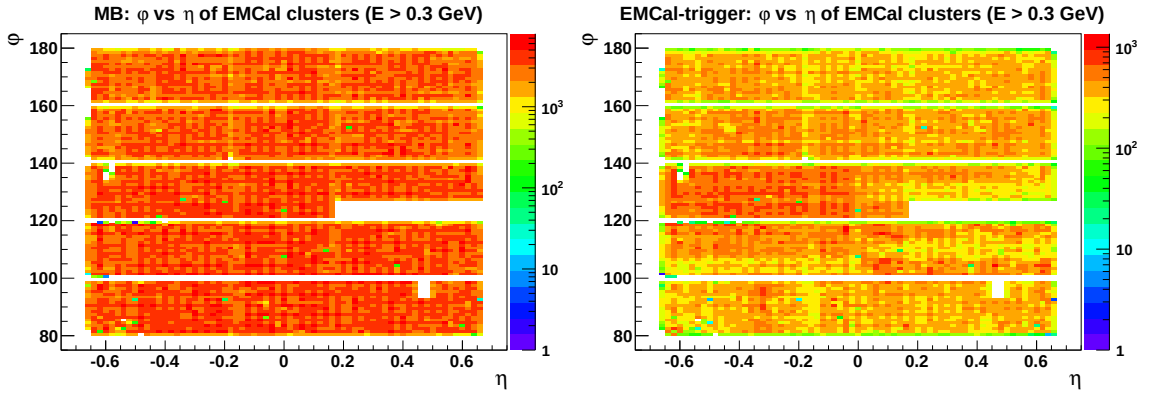

Figure 60: Spatial distribution of all accepted EMCal clusters in MB (left) and EMCal-triggered (right) data sets.

6.4 Jet reconstruction

Accepted charged tracks and EMCal clusters are fed into the FastJet anti-k_{T} jet-finding algorithm, with two resolution parameters $R = 0.2$ and 0.4 used. The BIpt-scheme is used which incorporates a weighted recombination of η and φ, and scalar summing of p_{T} (section 3.3). The jet acceptance, determined by the EMCal, is defined by a fiducial cut based on

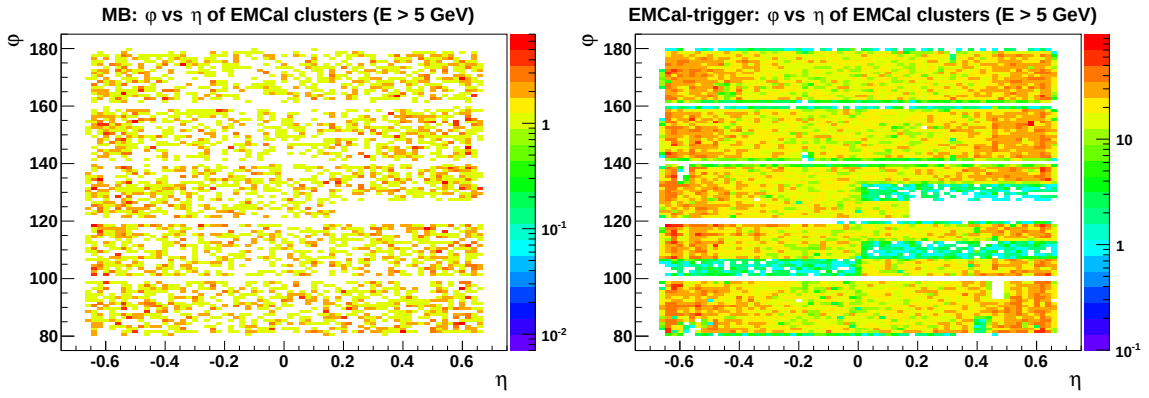

Figure 61: Spatial distribution of accepted EMCal clusters with $E > 5$ GeV in MB (left) and EMCal-triggered (right) data sets.

the position of the jet centroid:

$$|\eta_{jet}| < 0.7 - R, \ 1.4 + R < \varphi_{jet} < 3.14 - R, \tag{56}$$

Only jets with $p_{\mathrm{T,jet}} > 20$ GeV/c are considered in the cross section measurement, even though lower p_{T} jets are used in some diagnostic studies.

6.4.1 z_{leading} cut

The charged-particle tracking algorithm may misidentify low p_{T} decay daughters from secondary vertices as primary vertex tracks, and assign them a much larger p_{T} value. In addition, background in the EMCal can generate false neutral clusters with large apparent p_{T}, as described in section 6.3.2. The cuts imposed at the track or cluster level to suppress such cases directly may not be fully efficient, leading to fake jets with large apparent $p_{\mathrm{T,jet}}$. However, such false high p_{T} tracks or clusters will have little additional hadronic activity in their vicinity, if they are not part of an energetic jet. These cases are identified by examining the distribution of the longitudinal momentum fraction z of a jet carried by a hadron in the jet:

$$z = \frac{p_{\mathrm{h,proj}}}{p_{\mathrm{jet}}} = \frac{\vec{p_{\mathrm{h}}} \cdot \vec{p_{\mathrm{jet}}}}{|\vec{p_{\mathrm{jet}}}|^2} \tag{57}$$

i.e. the magnitude of the projection of the hadron 3-momentum on the jet axis. The distributions of z in three uncorrected $p_{\mathrm{T,jet}}$ bins are shown in Fig. 62, for both MB and

EMCal-triggered data sets. The EMCal trigger is seen to induce a bias in the z distribution for jets with low p_{T} (left panel), but not at significantly higher p_{T}. From the standpoint

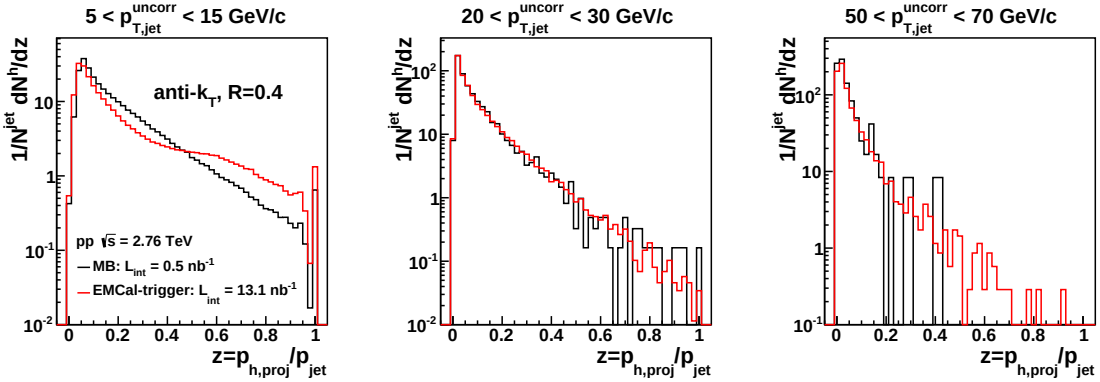

Figure 62: z distribution in three uncorrected $p_{\mathrm{T,jet}}$ bins ($R = 0.4$) for MB (black line) and EMCal-triggered (red line) data sets.

of QCD, hadrons with $z \sim 1$, corresponding to jets in which a single hadron carries almost all the jet energy, are improbable, and the distribution of z is expected to be continuous. However, the distributions in Fig. 62 show an apparently discontinuous peak close to $z = 1$, most significantly for low p_{T} jets. Jets are therefore required to have $z_{\mathrm{leading}} < 0.98$ independent of jet p_{T}, where z_{leading} is the z of the leading constituent in the jet. Figure 63 shows the effect of the z_{leading} cut on the raw jet yield ($R = 0.4$) in MB and EMCal-triggered data sets, which is seen to be negligible for $p_{\mathrm{T,jet}} > 10$ GeV/c.

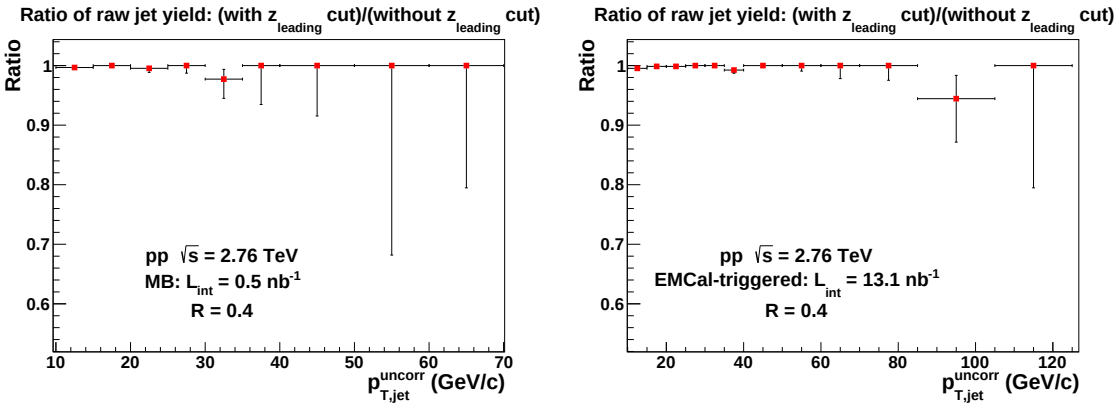

Figure 63: Ratio of the raw jet yield with $z_{\mathrm{leading}} < 0.98$ cut over the raw yield without z_{leading} cut in MB (left) and EMCal-triggered (right) data sets.

As discussed in section 6.3.2, a cut on F_{cross} is applied to reject exotic EMCal clusters

with large measured energy but anomalously small number of towers. In addition, a cut on z_{leading} is applied to remove unphysical jets that are dominated by a single track or cluster, due probably to mismeasurement or noise. Given that F_{cross} and z_{leading} cuts deal with similar issues, a correlation between them is expected. This correlation is studied in Fig. 64, where the distributions of F_{cross} for EMCal clusters that are the leading (largest z) constituents of jets ($R = 0.4$) are shown. Jets with $z_{\text{leading}} < 0.98$ and $z_{\text{leading}} > 0.98$ are separated and several $p_{\text{T,jet}}^{\text{uncorr}}$ intervals are selected. A clear peak at $F_{\text{cross}} \sim 1$ emerges

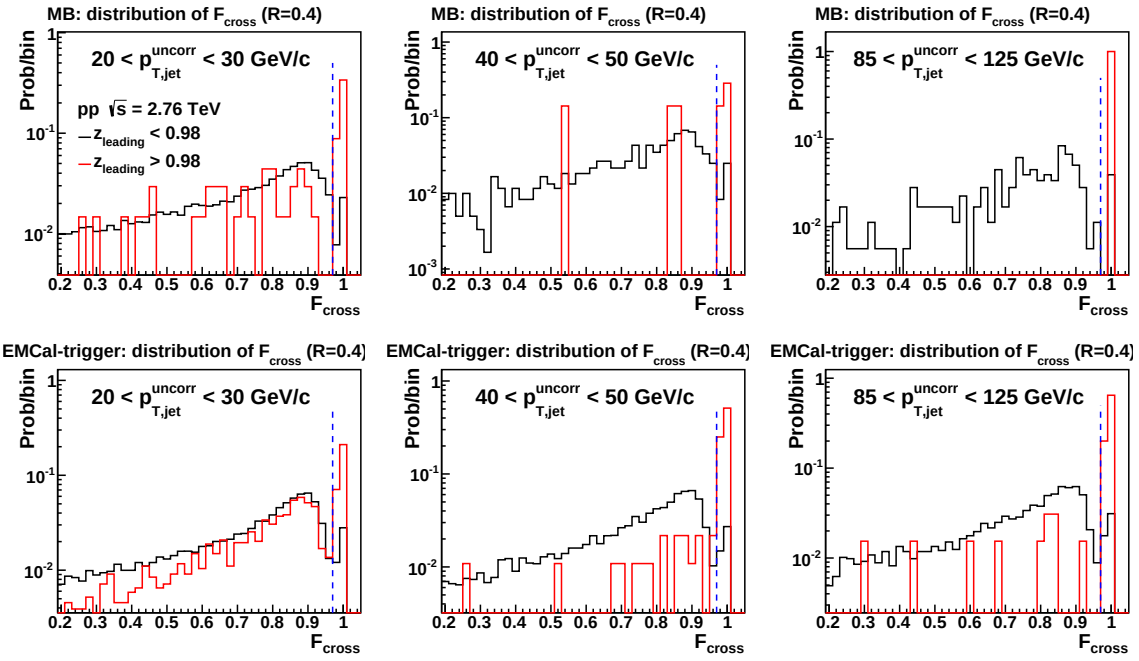

Figure 64: Distribution of F_{cross} for EMCal clusters which are the leading constituents of $R = 0.4$ jets in MB (upper row) and EMCal-triggered (lower row) data sets. Black: distribution for jets with $z_{\text{leading}} < 0.98$; Red: distribution for jets with $z_{\text{leading}} > 0.98$. Blue vertical dashed lines indicate the $F_{\text{cross}} < 0.97$ cut.

for the distribution with $z_{\text{leading}} > 0.98$, illustrating the strong correlation between these observables. The figure however also shows a peak at $F_{\text{cross}} \sim 1$ for the distribution with $z_{\text{leading}} < 0.98$, indicating that cuts on both observables are required to remove unphysical jets. In fact, almost all of the rejection is accomplished by the F_{cross} cut alone, even though this is not necessarily the case in general.

6.4.2 Uncorrected jet distributions

Figure 65 shows the raw (uncorrected) p_{T} distribution of inclusive jet yield per event, for both MB and EMCal-triggered data. The EMCal trigger is seen to greatly extend the kinematic reach of the jet population, as already indicated by the spectra of the charged tracks (Fig. 44) and EMCal clusters (Fig. 58). Meanwhile, a bias is induced by the EMCal trigger in the low $p_{\mathrm{T,jet}}^{\mathrm{uncorr}}$ region, as seen by the difference in shape of the two distributions.

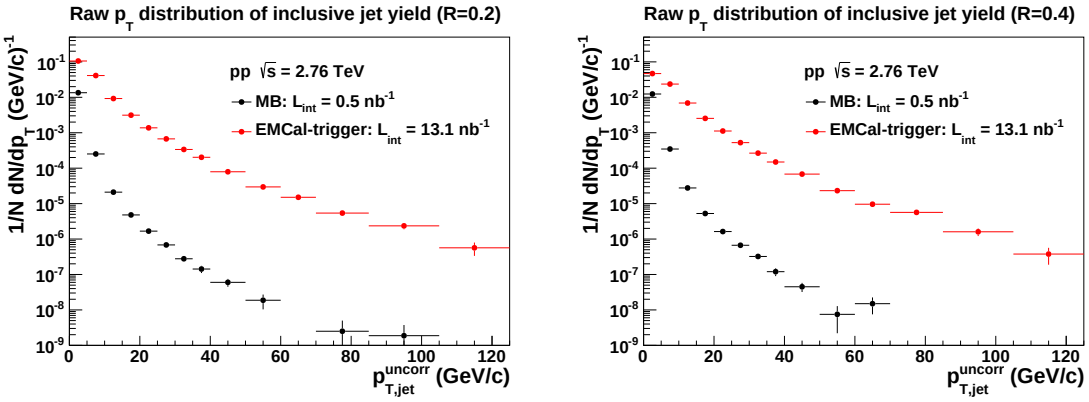

Figure 65: Raw p_{T} distribution of inclusive jet yield for $R = 0.2$ (left) $R = 0.4$ (right) jets in MB (black) and EMCal-triggered (red) data sets.

Figures 66 and 67 show the spatial distributions of reconstructed jets within the acceptance, projected onto the φ and η directions respectively, for various intervals of $p_{\mathrm{T,jet}}^{\mathrm{uncorr}}$.

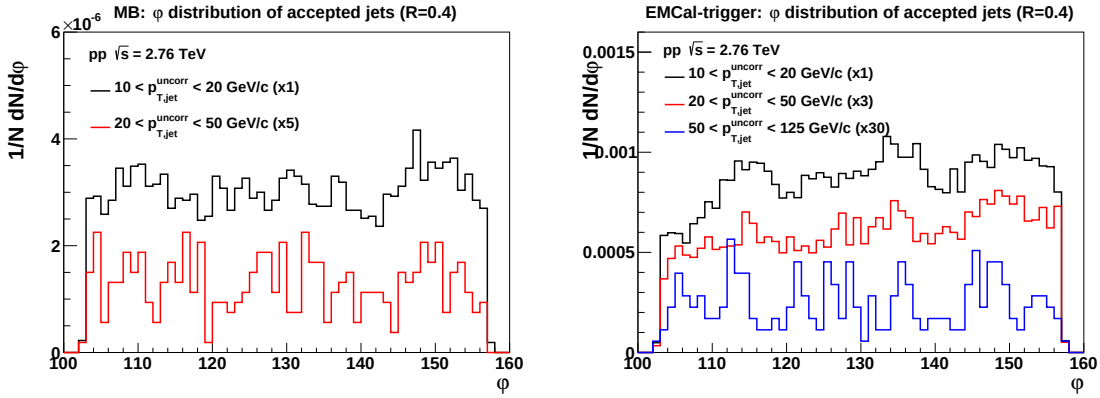

Figure 66: φ projection of spatial distribution of $R = 0.4$ jets in MB (left) and EMCal-triggered (right) data sets

Within the resolution of the analysis, the jet response appears to be consistent with uniformity over the acceptance in the MB data. For the EMCal-triggered data, there are some

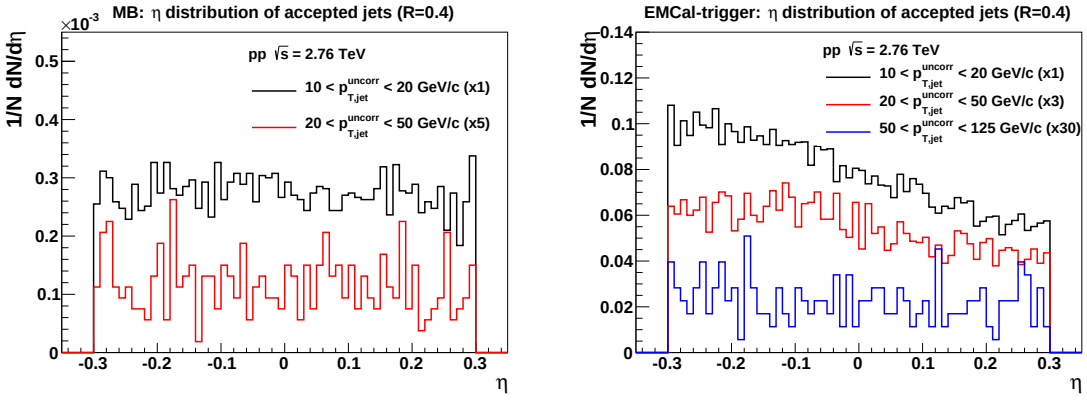

Figure 67: η projection of spatial distribution of $R = 0.4$ jets in MB (left) and EMCal-triggered (right) data sets

marked η and φ dependences (Fig. 67 and 66, right panels). These dependences can be attributed to the non-uniformity of the EMCal trigger, which is also observed in the EMCal cluster spatial distributions (Fig. 61). Measurement of the trigger bias on jets, discussed in section 7.2.1, corrects for this effect.

7 Trigger bias on jets

7.1 MB trigger

The MB trigger is intended to select all the collisions that contain hadronic interactions with minimal requirements on the details of the interactions. While jets are predominantly produced in hard scatterings, they should fire the MB trigger with full efficiency. This can be validated by comparing the particle-level jet spectra with and without MB trigger fired on detector level using MB simulation, shown in Fig. 68 for $R = 0.4$ jets. Indeed, the MB

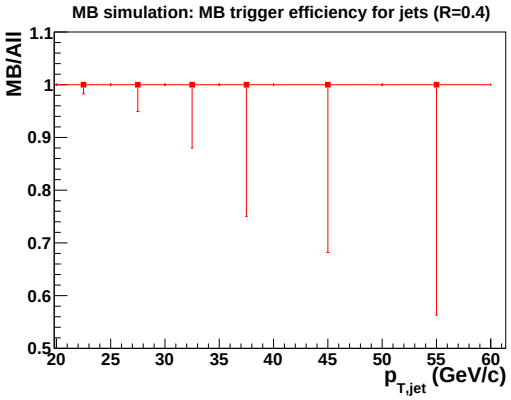

Figure 68: MB trigger efficiency for $R = 0.4$ jets estimated using MB simulations.

trigger efficiency is 100% above 20 GeV/c:

$$\epsilon_{\text{trigger}}\left(p_{\text{T}}\right) = 1 \tag{58}$$

which is also true for the $R = 0.2$ jets (not shown).

Since the MB trigger does not impose any bias on jets, the trigger acceptance is:

$$A_{\text{trigger}} = 1 \tag{59}$$

The dead regions and non-functioning electronics in the detectors that measure the trigger signals would miss some fraction of the delivered MB collisions, regardless of the presence of the jets. Therefore, it is equivalent to a loss of statistics, which does not affect the jet cross section measurement.

Primary vertices are required to be reconstructed in the MB event sample, which in principle could induce a bias on jets. Figure 69 shows the ratio of the particle-level jet spectra using simulated events with and without reconstructed primary vertices on detector level. Evidently, the efficiency of the vertex requirement for $R = 0.4$ jets is 100% above 20 GeV/c, which is also true for $R = 0.2$ jets.

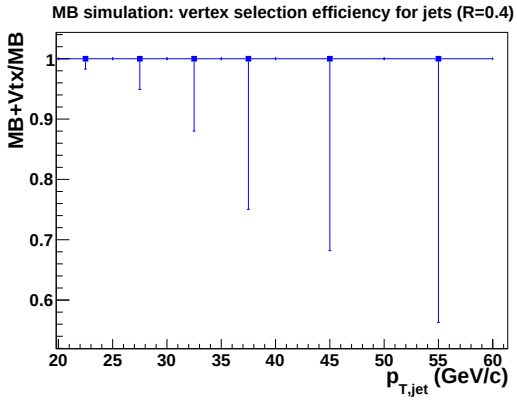

Figure 69: Vertex selection efficiency for $R = 0.4$ jets estimated using MB simulation.

7.2 EMCal SSh trigger

7.2.1 Trigger bias

Unlike the MB trigger, the EMCal SSh trigger only accepts events which contain more than 3 GeV energy deposition within a window of 4×4 towers in the EMCal. Thus, a fraction of the events that contain only low p_{T} jets in the EMCal acceptance are rejected. The rejection fraction decreases as the jet p_{T} increases, and reaches a plateau at sufficiently high $p_{\mathrm{T,jet}}$ where the trigger is expected to be fully efficient. In order to use the triggered data set for the jet cross section measurement, the bias imposed on jets needs to be assessed and corrected.

Purely data-driven method: a direct approach to extract the trigger bias is to compare the raw jet yields in the triggered and MB data sets, which are shown in Fig. 70 for $R = 0.4$ (left) and $R = 0.2$ (right) jets. As expected, the ratio rises as jet p_{T} goes up, which is in line with a decreasing bias. The correction factors for the jet production rate at high p_{T} can be extrapolated directly from the plateau. Therefore, the rightmost data

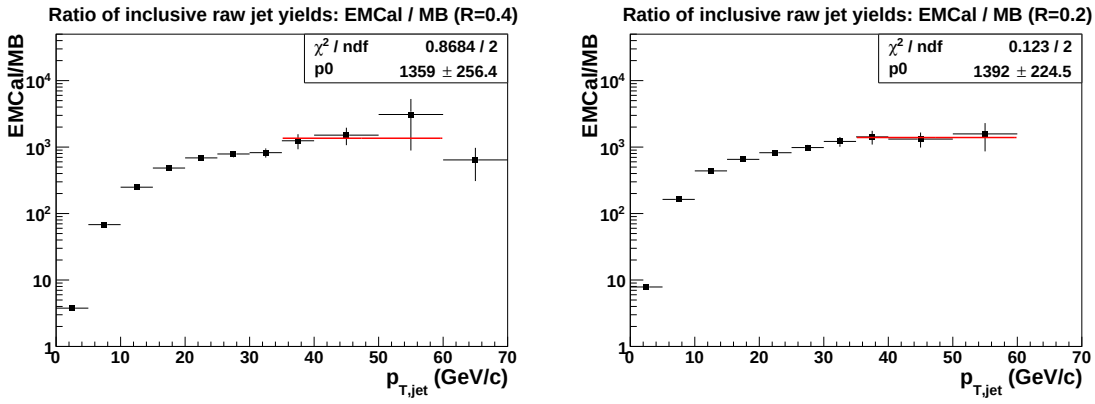

Figure 70: Ratio of raw inclusive jet yields EMCal/MB for $R = 0.4$ (left) and $R = 0.2$ (right). Red lines show the measured trigger rejection factor by fitting a constant line in the range indicated.

points are fitted with a constant line to check if the plateau is reached. However, Fig. 70 does not show strong evidence for a plateau, due to the limited MB statistics. This method is therefore not optimal for correcting the trigger bias as it comes with large uncertainties.

Data-driven + simulation method: an alternative approach to estimate the trigger bias on jets is to combine the measurement of the trigger bias on EMCal clusters from data with detector-level simulations based on PYTHIA and GEANT. This is motivated by the fact that the trigger plateau for the EMCal clusters is reached within the current statistical reach. There are two distinct sources of trigger inefficiency on jets that should be taken into account:

- Regions of the EMCal that are not read out by the DAQ (dead electronics, etc.), generating local inefficiency for the trigger. Insofar as these dead regions are in general much smaller than the size of the trigger patch, the effect on the jet yield is expected to be minor. It is accounted for by the detector-level simulations, which model the in-situ response of the EMCal accurately.

- Local inefficiency of the EMCal trigger system due to the exclusion of TRUs (section 6.1). It is this inefficiency, due specifically to the trigger system, that needs to be assessed.

Instead of simulating the trigger system response directly,[14] the trigger efficiency of the EMCal clusters measured in data is used to determine if a simulated event could be triggered or not. Figure 71 shows the trigger turn-on curves for the EMCal clusters in each SM from data, i.e. the ratio of the energy distribution of clusters that contain valid fired trigger patches in the triggered events to the energy distribution of all the clusters in the MB events. Constant lines are fit to the data points above 4-5 GeV/c depending on the SM, where the

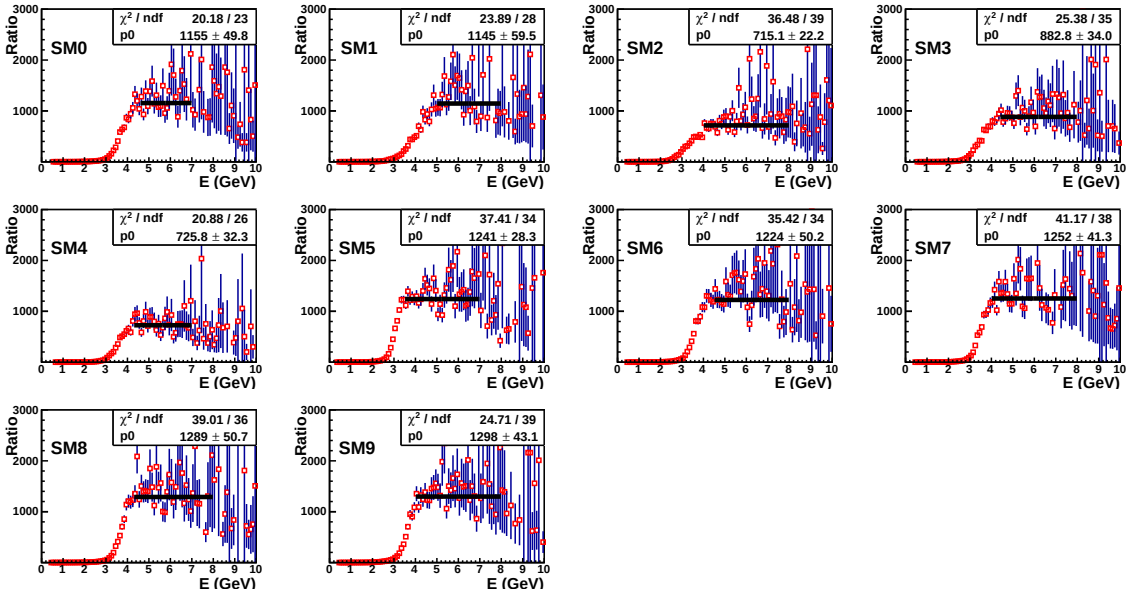

Figure 71: Trigger turn-on curves for the EMCal clusters in each individual SM from data. Constant lines are fit to the energy region where the trigger is expected to be fully efficient.

trigger is expected to be fully efficient. The fitted values are then used to normalize each turn-on curve to get the probability distribution for the EMCal SSh trigger to accept a cluster, which is unity at high E. The local efficiency of the trigger for clusters is assumed to follow the normalized turn-on curves if the TRU is functioning properly, and is 0 if the TRU is excluded. In order to account for the local variations, each EMCal cluster in a simulated event is accepted by the trigger with probability equal to the measured efficiency at that energy, for the SM in which it is located. A simulated event is accepted by the trigger if at least one EMCal cluster in the event satisfies the trigger requirement. The left panel of Fig. 72 shows the trigger efficiency for EMCal clusters in both data and simulation,

[14]This option is not available at the time of the analysis. Even though simulating the trigger response is the rigorous approach to estimate the trigger bias, in practice it very likely behaves similarly to the strategy used in this thesis.

where the data points are normalized to match simulation curve above 5 GeV. The right panel of Fig. 72 is the ratio the trigger efficiency curves of simulation to data and they agree within 20% over four orders of magnitudes. The trigger efficiency for jets is calculated using

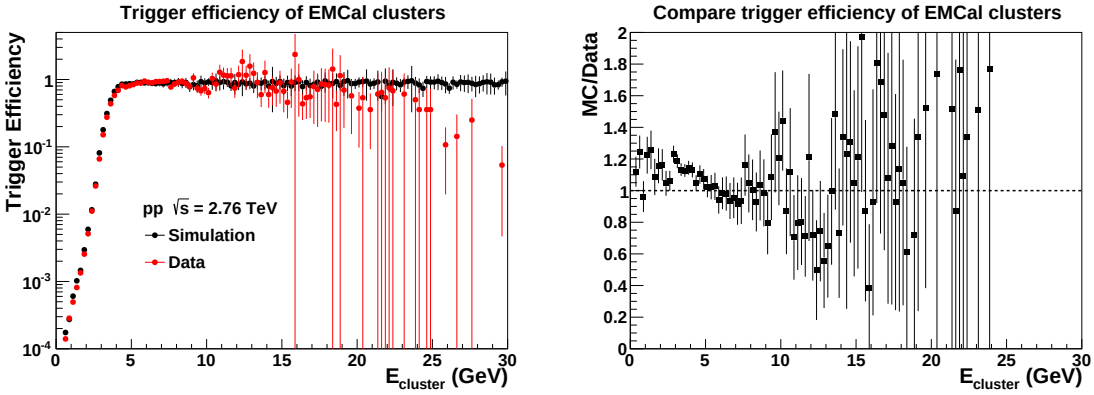

Figure 72: Left: the trigger efficiency for EMCal clusters in data (red) and simulation (black). The data points are normalized to match simulation curve above 5 GeV. Right: the ratio of the two distributions from the left plot (black/red).

distributions from detector-level simulations, for the fully inclusive jet population and for the population accepted by the simulated EMCal cluster trigger. The left panel of Fig. 73 shows the resulting trigger efficiency for $R = 0.4$ jets using this approach, overlaid with data points, which are scaled using the same normalization factor as in Fig. 72. As shown in

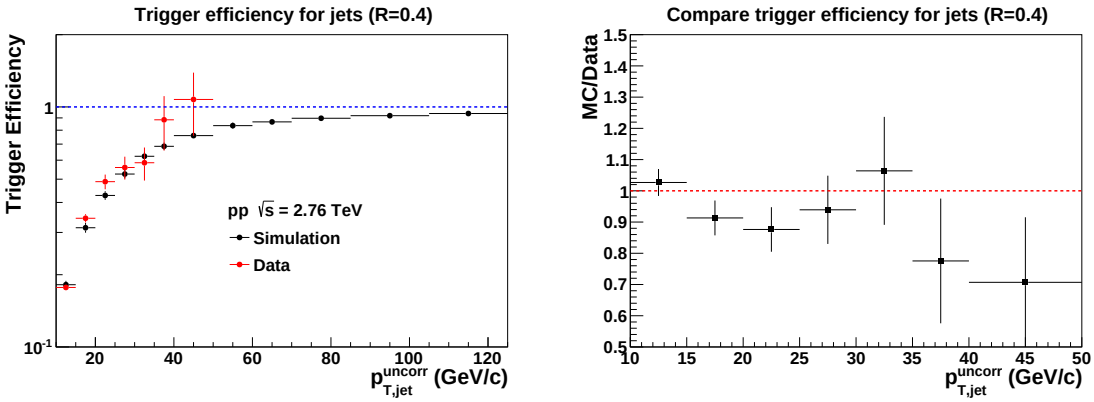

Figure 73: Left: trigger efficiency calculation via simulation (black) for $R = 0.4$ jets with comparison to data (red). Right: ratio of the two distributions from the left plot (black/red).

the right panel where the ratio of efficiencies in simulation to data is plotted, the efficiency from simulation in the turn-on region is lower than that in data by $5 - 10\%$. There are two possible sources for the discrepancy: (i) imperfection of the trigger simulation in the turn-on

region for clusters (see Fig. 72); (ii) mismatch of jet energy scale (JES) in simulation and data. Nevertheless, the agreement between data and simulation achieved in this approach is already satisfactory, which is also the case for the $R = 0.2$ jets. The black curve in the left panel of Fig. 73 is the trigger efficiency curve, $\epsilon_{\text{trigger}}(p_{\text{T}})$, used to calculate the jet cross section.

It is worth discussing the advantages and disadvantages of the two methods for estimating the trigger bias on jets. The purely data-driven method only uses data, and therefore does not have any model dependence. All trigger imperfections, including local threshold variation, online calibration issues, electronics problems, etc, are by definition incorporated into the triggered events, with the correct weighting by the integrated luminosity of different running conditions. Detailed investigation of run-dependent trigger performance is not required. However, application of the fully data-driven method requires care if the trigger bias depends on the observable. This method is also limited, by the available MB statistics, in the precision to which it can constrain the normalization of the efficiency plateau region. On the other hand, the available statistics of the MB sample is not relevant for the method incorporating simulations. It is partially data-driven, in that the EMCal cluster trigger efficiency is derived from data, though that also requires detailed investigations of trigger performance in data. In addition, the method relies on accurate PYTHIA modeling of the jet fragmentation and GEANT simulation of the EMCal clusters.

7.2.2 Trigger acceptance

The EMCal SSh trigger acceptance is less than unity due to the excluded parts of the trigger system. It can be estimated using the trigger efficiency of the clusters in simulation since the loss of the high energy clusters in the triggered simulated events is solely due to the masked-out regions. The efficiency is shown in Fig. 74, and a fit at the plateau gives:

$$A_{\text{trigger}} = 0.89 \pm 0.004 \tag{60}$$

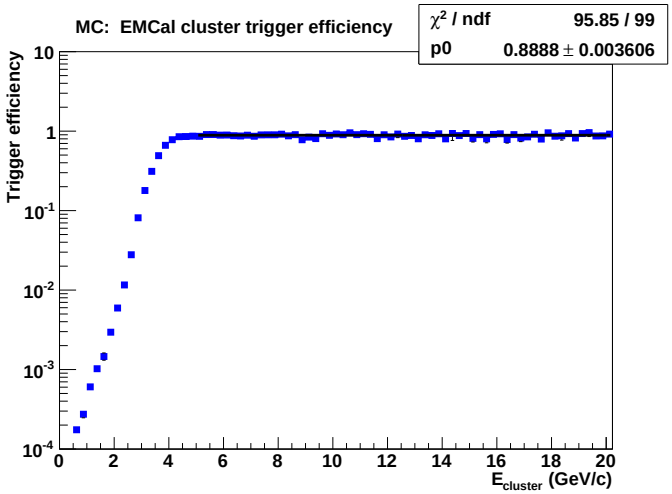

Figure 74: Trigger efficiency for EMCal clusters in simulation fitted with a constant line above 5 GeV.

8 Correction to particle level

The inclusive jet distribution is corrected to the particle level, with the correction factors calculated based on PYTHIA and detailed GEANT modeling of the ALICE detector. No correction is made for hadronization effects that may modify the energy in the jet cone at the particle level relative to the parton level[15]. This choice is made to facilitate future comparison to jet measurements in heavy-ion collisions, where correction to the parton level is not well-defined at present.

Corrections are applied bin-by-bin [98], with the correction factor for each bin defined as:

$$C_{\mathrm{MC}}\left(p_{\mathrm{T}}^{\mathrm{low}};p_{\mathrm{T}}^{\mathrm{high}}\right)=\frac{\int_{p_{\mathrm{T}}^{\mathrm{low}}}^{p_{\mathrm{T}}^{\mathrm{high}}}\mathrm{d}p_{\mathrm{T}}\frac{\mathrm{d}F_{\mathrm{meas}}^{\mathrm{uncorr}}}{\mathrm{d}p_{\mathrm{T}}}\cdot\frac{\mathrm{d}\sigma_{\mathrm{MC}}^{\mathrm{particle}}/\mathrm{d}p_{\mathrm{T}}}{\mathrm{d}\sigma_{\mathrm{MC}}^{\mathrm{detector}}/\mathrm{d}p_{\mathrm{T}}}}{\int_{p_{\mathrm{T}}^{\mathrm{low}}}^{p_{\mathrm{T}}^{\mathrm{high}}}\mathrm{d}p_{\mathrm{T}}\frac{\mathrm{d}F_{\mathrm{meas}}^{\mathrm{uncorr}}}{\mathrm{d}p_{\mathrm{T}}}}, \tag{61}$$

where $\mathrm{d}\sigma_{\mathrm{MC}}^{\mathrm{particle}}/\mathrm{d}p_{\mathrm{T}}$ and $\mathrm{d}\sigma_{\mathrm{MC}}^{\mathrm{detector}}/\mathrm{d}p_{\mathrm{T}}$ are the particle-level and detector-level inclusive jet spectra from PYTHIA; $\frac{\mathrm{d}F_{\mathrm{meas}}^{\mathrm{uncorr}}}{\mathrm{d}p_{\mathrm{T}}}$ is a parametrization of the measured, uncorrected inclusive jet distribution, which provides a weight function to minimize the dependence on the spectral shape of the simulation; $p_{\mathrm{T}}^{\mathrm{low}}$ and $p_{\mathrm{T}}^{\mathrm{high}}$ are the bin limits. The ratio in the numerator of the particle-level and detector-level cross sections at fixed p_{T} incorporates all detector effects included in the simulation.

8.1 Validate simulation

The simulation used to calculate the correction factors is checked extensively with data in terms of key jet observables to make sure it reproduces all the relevant detector effects correctly.

Neutral energy fraction (NEF): it is defined as the fraction of total jet energy carried by the EMCal clusters. Figure 75 compares the mean NEF as a function of $p_{\mathrm{T,jet}}^{\mathrm{uncorr}}$ for $R = 0.2$ (left) and $R = 0.4$ (right) jets from MB data, EMCal-triggered data, MB simulation as well as triggered simulation (described in section 7.2.1). In general, the simulation agrees well with both MB and triggered data sample for jets with $p_{\mathrm{T,jet}}^{\mathrm{uncorr}} < 70$ GeV/c. Above 70

[15] Jet finding is performed directly on the parent partons, instead of the particles from the parton fragmentation.

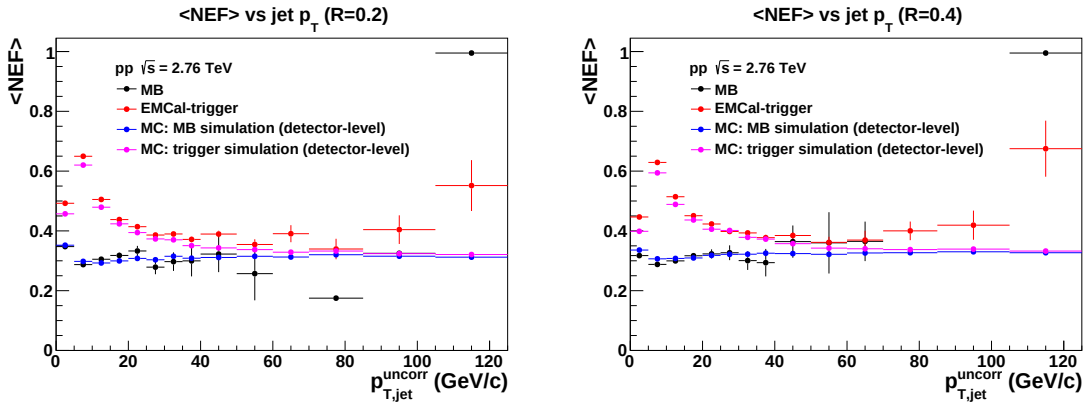

Figure 75: Mean NEF as a function of $p_{\mathrm{T,jet}}^{\mathrm{uncorr}}$ for $R = 0.2$ (left) and $R = 0.4$ (right) jets from MB data (black), EMCal-triggered data (red), MB simulation (blue) and triggered simulation sample (magenta).

GeV/c, the deviation is mainly due to the limited statistics in data. A more differential comparison of the actual distributions of jet NEF ($R = 0.4$) is shown in Fig. 76 in four different $p_{\mathrm{T,jet}}^{\mathrm{uncorr}}$ bins. Good agreement is also observed for these distributions.

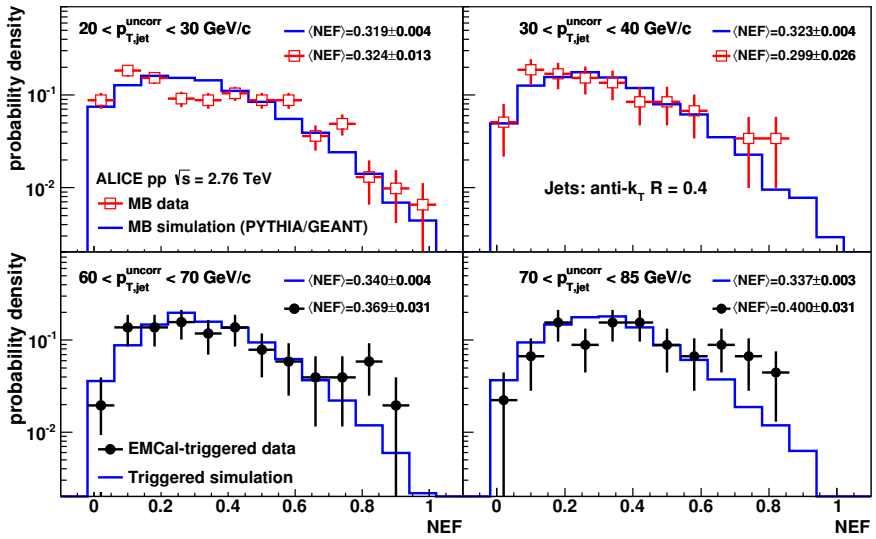

Figure 76: Jet NEF distributions for MB data (open squares), EMCal-triggered data (filled circles) and simulations (histograms), in four different $p_{\mathrm{T,jet}}^{\mathrm{uncorr}}$ intervals.

Jet constituents: the mean number of jet constituents, mean charged constituent p_{T} and mean neutral constituent p_{T} as a function of $p_{\mathrm{T,jet}}^{\mathrm{uncorr}}$ are shown in Figs. 77, 78 and 79, respectively, for $R = 0.2$ (left) and $R = 0.4$ (right) jets from data and simulation. Good agreements are observed, which confirms that the detector simulation is indeed able to

reproduce the effects in real data.

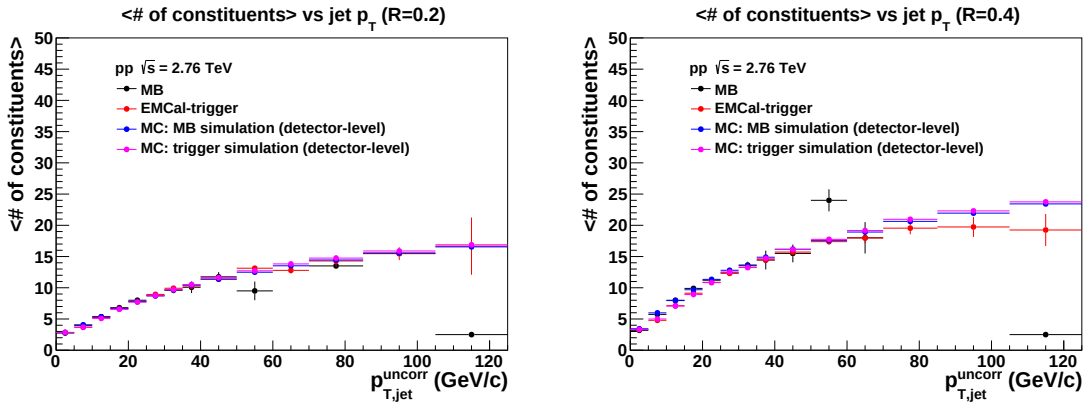

Figure 77: Mean number of jet constituents as a function of $p_{\mathrm{T,jet}}^{\mathrm{uncorr}}$ for $R = 0.2$ (left) and $R = 0.4$ (right) jets from MB data (black), EMCal-triggered data (red), MB simulation (blue) and triggered simulation sample (magenta).

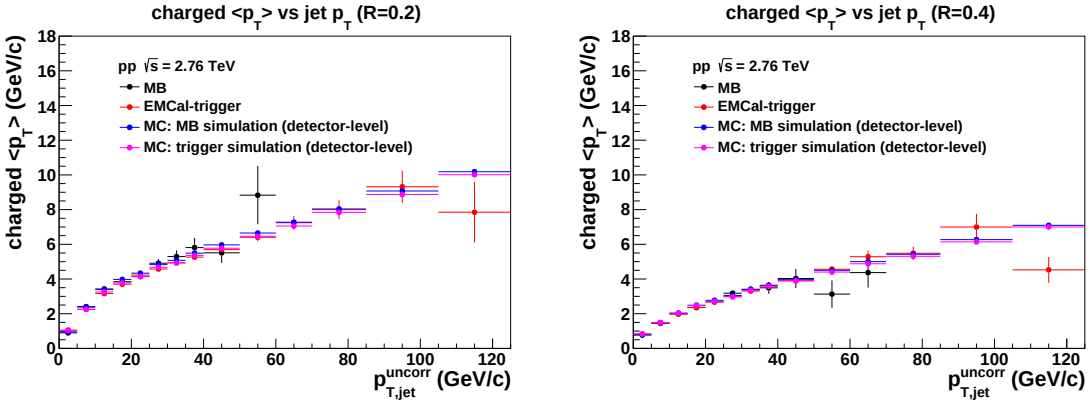

Figure 78: Mean charged constituent p_{T} as a function of $p_{\mathrm{T,jet}}^{\mathrm{uncorr}}$ for $R = 0.2$ (left) and $R = 0.4$ (right) jets from MB data (black), EMCal-triggered data (red), MB simulation (blue) and triggered simulation sample (magenta).

8.2 Detector effects

The overall effect of the detector response, as modeled by GEANT, can be quantified by comparing jet p_{T} at the particle level ($p_{\mathrm{T,jet}}^{\mathrm{particle}}$) and detector level ($p_{\mathrm{T,jet}}^{\mathrm{detector}}$) on a jet-by-jet basis in simulation. Detector and particle level jets are matched based on the proximity of their centroids in (η, φ) with cuts: $\Delta R = \sqrt{(\Delta\varphi)^2 + (\Delta\eta)^2} < 0.25$ for $R = 0.4$ jets and $\Delta R < 0.1$ for $R = 0.2$ jets. The resulting response matrices are shown in Fig. 80 for $R = 0.2$ (left) and $R = 0.4$ (right) jets, respectively.

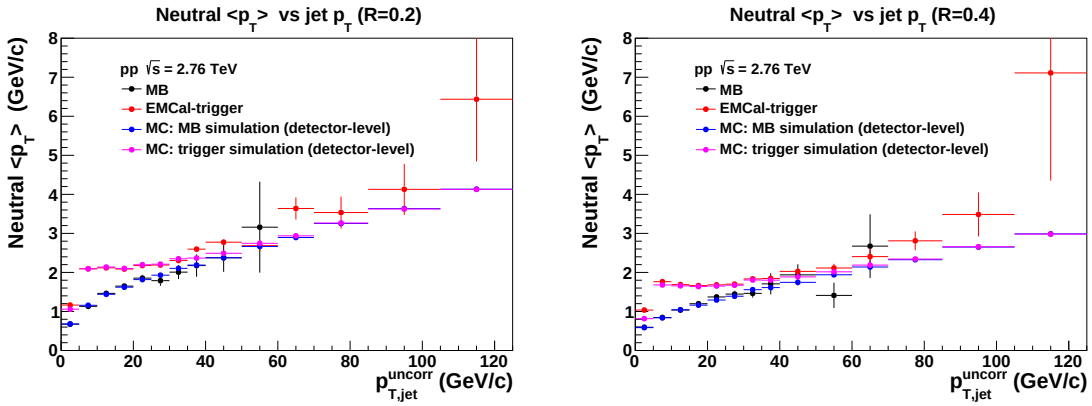

Figure 79: Mean neutral constituent p_{T} as a function of $p_{\mathrm{T,jet}}^{\mathrm{uncorr}}$ for $R = 0.2$ (left) and $R = 0.4$ (right) jets from MB data (black), EMCal-triggered data (red), MB simulation (blue) and triggered simulation sample (magenta).

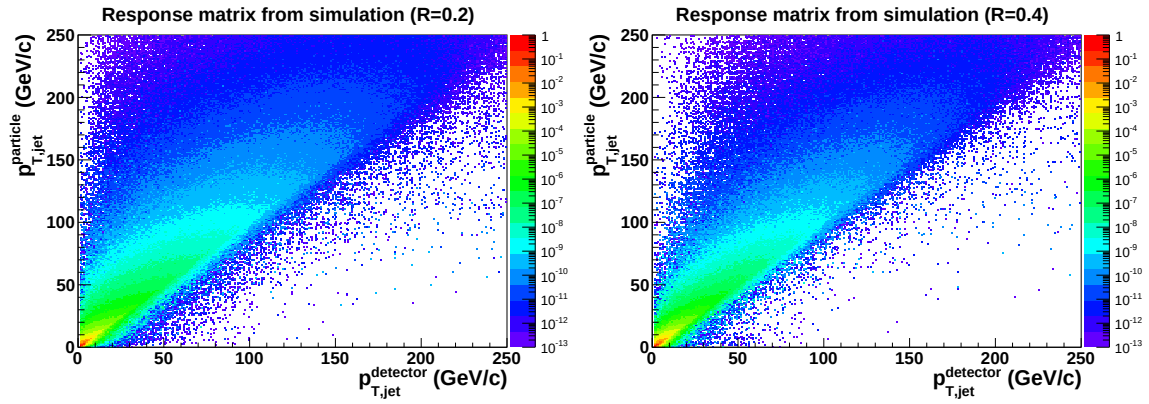

Figure 80: Detector response matrices for jets with $R = 0.2$ (left) and $R = 0.4$ (right).

The relative p_{T} shifts between particle and detector level jets $(p_{\mathrm{T,jet}}^{\mathrm{detector}} - p_{\mathrm{T,jet}}^{\mathrm{particle}})/p_{\mathrm{T,jet}}^{\mathrm{particle}}$ are plotted in Fig. 81 in all $p_{\mathrm{T,jet}}^{\mathrm{particle}}$ bins. In all cases, $p_{\mathrm{T,jet}}^{\mathrm{detector}}$ is smaller than $p_{\mathrm{T,jet}}^{\mathrm{particle}}$ with

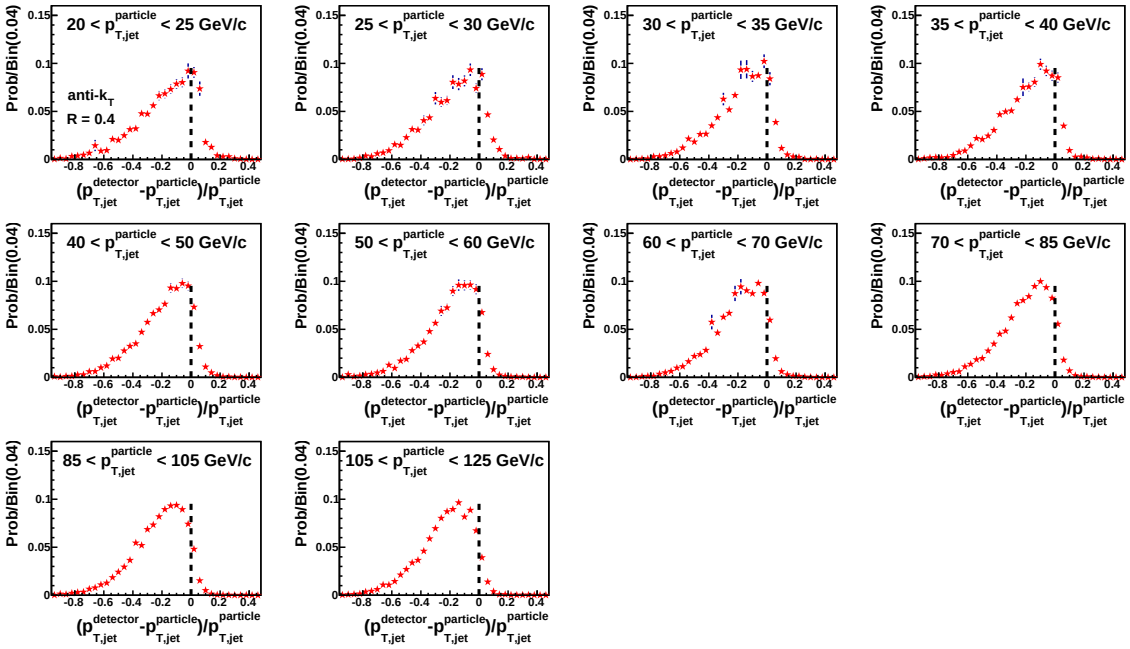

Figure 81: The relative p_{T} shift between particle level and detector level jets in various particle level jet p_{T} bins ($R = 0.4$).

high probability. This occurs because the largest detector-level effects are due to unobserved particles, i.e. finite charged particle tracking efficiency and undetected neutrons and $\mathrm{K}_{\mathrm{L}}^{0}$'s. Large upward fluctuations in the detector response ($p_{\mathrm{T,jet}}^{\mathrm{detector}} > p_{\mathrm{T,jet}}^{\mathrm{particle}}$), which are much less probable, are due predominantly to rare track configurations in which daughters of secondary vertices are incorrectly reconstructed with high p_{T}, with their contribution not eliminated by the cuts described in sections 6.2 and 6.4.1. Comparison of simulations and data show that these configurations are accurately modeled in the simulations. Insofar as their rate in data is small, they make negligible contribution to the measured jet spectrum. The $(p_{\mathrm{T,jet}}^{\mathrm{detector}} - p_{\mathrm{T,jet}}^{\mathrm{particle}})/p_{\mathrm{T,jet}}^{\mathrm{particle}}$ distributions can be partially characterized in terms of mean, median and standard deviation, as shown in Fig. 82. The median correction to the JES is $\sim 15\%$ at $p_{\mathrm{T,jet}} = 25$ GeV/c and $\sim 19\%$ at $p_{\mathrm{T,jet}} = 100$ GeV/c. The right panel shows the standard deviation, corresponding to an estimate of JER approximately 18%.

Since the distributions in Fig. 81 are significantly non-Gaussian, especially at low $p_{\mathrm{T,jet}}^{\mathrm{particle}}$, the full distributions are used to determine $\mathrm{d}\sigma_{\mathrm{MC}}^{\mathrm{detector}}/\mathrm{d}p_{\mathrm{T}}$ in C_{MC}. With all the

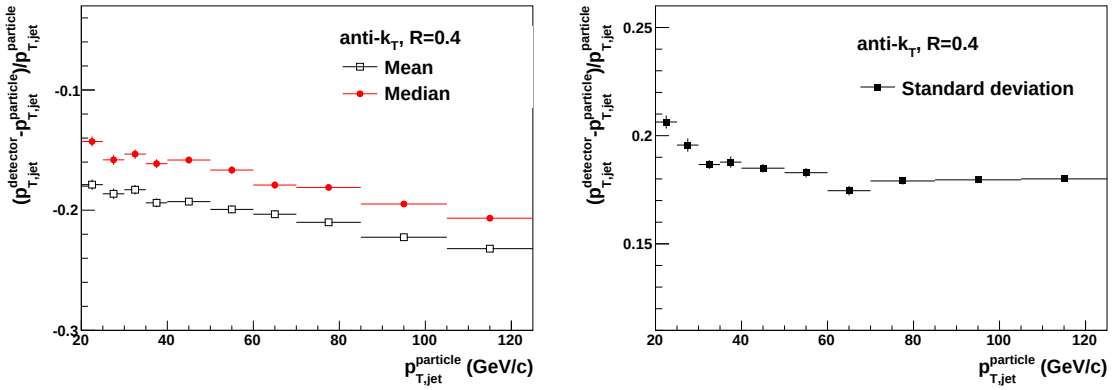

Figure 82: Mean and median (left), and standard deviation (right) of the $(p_{\mathrm{T,jet}}^{\mathrm{detector}} - p_{\mathrm{T,jet}}^{\mathrm{particle}})/p_{\mathrm{T,jet}}^{\mathrm{particle}}$ distributions as a function of particle level jet p_{T} ($R = 0.4$).

detector effects taken into account, the magnitudes of C_{MC} for $R = 0.2$ (left) and $R = 0.4$ (right) jets are illustrated in Fig. 83. The gray band around the data points represents

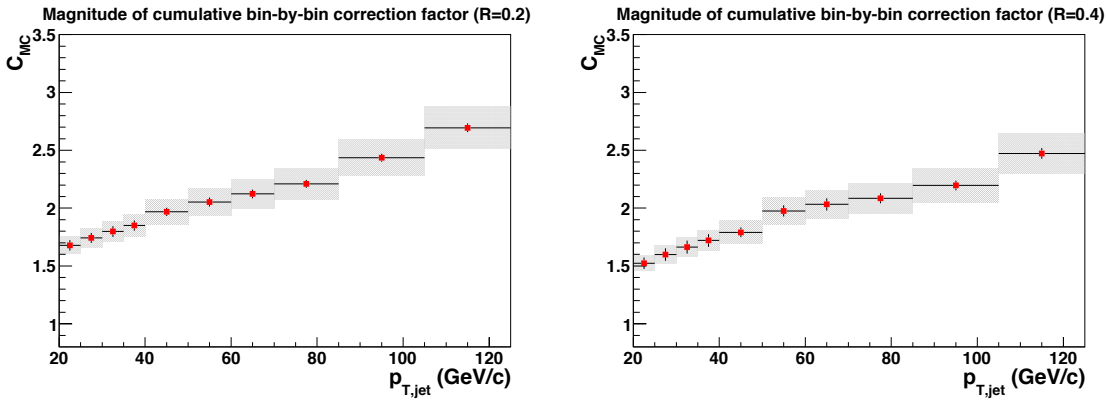

Figure 83: Overall bin-by-bin correction factor (Eq. 61) for $R = 0.2$ (left) and $R = 0.4$ (right) jets as a function of jet p_{T}.

the systematic uncertainty due to the input spectral shape $(\mathrm{d}\sigma_{\mathrm{MC}}^{\mathrm{particle}}/\mathrm{d}p_{\mathrm{T}})$ as discussed in section 10.2.1. For $R = 0.2$, C_{MC} rises monotonically from 1.7 at $p_{\mathrm{T,jet}} = 20$ GeV/c to 2.7 at $p_{\mathrm{T,jet}} = 120$ GeV/c, while for $R = 0.4$, C_{MC} rises monotonically from 1.5 at $p_{\mathrm{T,jet}} = 20$ GeV/c to 2.5 at $p_{\mathrm{T,jet}} = 120$ GeV/c.

The individual contributions to the C_{MC} calculation are discussed in the following sections.

8.2.1 Unmeasured neutron and K^0_L energy

Neutrons and K^0_L's are not measured by the ALICE central barrel, which generates a systematic deficit in the measured jet energy. The magnitude of the deficit is determined utilizing particle-level simulations. Jet finding is run twice on each simulated event, first on the full set of particles, and then excluding neutrons and K^0_L's. Jets in the two samples are matched by requiring a small distance between the jet centroids[16] and the difference between the reconstructed energies for each pair of matched jets is calculated.

Figure 84 shows the distribution of fractional energy shift $\Delta p_T^{NK}/p_T = (p_{T,jet}^{NK} - p_{T,jet}^{no\ NK})/p_{T,jet}^{NK}$ for selected intervals of $p_{T,jet}^{NK}$, where "NK" indicates that neutrons and K^0_L's are included, and "no NK" indicates that they are excluded. Positive $\Delta p_T^{NK}/p_T$ indicates energy deficit due to missing neutrons and K^0_L's. In rare cases, this quantity may be negative, due to the interference of the measured jet hadrons with the underlying event. However, the main features of the distribution for all jet selections are

- A sharp peak at zero, indicating *no* energy deficit, corresponds to $\sim 45-70\%$ of the jet population depending on jet p_T and cone radius. Such jets do not contain neutrons or K^0_L's among their fragments.
- $|\Delta p_T^{NK}/p_T| < 10\%$ corresponds to $\sim 75\%$ of the jet population.

The magnitude of the bin-by-bin correction for this effect is assessed by comparing the inclusive particle-level jet spectra excluding and including neutrons and K^0_L's. As shown in Fig. 85, it increases as a function of $p_{T,jet}$ for jets with both radii, which is consistent with the behavior observed in Fig. 83.

8.2.2 Tracking efficiency

Not all charged tracks are detected, due to finite tracking efficiency (see section 6.2), which also generates a deficit in measured jet energy. As was done for the unmeasured neutron and K^0_L contribution in Section 8.2.1, we can evaluate the magnitude of correction due to

[16] We find that alternative matching criteria, based on finding jets that share a certain fraction of the particles in the event, induce fragmentation biases that are difficult to disentangle from the effect we are investigating.

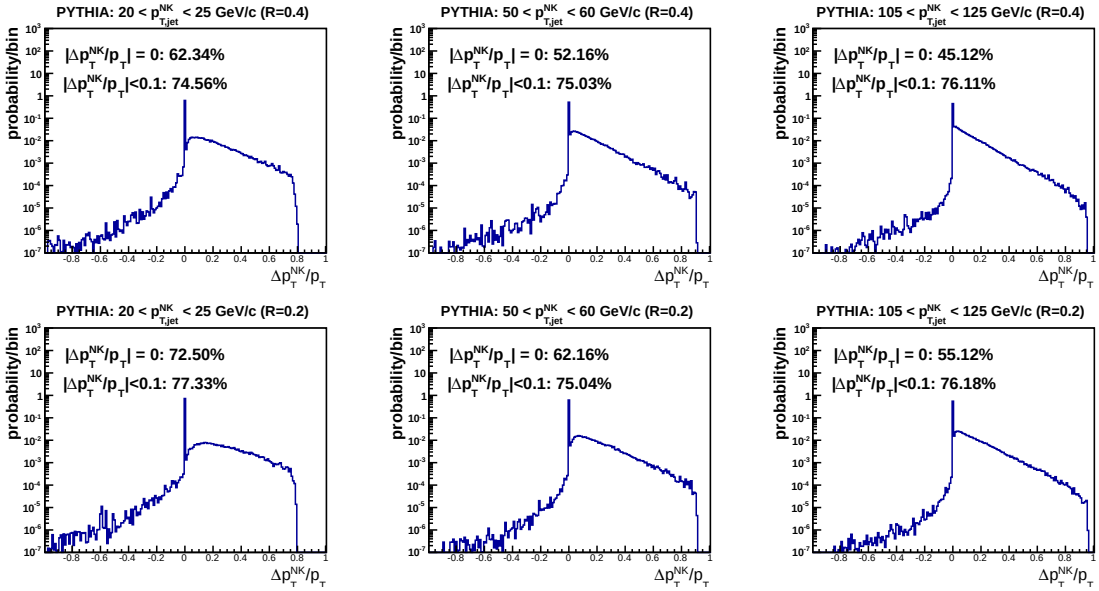

Figure 84: Distribution of relative missing p_{T} due to missing neutrons and $\mathrm{K}^0_{\mathrm{L}}$'s for $R = 0.4$ (upper) and $R = 0.2$ (lower) jets.

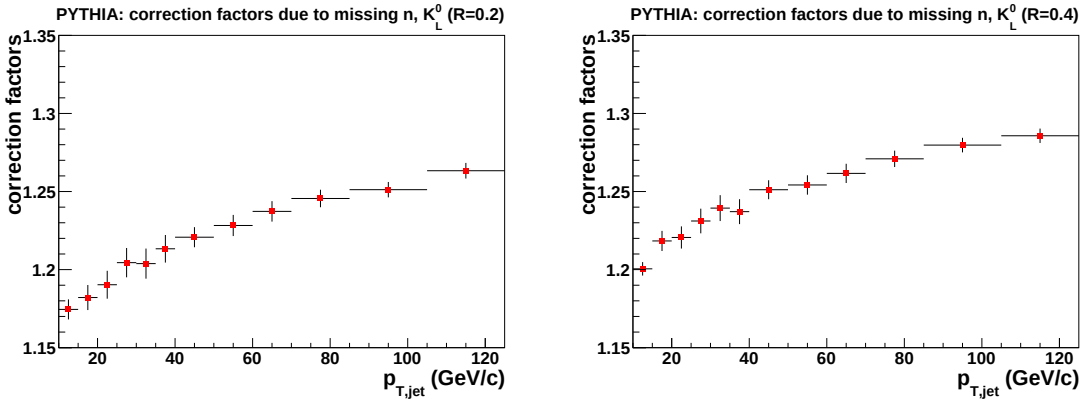

Figure 85: Bin-by-bin correction factors due to unmeasured neutrons and $\mathrm{K}^0_{\mathrm{L}}$'s estimated using PYTHIA events at particle level for $R = 0.2$ (left) and $R = 0.4$ (right) jets.

tracking efficiency on a jet-by-jet basis by matching particle level jets from PYTHIA events with and without tracking efficiency included. To mimic tracking inefficiency, charged particles are randomly thrown away according to the estimated tracking efficiency, shown in Fig. 48 as the blue points. Figure 86 shows the distribution of fractional energy shift $\Delta p_{\mathrm{T}}^{\mathrm{TrkEff}}/p_{\mathrm{T}} = (p_{\mathrm{T,jet}}^{\text{no TrkEff}} - p_{\mathrm{T,jet}}^{\mathrm{TrkEff}})/p_{\mathrm{T,jet}}^{\text{no TrkEff}}$ for selected intervals of $p_{\mathrm{T,jet}}^{\text{no TrkEff}}$, where "no TrkEff" indicates that tracking efficiency is not incorporated , and "TrkEff" indicates that it is incorporated. The characteristics of Fig. 86 are very similar to those of Fig. 84, namely

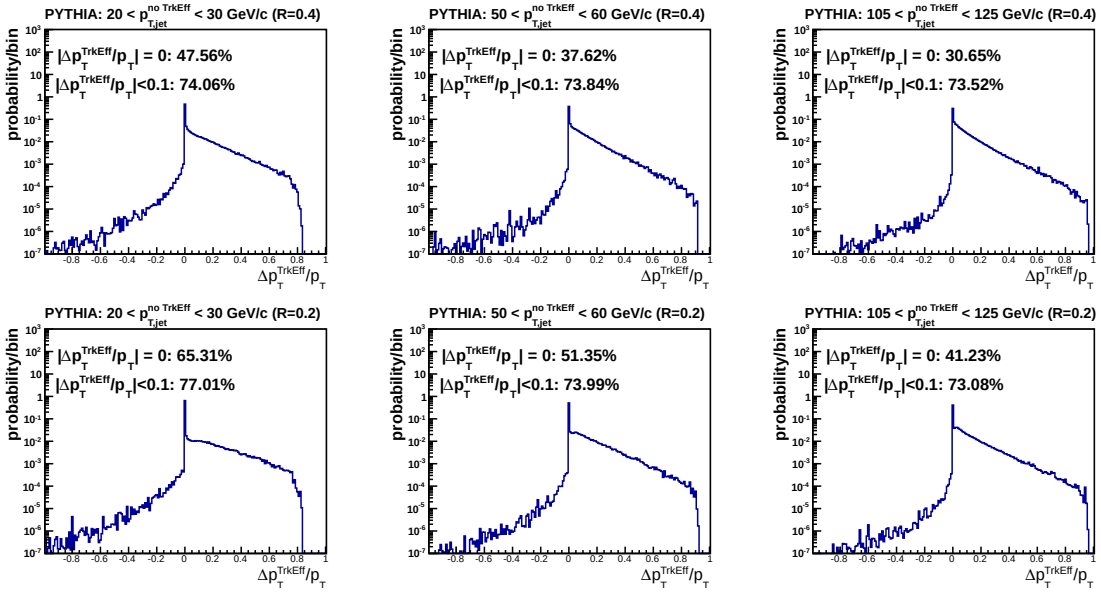

Figure 86: Distribution of relative missing p_{T} due to tracking efficiency for $R = 0.4$ (upper) and $R = 0.2$ (lower) jets.

a peak at 0 and a long tail to the right. However there are fewer jets in the peaks of Fig. 86, which indicates larger correction factors, as confirmed by Fig. 87.

The magnitude of the bin-by-bin correction for tracking efficiency is determined by comparing the inclusive jet spectra for PYTHIA events at the particle level, with and without tracking efficiency incorporated. Figure 87 displays the magnitude of the correction, which increases as a function of jet p_{T} for both $R = 0.2$ (left) and $R = 0.4$ (right) jets as well.

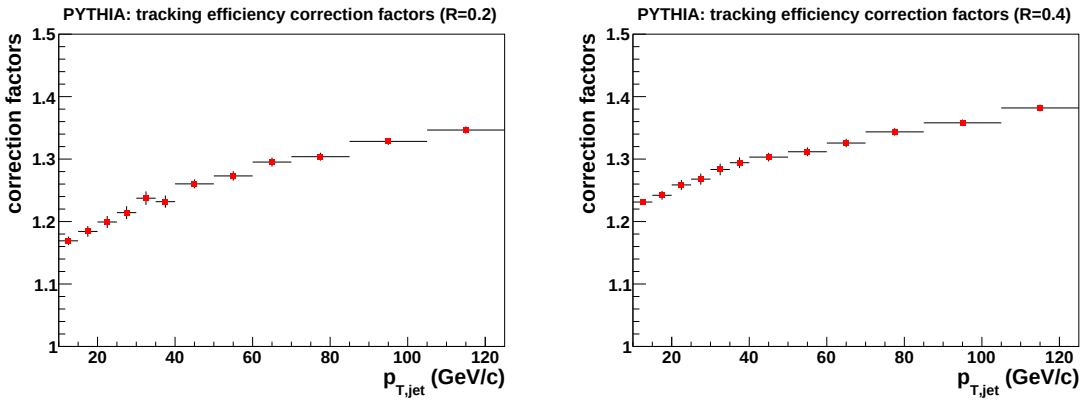

Figure 87: Bin-by-bin correction factors due to tracking efficiency estimated using PYTHIA events at particle level for $R = 0.2$ (left) and $R = 0.4$ (right) jets.

8.2.3 Missing secondary particles from weak decays

Strange particles, K^0_S, Λ and other hyperons, can decay into both neutral and charged secondary particles via weak processes. The neutral secondary particles are predominantly π^0's, whose energies are measured by EMCal almost without efficiency loss. One exception is that when the π^0 decays into photons, which then convert into electron-positron pairs, part of its energy can be missed if the electron or positron trajectories bend (magnetically) out of the acceptance. Although this effect is found to be small, it is included in the simulation. On the other hand, the detection efficiency for the charged secondary particles is expected to be low, due to their broad DCA distribution and the strict DCA cut used in the analysis. Therefore, it makes sizable contribution to the total correction factors, and has to be taken into account.

The detector response to weakly decaying particles can be obtained by comparing their p_T on the particle and detector levels under the assumption that the neutral secondary particles can be measured precisely with full efficiency. With this detector response in hand, the effects of missing charged secondary particles are assessed on a jet-by-jet basis using the same technique as in sections 8.2.1 and 8.2.2. Figure 88 shows the distribution of fractional energy shift $\Delta p_T^{Sec}/p_T = (p_{T,jet}^{no\ Sec} - p_{T,jet}^{Sec})/p_{T,jet}^{no\ Sec}$ for selected intervals of $p_{T,jet}^{no\ Sec}$, where "Sec" and "no Sec" correspond to with and without incorporating detector response of the weakly decaying particles in PYTHIA events. With the same technique, the magnitude of the bin-by-bin correction factors due to the missing charged secondary particles is determined and

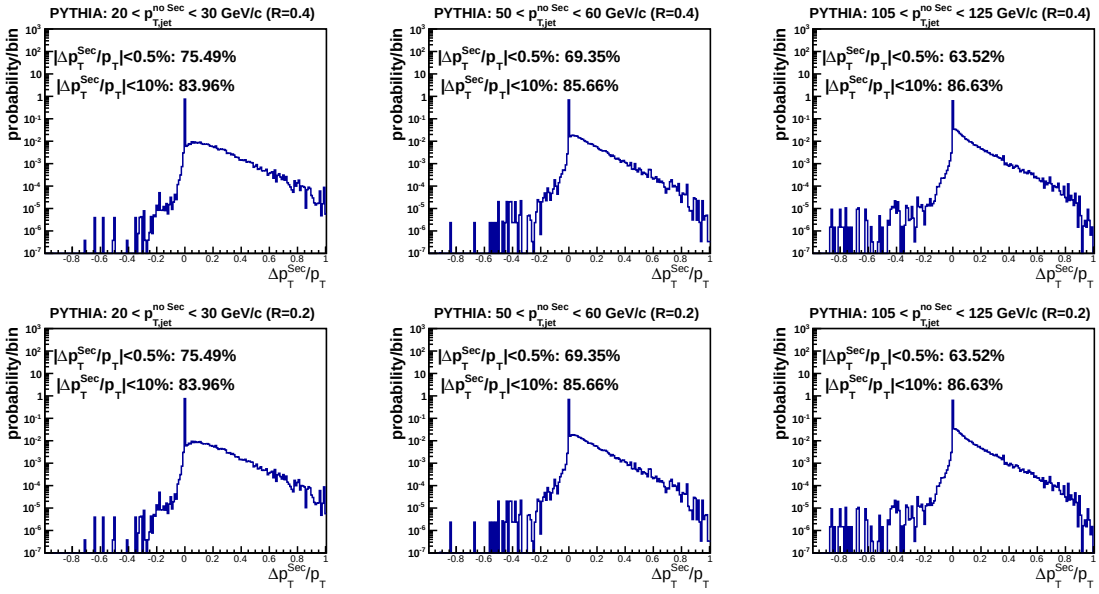

Figure 88: Distribution of relative missing p_{T} due to missing charged secondary particles for $R = 0.4$ (upper) and $R = 0.2$ (lower) jets.

shown in Fig. 89. It increases slightly as a function of jet p_{T} for both $R = 0.2$ (left) and $R = 0.4$ (right) jets. The magnitude of this correction is smaller than that due to missing neutrons and $\mathrm{K}^0_{\mathrm{L}}$'s or tracking efficiency, which is consistent with the observation that more jets are contained in the peaks of Fig. 88.

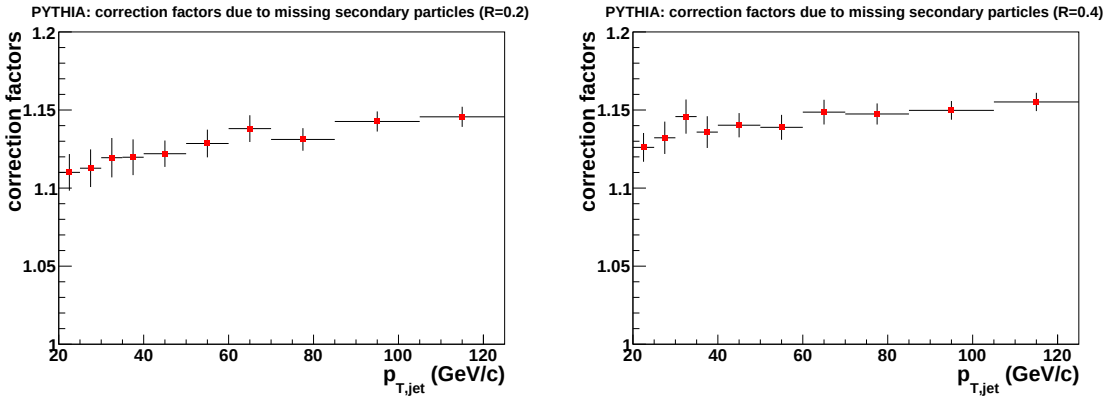

Figure 89: Bin-by-bin correction factors due to missing charged secondary particles estimated using PYTHIA events at particle level for $R = 0.2$ (left) and $R = 0.4$ (right) jets.

8.2.4 Residual charged-energy double counting

As discussed in section 6.3.3, double counting of charged hadronic energy in the EMCal is corrected via matching tracks to EMCal clusters and subtracting a fraction f_{sub} of the track momentum from the cluster energy, with truncation to zero when the subtraction gives a negative value. Values for f_{sub} between 0.7 and 1 are seen to generate a consistent and stable correction and the default is chosen to be $f_{\mathrm{sub}} = 1$. However, this correction is only approximate, and the residual effects of hadronic energy double counting may remain and require additional correction. In particular, over-subtraction by this method can occur if both neutral and charged particles contribute to a cluster and the hadronic shower is only partially contained. The requirement that cluster energy be positive will not catch all such cases, which are more frequent for higher energy jets with larger particle density. For detector-level simulations, the same hadronic correction is applied prior to running the jet finder. The bin-by-bin correction (or response matrix) therefore includes the residual

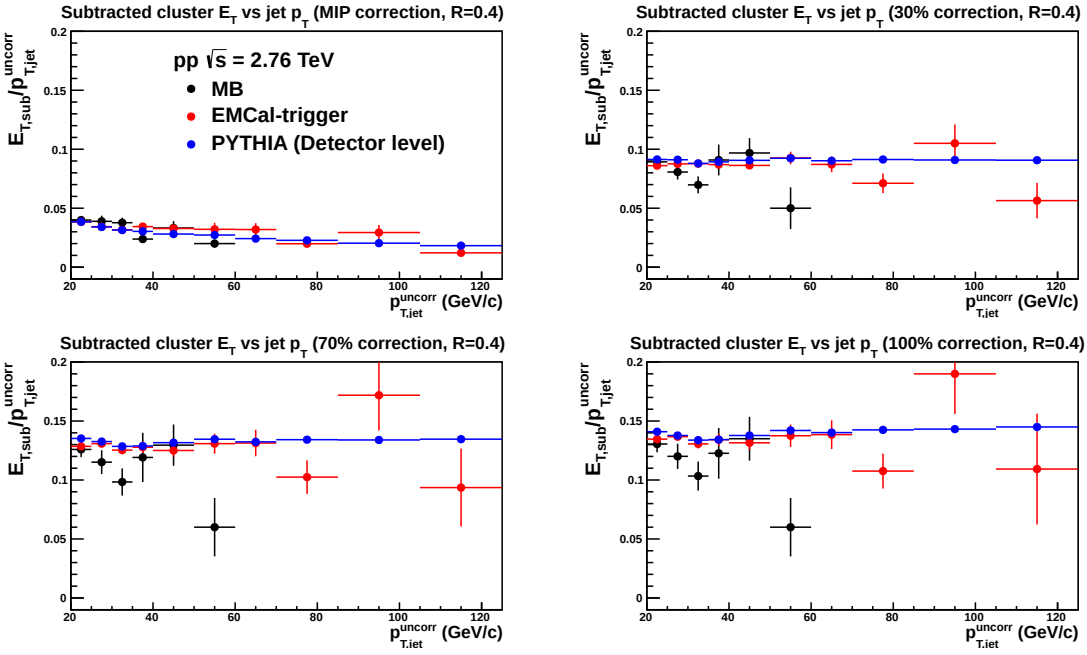

Figure 90: Mean relative energy subtracted in hadronic correction as a function of jet p_{T}, for PYTHIA detector level events and for MB and EMCal-triggered data using MIP correction and various choices of f_{sub}. See text.

correction when comparing detector-level and particle-level distributions. It is valuable to assess how accurately the simulation models the effects of this procedure, via comparison

to data. For each jet, the total energy subtracted from EMCal clusters in the jet due to the hadronic correction is determined, and its fraction relative to the total uncorrected jet energy is calculated; in other words, the relative energy reduction due to the hadronic correction is studied. This quantity can be calculated for any choice of f_{sub}, and can likewise be calculated in both data and detector-level simulation for comparison. Figure 90 shows the mean relative energy subtracted in hadronic correction as a function of jet p_{T}, for PYTHIA detector-level events and for MB and EMCal-triggered data. The upper left panel corresponds to a MIP correction, while the other panels correspond to $f_{\mathrm{sub}} = 0.3, 0.7,$ and 1. Within the resolution achievable by this comparison, the detector-level simulation is seen to agree to better than a few percent with data for $p_{\mathrm{T,jet}}^{\mathrm{uncorr}} > 20$ GeV/c for all choices of f_{sub} and MIP correction.

8.2.5 Intrinsic detector resolution

The contribution to the JER due to the energy resolution of the constituent tracks and clusters can be calculated on a jet-by-jet basis:

$$\sigma^2(p_{\mathrm{T,jet}}) = \sum \sigma^2(p_{\mathrm{T,track}}) + \sum \sigma^2(E_{\mathrm{T,cluster}}) \tag{62}$$

where

$$\sigma^2(E_{\mathrm{T,cluster}}) = \sigma^2(E_{\mathrm{T,cluster}}^{\text{before subtraction}}) + f_{\mathrm{sub}}^2 \sum \sigma^2(p_{\mathrm{T,track}}^{\mathrm{matched}}). \tag{63}$$

The sum is over all charged track and EMCal cluster constituents. The transverse momentum resolution $\sigma(p_{\mathrm{T,track}})$ for charged tracks is estimated using the covariance matrix of the Kalman filter (Fig. 49), while the energy resolution $\sigma(E_{\mathrm{T,cluster}})$ for EMCal clusters is extracted from the 2010 test beam data (Fig. 38). Figure 91 shows the profile of the relative jet p_{T} resolution, measured using Eq. 62, as a function of jet p_{T} for $R = 0.2$ and $R = 0.4$ jets in MB and EMCal-triggered data sets. The contribution of the detector resolution to the JER is found to be $\sim 1 - 2\%$. Also shown is the same quantity calculated in the detector-level simulation, which is slightly better than in data. Nevertheless, since the detector resolution makes a very small contribution to the bin-by-bin correction and the

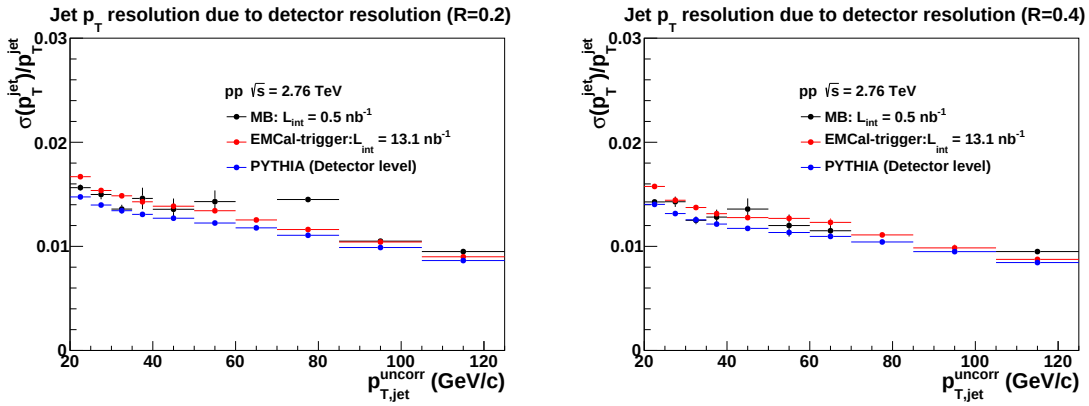

Figure 91: Contribution to the JER by the detector resolution (Eq. 62) as a function of $p_{\mathrm{T,jet}}^{\mathrm{uncorr}}$ for $R = 0.2$ (left) and $R = 0.4$ (right) jets.

estimated systematic uncertainties, simulations are not adjusted to match precisely that measured in the data.

8.2.6 Non-linearity due to minimum p_{T} cuts

Non-linearity in the energy response will arise due to the low p_{T} cut on charged tracks ($p_{\mathrm{T}} > 0.15$ GeV/c), EMCal towers ($E > 0.05$ GeV), and EMCal clusters ($E > 0.3$ GeV). Figure 92 shows the estimated effect of such cuts, through the comparison of jet spectra on PYTHIA particle-level which include all particles in the event, or exclude particles with p_{T} less than 0.15 GeV/c. Only a loss of less than 2% in the jet yield is observed due to the

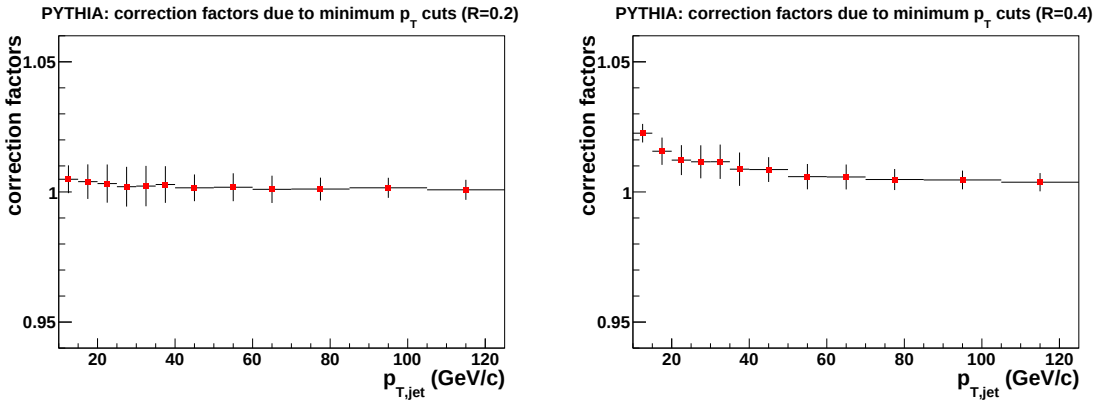

Figure 92: Bin-by-bin correction factors due to minimum kinematic cuts on the jet constituents, estimated using PYTHIA events at particle level for $R = 0.2$ (left) and $R = 0.4$ (right) jets.

minimum kinematic cuts.

8.2.7 z_{leading} cut

The magnitude of the correction due to the z_{leading} cut (section 6.4.1) is estimated by comparing the inclusive jet spectra from PYTHIA particle-level events, with and without z_{leading} cut, as shown in Fig. 93 for $R = 0.2$ and $R = 0.4$ jets, respectively. Above 20 GeV/c, the effect of the z_{leading} cut is seen to be less than 1%, as expected from the same analysis using data (Fig. 63).

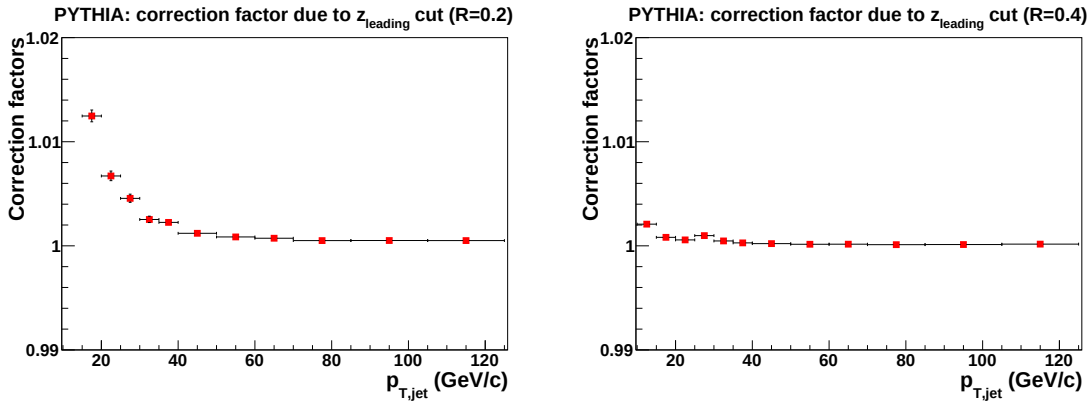

Figure 93: Bin-by-bin correction factors due to $z_{\text{leading}} < 0.98$ cut estimated using PYTHIA events at particle level for $R = 0.2$ (left) and $R = 0.4$ (right) jets.

8.3 Underlying event subtraction

The underlying event (UE) in the collision is not part of the jet fragmentation, so its contribution to jet energy must be subtracted for comparison to theoretical calculations. There are two ways to estimate the UE density [99]:

- "Leading jet" events: for each event find the leading jet (jet #1) in the event and sum up p_{T} of all the particles in a cone of $R = 0.4$ perpendicular to the leading jet axis. See left panel of Fig. 94.

- "Back-to-back" events: besides the leading jet (jet #1) in the event, a back-to-back jet (jet #2), satisfying $|\Delta\varphi| > 5/6\pi$ and carrying more than 80% of the transverse momentum of the leading jet, is required to be also present in the event. Additionally, all the other jets in the event should have $p_{\text{T,jet}} < 15$ GeV/c. Again, the UE density

is estimated as the summed p_{T} of all particles in a cone of $R = 0.4$ perpendicular to the leading jet axis. See right panel of Fig. 94.

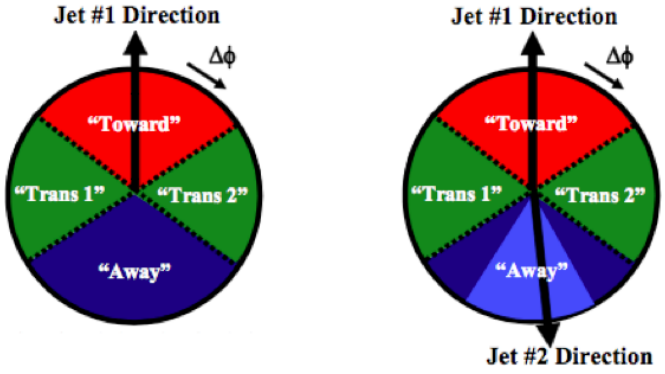

Figure 94: Illustration of "leading jet" (left) and "back-to-back" (right) events [99].

Both "leading jet" and "back-to-back" event samples are used to assess the UE density for PYTHIA particle-level events, whose dependence on the leading jet p_{T} is shown in the left panel of Fig. 95. A significant rising trend is observed for the "leading jet" events (red

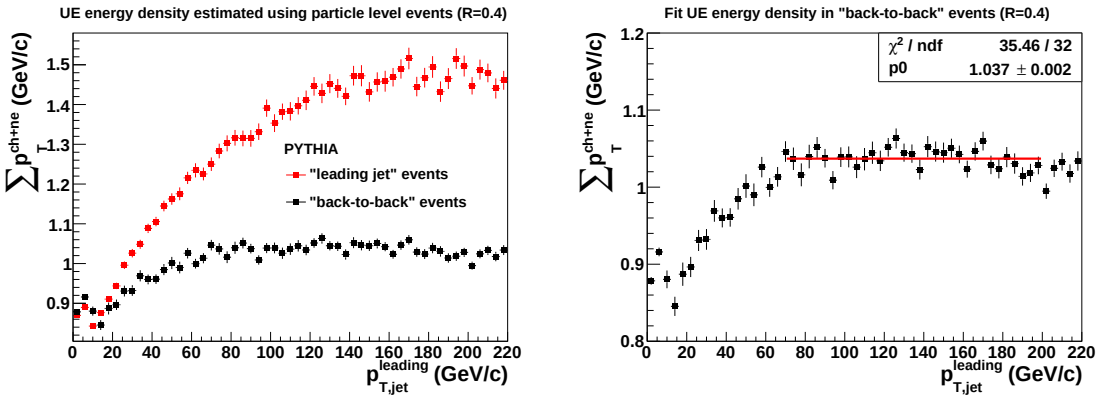

Figure 95: Left: UE density as a function of leading jet p_{T} in both "leading jet" and "back-to-back" events at particle level. Right: fit to the UE density in "back-to-back" events above 60 GeV/c.

points) in the full kinematic region, which indicates contributions from the hard scattering to the UE. The main sources are probably initial and final state radiations at large angles. On the contrary, the UE density in the "back-to-back" events (black points) saturates above 60 GeV/c, meaning the contribution of the hard scatterings is highly suppressed. Therefore, the UE density is better estimated using the "back-to-back" events as it is dominated by

interactions that are not related to the jet production. By fitting the saturation region of the UE density distribution as shown in the right panel of Fig. 95, the mean UE density is estimated to be about 2.08 GeV/c per unit area. Its contribution to the jet energy is corrected for at the particle level ($\mathrm{d}\sigma_{\mathrm{MC}}^{\mathrm{particle}}/\mathrm{d}p_{\mathrm{T}}$) by subtracting $2.08{*}A_{\mathrm{jet}}$ from jet p_{T}, where A_{jet} is the jet area. The effects of the UE subtraction on the particle-level jet spectrum are shown in Fig. 96 for $R = 0.2$ (left) and $R = 0.4$ (right) jets. The corrections are larger at low $p_{\mathrm{T,jet}}$ due to the $p_{\mathrm{T,jet}}$ independent UE density, and are larger for $R = 0.4$ jets due to the larger area.

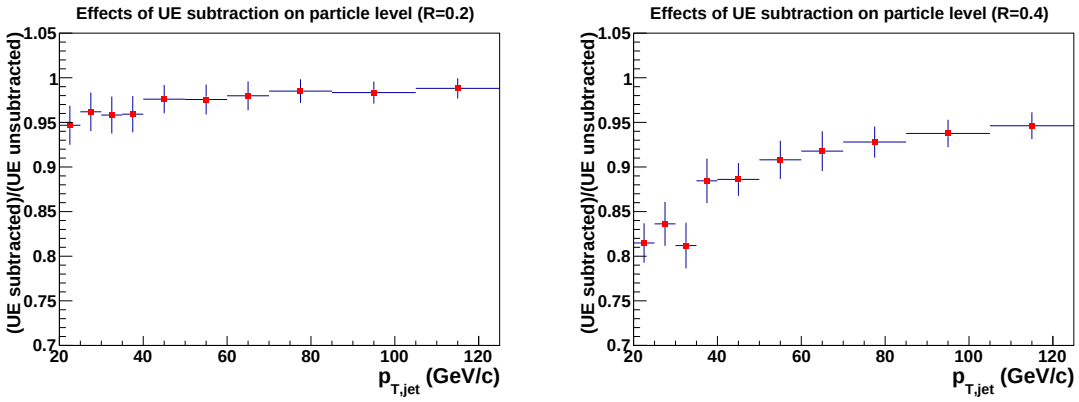

Figure 96: Effects of UE subtraction on the jet spectrum for $R = 0.2$ (left) and R =0.4 (right) jets at particle level.

An implicit assumption made in the above procedure of correcting the UE contribution is that the UE density in the data is correctly modeled in the detector-level simulation. To validate this assumption, we compare the charged UE density as a function of leading charged jet p_{T} in the "leading jet" events between data and detector-level simulation, as shown in the left panel of Fig. 97. This choice is made under the constraint of the limited EMCal acceptance and limited statistics in data. As illustrated by the ratio in the right panel, data and simulation are seen to agree within 20% in the kinematic reach of the data, which is then assigned as the systematic uncertainty of the UE density.

8.4 Acceptance Correction

Jets are measured in the EMCal acceptance (see Eq. 56), while the cross section is conventionally reported for mid-rapidity ($|\eta| < 0.5$) over full azimuth. Since the EMCal is located

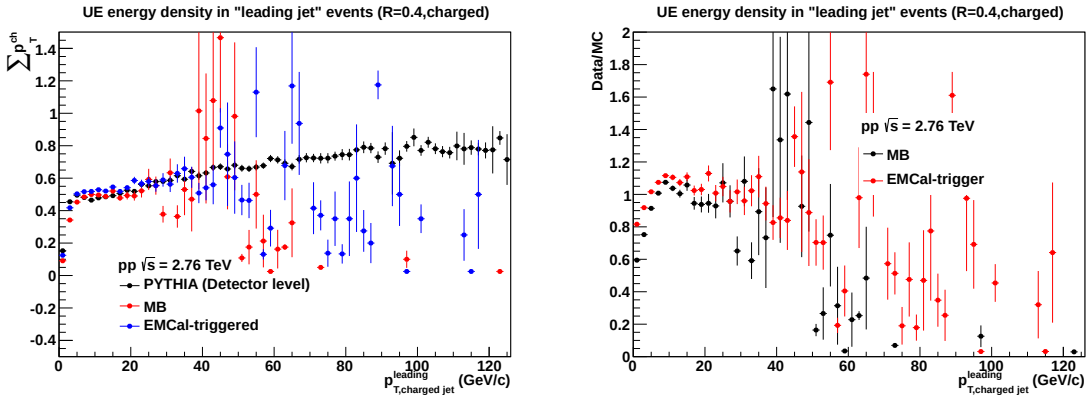

Figure 97: Left: charged UE density as a function of leading charged jet p_{T} in the "leading jet" events for MB data (red), EMCal-triggered data (blue) and detector-level simulation (black). Right: ratio of data to simulation.

at mid-rapidity, no efficiency change is expected going from the EMCal acceptance to the full phase space. Hence, the acceptance correction is simply calculated based on geometrical scaling:

$$A\left(p_{\mathrm{T}}\right)=\frac{(1.4-2R)\times(1.745-2R)}{2\pi} \tag{64}$$

where R is the jet radius.

8.5 Cross check via unfolding

An alternative way to correct for the detector effects is via unfolding, which is used to cross-check the results of the default bin-by-bin correction procedure. Specifically, the Bayesian unfolding [100] method is utilized as the following:

- Build response matrix from simulation, which is shown in Fig. 80.
- Get the raw jet yield from data, and correct the trigger bias on jets in EMCal-triggered data as described in section 7.2.
- Cut both response matrix (detector level jets) and raw yield at 10 GeV/c to suppress "fake" jets. The actual threshold can be determined via simulation by examining the ratio of the unmatched jets to the inclusive jets at detector level.
- Use the iterative Bayesian method implemented in the RooUnfold package for unfolding. The number of iterations is set to 4.

- Apply the jet-finding efficiency on the unfolded spectrum. It is determined from simulation as the ratio of particle-level jets that have matched detector-level jets above threshold (10 GeV/c) to the inclusive particle-level jets.

The resulting jet cross sections using both bin-by-bin and unfolding techniques are shown in Fig. 98 for $R = 0.4$ jets, and are consistent within the statistical errors. The same conclusion stands also for the $R = 0.2$ jets.

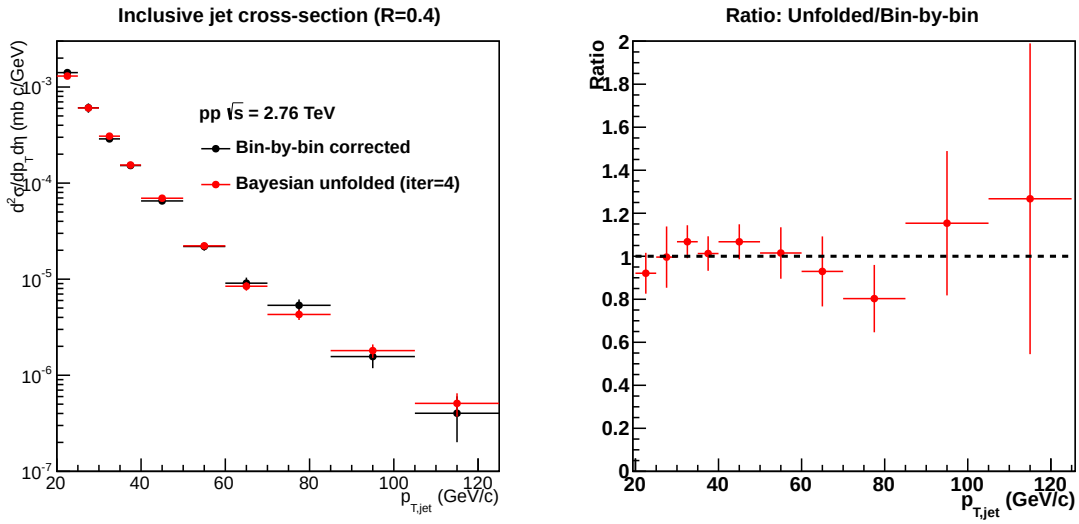

Figure 98: Left: comparison of jet cross section ($R = 0.4$) using bin-by-bin and unfolding techniques. Right: ratio of unfolded cross section to the bin-by-bin corrected one. Within the statistical errors, the results from the two methods are consistent.

9 Integrated luminosity

9.1 MB data

The integrated luminosity of the MB data sample can be calculated via:

$$L_{\text{int}} = \frac{N_{\text{MB}}^{10\text{ cm}}}{\sigma^{\text{MB}}} \tag{65}$$

$$= \frac{N_{\text{MB}}^{\text{vtx+10 cm}} \times \frac{N_{\text{MB}}^{10\text{ cm}}}{N_{\text{MB}}^{\text{vtx+10 cm}}}}{\sigma^{\text{MB}}} \tag{66}$$

$$= \frac{N_{\text{MB}}^{\text{vtx+10 cm}} \times \frac{N_{\text{MB}}}{N_{\text{MB}}^{\text{vtx}}}}{\sigma^{\text{MB}}} \tag{67}$$

where

- σ^{MB} is the MB trigger cross section, measured to be 55.4 ± 1.0 mb by a van der Meer scan [101].
- $N_{\text{MB}}^{10\text{ cm}}$ is the number of MB triggered events that have interaction vertices within $|z| < 10$ cm. A fraction of such events may not contain any reconstructed vertex. Since the $|z| < 10$ cm cut does not carry any cross section bias, the corresponding cross section for such events is still σ^{MB}, which is why Eq. 65 holds. However, this quantity cannot be directly measured in data.
- $N_{\text{MB}}^{\text{vtx+10 cm}}$ is the number of MB triggered events with reconstructed vertices within $|z| < 10$ cm
- $N_{\text{MB}}^{\text{vtx}}$ is the number of MB triggered events with reconstructed vertices.
- N_{MB} is the number of MB triggered events.
- The MB simulation shows that the z distributions of the interacting vertices for events with and without reconstructed vertices are almost identical, which leads to Eq. 67.

Plug in all the numbers:

$$L_{\text{int}} = \frac{2.665726 \times 10^7 \times \frac{3.316857 \times 10^7}{3.018114 \times 10^7}}{55.4} = \frac{2.665726 \times 10^7}{55.4 \times 0.91} = 0.5 \text{ nb}^{-1} \tag{68}$$

9.2 EMCal-triggered data

The integrated luminosity is calculated by referring to the MB process as:

$$L_{\text{int}} = \frac{N_{\text{event}}^{\text{triggered}} \times F_{\text{rejection}}}{\sigma^{\text{MB}} \times (N_{\text{MB}}^{\text{vtx}}/N_{\text{MB}})} \tag{69}$$

$F_{\text{rejection}}$ is the number of MB events to which a single EMCal-triggered event is equivalent. It is estimated to be 1246 ± 19 by fitting the cluster turn-on curve in the plateau region extracted from data, as shown in Fig. 99. The binning in Fig. 99 is chosen to be large to

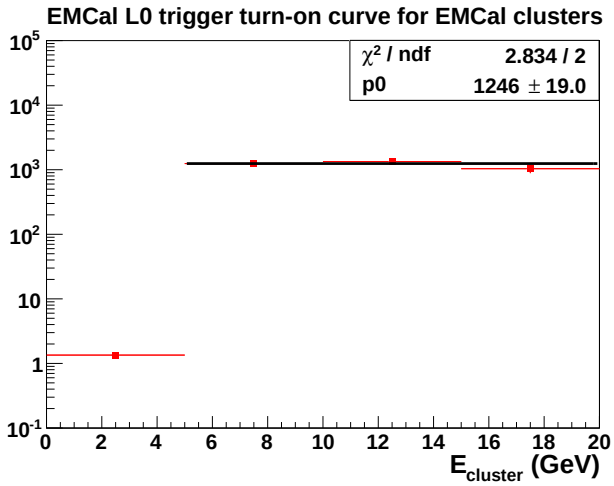

Figure 99: Determine the rejection factor of the EMCal trigger by fitting the trigger turn-on curve of the EMCal clusters from data.

avoid any significant statistical fluctuations at high energies.

Plugging in all the numbers gives:

$$L_{\text{int}} = \frac{5.302320 \times 10^5 \times 1246}{55.4 \times 0.91} = 13.1 \text{ nb}^{-1} \tag{70}$$

10 Systematic uncertainties

Systematic uncertainties arise from limited knowledge of the precise conditions under which the detectors are operated when the data was taken, and from the imperfection of the simulations for the physical processes under study. All components of the systematic uncertainties can be classified into two categories: (i) those affecting the JES, and (ii) those affecting the jet yield. The total uncertainty on the jet cross section is the quadratic sum of all the components.

A general feature that will be observed in the following sections is that in the highest $p_{\mathrm{T,jet}}$ bins where the number of entries is small, systematic variation of components of analysis cuts and algorithms can induce large fluctuations. This effect arises because the variations effectively change the reported p_{T} of each jet candidate, and the systematic variation in yield in the bin comes from the flow into and out of the bin at both its lower and upper bounds. However, if the bin contains only a few candidates, such bin-flow will be highly granular and dominated by the small statistics, and will not be representative of the systematic variation in the bin population at high statistics. In order to extract a representative systematic uncertainty, adjustment of the derived uncertainties may be needed by fitting or extrapolating from lower p_{T} bins. There is a degree of arbitrariness in this procedure, which varies for different sources of systematic uncertainties, but in general we aim to assign reasonably conservative values. In each subsection, the final systematic uncertainty is shown as the red lines, while the black and blue solid squares (if present) resemble the variation of the jet yield due to the variation of cuts or algorithms.

10.1 Systematic uncertainty of the JES

A given fractional variation of the JES corresponds to a fractional variation fives times larger in the jet yield due to the fact that the jet spectrum follows a power-law distribution of: $\mathrm{d}\sigma/\mathrm{dp_T} \sim \mathrm{p_T^{-5}}$. As all the uncertainties are shown for the jet yield, they can be converted to the uncertainty of the JES simply via being divided by 5.

10.1.1 Tracking efficiency

The correction for tracking efficiency relies on simulation, and the uncertainty comes from how accurately GEANT models the absolute tracking efficiency in real data. The effects of the tracking efficiency can be simply mimicked by throwing away randomly a fraction of tracks according to the normal value of the efficiency shown in Fig. 48 on the particle level. The systematic uncertainty is estimated by varying the tracking efficiency relative to its nominal value by ±5%. The corresponding variations of the particle-level spectrum give us an estimate of the systematic uncertainties, which are shown in Fig. 100 for $R = 0.2$ (left) and $R = 0.4$ (right) jets. Symmetric uncertainty is assigned by taking the larger of the two variations in each bin, which increases monotonically with jet p_{T} from ~ 9 (7)% at $p_{\mathrm{T,jet}} = 20$ GeV/c to ~ 13 (11)% at $p_{\mathrm{T,jet}} = 120$ GeV/c for $R = 0.4$ (0.2) jets.

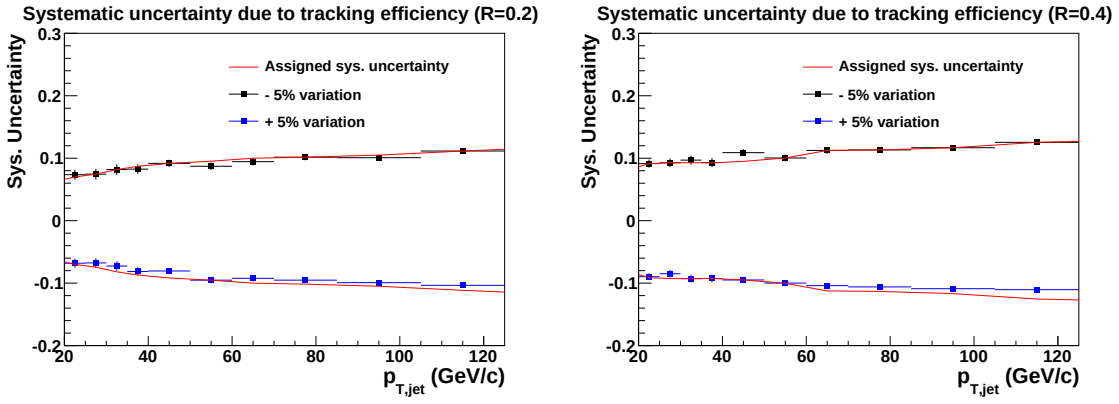

Figure 100: Systematic uncertainty of the inclusive jet spectrum due to uncertainty in GEANT modeling of the tracking efficiency for $R = 0.2$ (left) and $R = 0.4$ (right) jets as a function of jet p_{T}.

10.1.2 Hadronic correction

There are two main sources of systematic uncertainty in the procedure of correcting the charged energy deposition in the EMCal: (i) matching criteria used to associate tracks and clusters; and (ii) the fraction of charged track momentum subtracted from the cluster energy.

A track is matched to a cluster if the residuals meet the requirements: $|\Delta\eta| < 0.015, |\Delta\varphi| < 0.03$. These matching criteria are varied to be $|\Delta\eta| < 0.025, |\Delta\varphi| < 0.05$ in both real data

and MC detector level. The systematic uncertainty is assigned as the variation on the final cross section, shown in Fig. 101 for $R = 0.2$ (left) and $R = 0.4$ (right) jets, where an instance of large fluctuations at high $p_{\mathrm{T,jet}}$ emerges. With the help of the variations at lower $p_{\mathrm{T,jet}}$, where the statistical errors are small, the final uncertainty is determined to be 2% at low $p_{\mathrm{T,jet}}$ and 5% at high $p_{\mathrm{T,jet}}$.

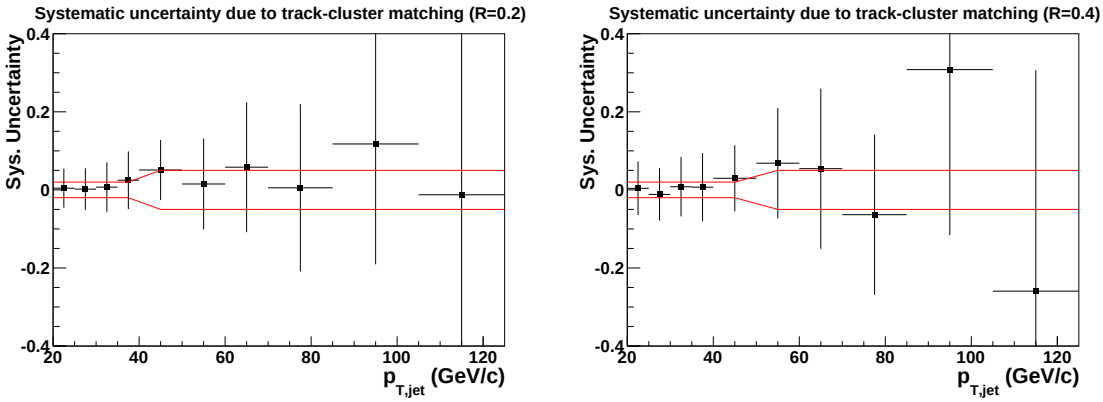

Figure 101: Systematic uncertainty of the inclusive jet spectrum due to the matching criteria for $R = 0.2$ (left) and $R = 0.4$ (right) jets as a function of jet p_{T}.

$f_{\mathrm{sub}} = 1$ is used as the default value to correct the charged energy double counting in the EMCal. To estimate the systematic uncertainty due to this choice, f_{sub} is changed to be 0.7 in both real data and MC detector level, and the entire analysis chain is repeated with the new value. The uncertainty comes from the variation of the final cross section, which is shown in Fig. 102 for $R = 0.2$ (left) and $R = 0.4$ (right) jets. The reassigned uncertainty is generally less than 6%.

10.1.3 Sensitivity to clustering algorithm

To estimate the sensitivity to the clustering algorithm choice, a different algorithm is utilized, which strictly limits the cluster size to be smaller than 9. The alternative algorithm is used in both data and simulation consistently, with the full correction scheme applied. The variation in the final cross section is taken as the systematic uncertainty, and Fig. 103 shows the result of this procedure for $R = 0.2$ (left) and $R = 0.4$ jets (right). Again, large and anti-correlated bin-to-bin excursions are seen, characteristic of the effects of small statistics in the high p_{T} bins. The anti-correlation arises because the total number of jets

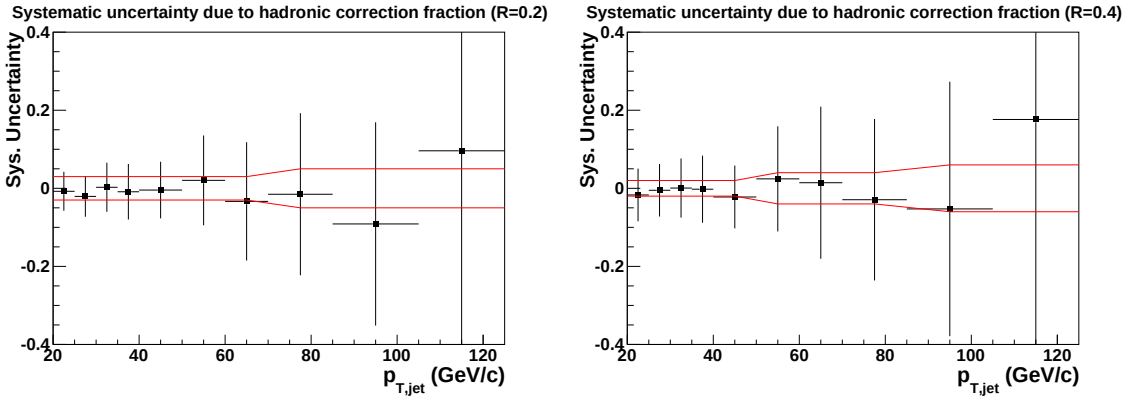

Figure 102: Systematic uncertainty of the inclusive jet spectrum due to the choice of $f_{\rm sub}$ value for hadronic energy correction for $R = 0.2$ (left) and $R = 0.4$ (right) jets as a function of jet $p_{\rm T}$.

is conserved, but the jet $p_{\rm T}$ for each candidate is varied by the change in algorithm. The reassigned uncertainty is 5% for both $R = 0.2$ and $R = 0.4$ jets across the full kinematic range.

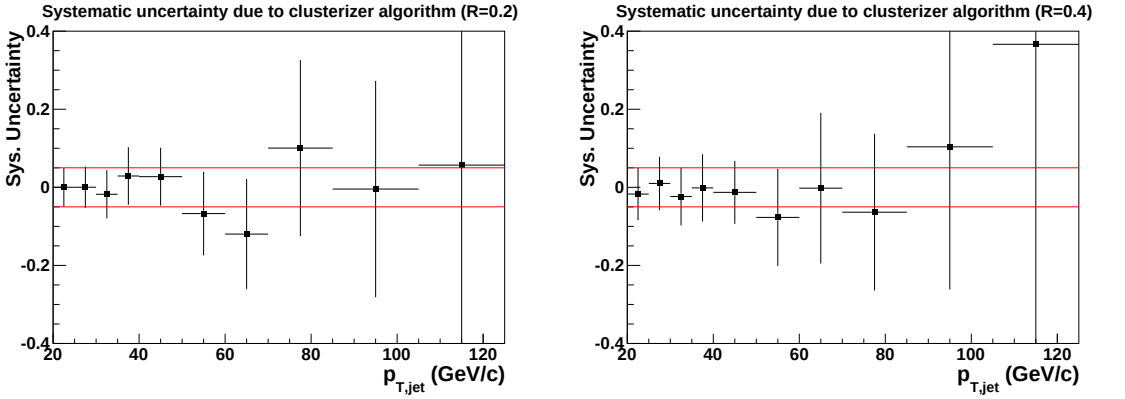

Figure 103: Systematic uncertainty of the inclusive jet spectrum due to the clustering algorithm for $R = 0.2$ (left) and $R = 0.4$ (right) jets as a function of jet $p_{\rm T}$.

10.1.4 EMCal energy scale

According to π^0 mass and electron E/p measurements using exactly the same data sets and simulations, a $\sim 2\%$ discrepancy between data and MC is observed as shown in Fig. 52, which is assigned as the uncertainty of the EMCal energy scale. To estimate the uncertainty on the final spectrum, we vary EMCal cluster energy by $\pm$ 2% in simulation, and look at the variation on the corrected spectrum, as shown in Fig. 104. The reassigned uncertainty

is 3% for $R = 0.2$ jets (left) and 4% for $R = 0.4$ jets (right) independent of $p_{\mathrm{T,jet}}$.

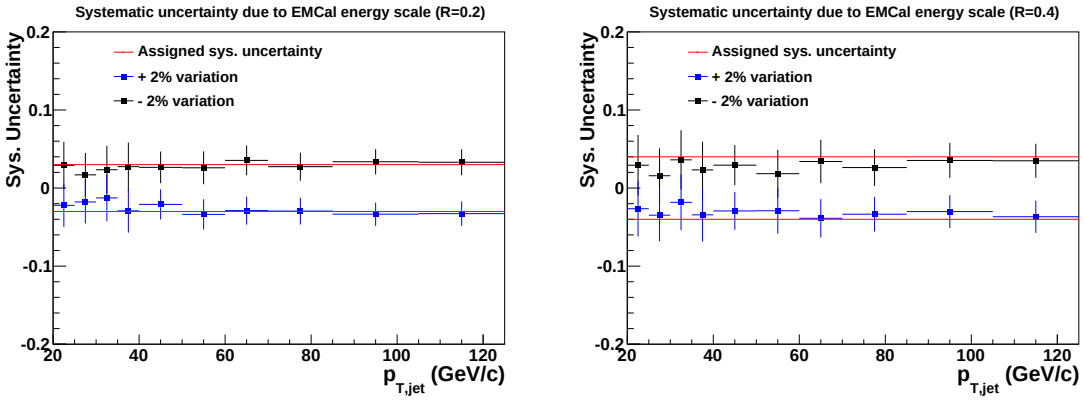

Figure 104: Systematic uncertainty of the inclusive jet spectrum due to EMCal energy scale uncertainty for $R = 0.2$ (left) and $R = 0.4$(right) jets as a function of jet p_{T}.

10.1.5 EMCal non-linearity

The uncertainty on the EMCal non-linearity correction is estimated by assuming that the EMCal has a uniform energy response in the data, and then observing the variation on the final spectrum. As shown in Fig. 105, the resulting uncertainty is less than 3% for both $R = 0.2$ and $R = 0.4$ jets.

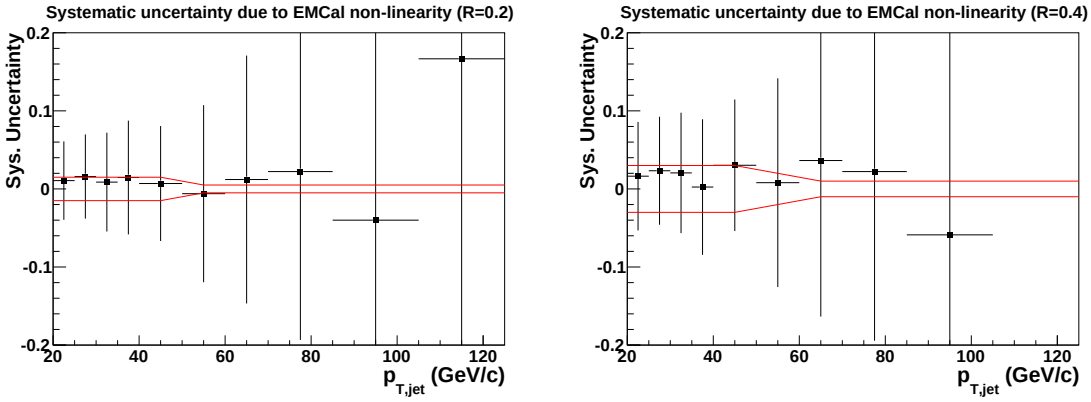

Figure 105: Systematic uncertainty of the inclusive jet spectrum due to the EMCal non-linearity correction for $R = 0.2$ (left) and $R = 0.4$(right) jets as a function of jet p_{T}.

10.1.6 Model dependence of fragmentation

A data-driven method is used to assess how accurately PYTHIA models jets fragmenting into charged tracks. This is done by discarding an additional 5% charged tracks in both data and detector-level simulation, recalculating $C_{\mathrm{MC}}\left(p_{\mathrm{T}}^{\mathrm{low}}; p_{\mathrm{T}}^{\mathrm{high}}\right)$ and the final corrected jet spectrum. The variation in the cross section is taken as the systematic uncertainty, which is assigned to be 5% across the board, as shown in Fig. 106 for $R = 0.2$ (left) and $R = 0.4$ (right) jets.

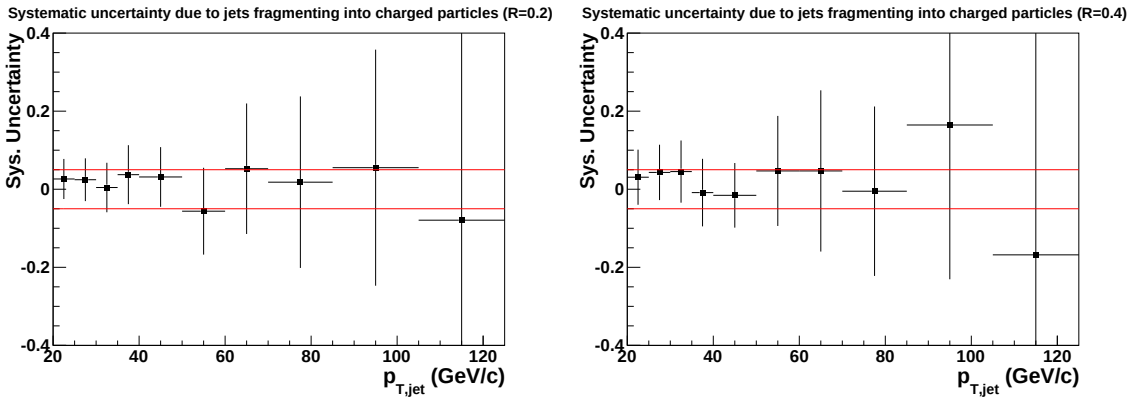

Figure 106: Systematic uncertainty of the inclusive jet spectrum due to PYTHIA modeling of jets fragmenting into charged particles, for $R = 0.2$ (left) and $R = 0.4$ (right) jets as a function of jet p_{T}.

A second source of uncertainty for the fragmentation model dependence is the relative abundance of quark and gluon-initiated jets in PYTHIA. While this concept is only meaningful at leading order, the distinction of quark and gluon jets can nevertheless be made in the model. Each particle-level jet from PYTHIA can be tagged according to the highest energy parton within its phase space, allowing C_{MC} to be calculated separately for quark and gluon-initiated jets. Since gluons tend to fragment into more particles with smaller p_{T} than quarks, the response matrices are different for jets initiated by quarks and gluons. PYTHIA estimates that gluon-initiated jets make up $\sim 70\%$ of the jet population, as shown in Fig. 107 for $R = 0.2$ (left) and $R = 0.4$ (right) jets. Assuming systematic uncertainty in the quark/gluon ratio of 10% relative to that in PYTHIA, the uncertainty in C_{MC} due to the different responses to quarks and gluons is estimated to be 5% in the full kinematic range. This is shown in Fig. 108 for $R = 0.2$ (left) and $R = 0.4$ (right) jets respectively.

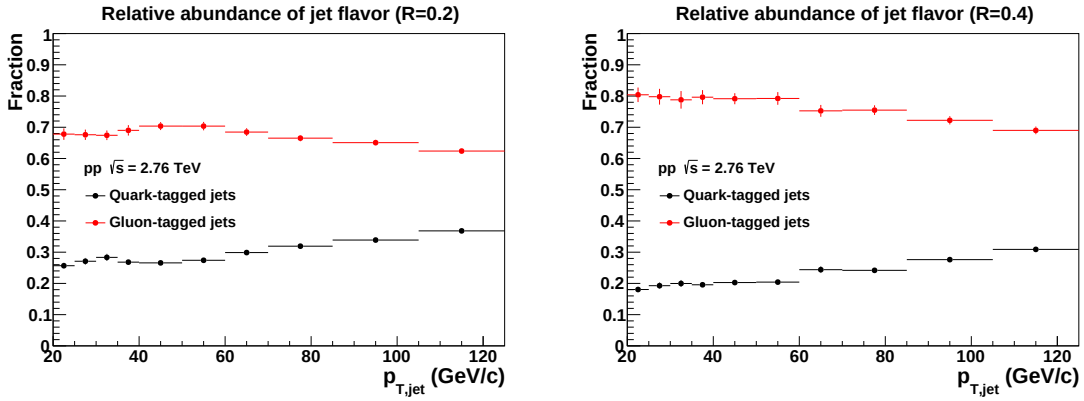

Figure 107: Relative abundance of gluon and quark initiated jets for $R = 0.2$ (left) and $R = 0.4$ (right) estimated by PYTHIA.

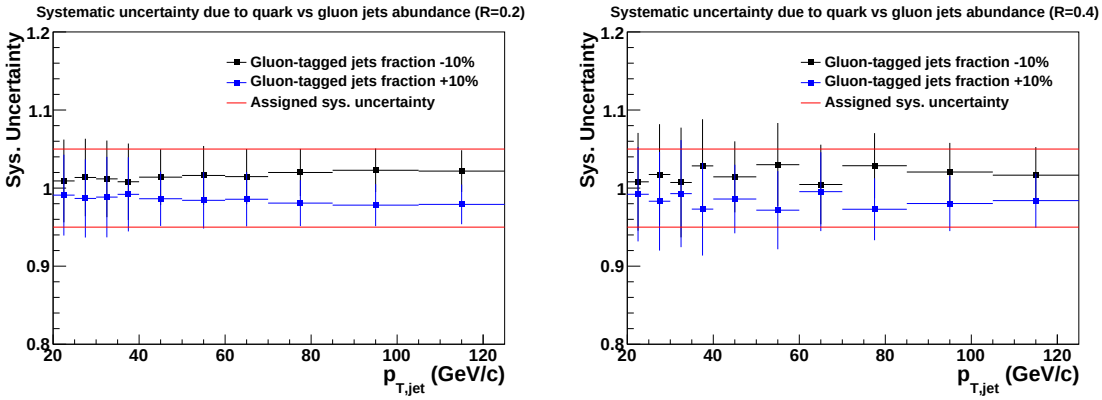

Figure 108: Systematic uncertainty of the inclusive jet spectrum due to PYTHIA modeling of the relative abundance of quark and gluon jets, for $R = 0.2$ (left) and $R = 0.4$ (right) jets as a function of jet p_{T}.

A third contribution comes from the comparison of PYTHIA to a different fragmentation model, HERWIG. This variation is assessed at the particle level by applying parametrized detector response:

- Exclude neutrons and K_L^0's.
- Assume 100% efficiency for photon measurements.
- Smear photon energy according to the energy resolution of EMCal estimated from the test beam data, shown in Fig. 38.
- Discard charged particles on a random basis according to the p_T-dependent tracking efficiency in Fig. 48.
- Smear p_T of the charged particles according to the p_T resolution estimated in data for charged tracks, shown in Fig. 49.

The difference in the bin-by-bin correction factors calculated from the two models incorporating parametrized detector response is assigned as the uncertainty, as shown in Fig. 109 for $R = 0.2$ (left) and $R = 0.4$ (right) jets. The large fluctuations come from the weighting procedure in the jet simulation. The uncertainty is assigned to be 5% over the entire range, for both jet radii.

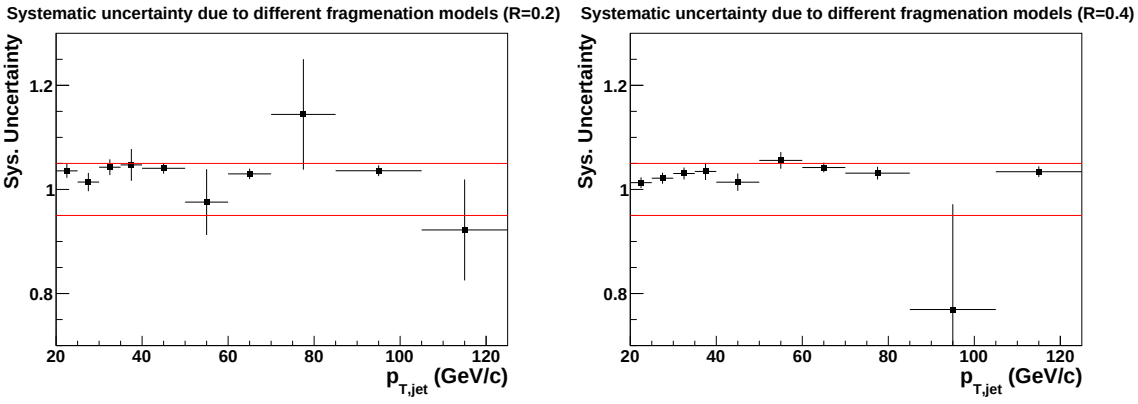

Figure 109: Systematic uncertainty of the inclusive jet spectrum due to different fragmentation models, for $R = 0.2$ (left) and $R = 0.4$ (right) jets as a function of jet p_T.

10.1.7 Correction for unmeasured neutrons and K_L^0's

The systematic uncertainty associated with the correction for unmeasured neutrons and K_L^0's is estimated by comparing calculations from PYTHIA and HERWIG, as shown in Fig. 110. It increases with jet p_T and is $\sim 3\%$ in the highest bin. This is actually part of the third

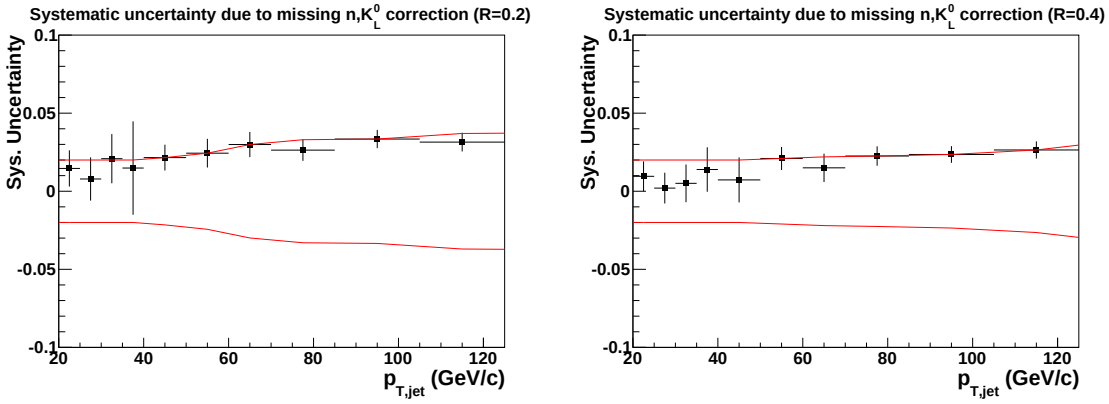

Figure 110: Systematic uncertainty for the correction of unmeasured neutrons and K_L^0's for $R = 0.2$ (left) and $R = 0.4$ (right) jets as a function of jet p_T, which is estimated by comparing PYTHIA and HERWIG.

component of the uncertainty due to the fragmentation model discussed in Section 10.1.6. But it is worth separating this aspect out to show that the uncertainty is well constrained, since a major criticism of jet measurements using an electromagnetic calorimeter without hadronic calorimetry is how well the correction for the missing energy of the neutrons and K_L^0's is under control.

10.1.8 UE subtraction

As discussed in section 8.3, the uncertainty of the UE density on the particle level is determined to be 20% which covers the discrepancy between data and simulation. The resulting variation on the particle-level spectrum with the 20% variation of the subtracted UE density is assigned as the systematic uncertainty, shown in Fig. 111. In general, the uncertainty decreases as jet p_T increases, and is much smaller for $R = 0.2$ than for $R = 0.4$, as expected.

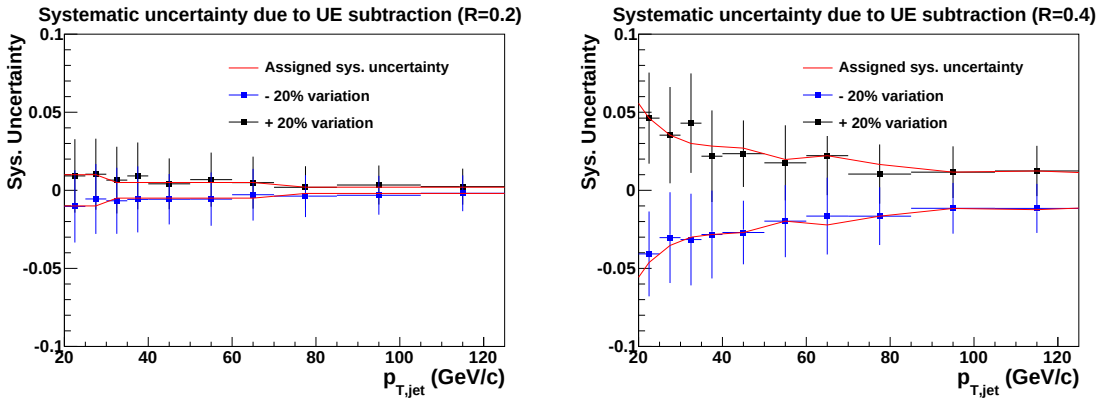

Figure 111: Systematic uncertainty of the inclusive jet spectrum due to the UE subtraction for $R = 0.2$ (left) and $R = 0.4$ (right) jets as a function of jet p_{T}.

10.2 Systematic uncertainty of the jet yield

10.2.1 Input spectrum shape

The bin-by-bin correction factor C_{MC} (Eq. 61) has an explicit dependence on the input spectrum shape, via $\mathrm{d}\sigma_{\mathrm{MC}}^{\mathrm{particle}}/\mathrm{d}p_{\mathrm{T}}$. A parametrization of the measured raw inclusive jet distribution $\frac{\mathrm{d}F_{\mathrm{meas}}^{\mathrm{uncorr}}}{\mathrm{d}p_{\mathrm{T}}}$ is used as a weight function to minimize such dependence. Nevertheless, there are still residual systematic uncertainties due to possible variations in the particle-level spectral shape, which are estimated as follows:

- Parametrize the default spectrum at particle level with a power law function.
- Vary the power index of the parametrization by ± 0.5, which covers the variation between different models. The overall normalization is irrelevant.
- Get the response matrix $R(p_{\mathrm{T,jet}}^{\mathrm{particle}}, p_{\mathrm{T,jet}}^{\mathrm{detector}})$ as shown in Fig. 80.
- Construct the jet spectrum at the detector level according to:

$$\mathrm{d}\sigma_{\mathrm{MC}}^{\mathrm{detector}}/\mathrm{d}p_{\mathrm{T}} = \int_0^{p_{\mathrm{T,jet,max}}^{\mathrm{particle}}} dp_{\mathrm{T,jet}}^{\mathrm{particle}} \frac{d\sigma}{dp_{\mathrm{T,jet}}^{\mathrm{particle}}} R(p_{\mathrm{T,jet}}^{\mathrm{particle}}, p_{\mathrm{T,jet}}^{\mathrm{detector}}), \tag{71}$$

  where $p_{\mathrm{T,jet,max}}^{\mathrm{particle}}$ is an arbitrary upper limit beyond the practical jet p_{T} reach for the statistics of the data set. It is set to 250 GeV/c.

- The systematic uncertainty is estimated by comparing the variation in the overall bin-by-bin correction factor $C_{\mathrm{MC}}\left(p_{\mathrm{T}}^{\mathrm{low}};p_{\mathrm{T}}^{\mathrm{high}}\right)$ with various choices of power for the input spectrum. Figure 112 shows the systematic uncertainties for $R = 0.2$ (left) and $R = 0.4$ (right) jets, which are $4-7\%$ with mild p_{T} dependence.

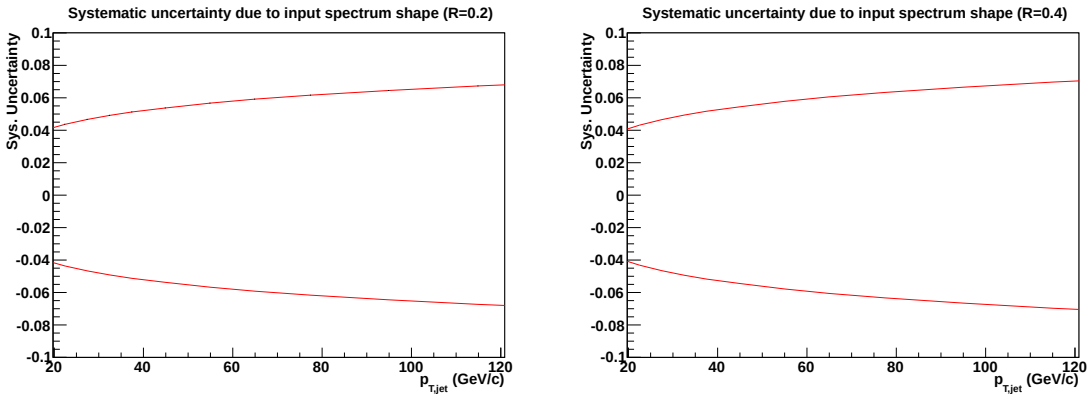

Figure 112: Systematic uncertainty on $C_{\mathrm{MC}}\left(p_{\mathrm{T}}^{\mathrm{low}};p_{\mathrm{T}}^{\mathrm{high}}\right)$ due to variation of input PYTHIA spectrum shape for $R = 0.2$ (left) and $R = 0.4$ (right) jets.

10.2.2 Trigger efficiency

There are four sources of uncertainties in the estimation of the trigger efficiency for jets: (i) the accuracy of GEANT modeling of electromagnetic showers, (ii) the accuracy of PYTHIA modeling of jet fragmentation into neutral particles, (iii) variation of online trigger threshold, and (iv) the relative scaling of SSh-triggered and MB cross sections.

The first type of uncertainty is estimated by comparing the trigger efficiency in data and simulation, as shown in the right panel of Fig. 73. However, this comparison is limited due to the statistical reach of the data. Therefore, a one-sided 10% uncertainty for the jet spectrum below 30 GeV/c is assigned in the triggered data.

The EMCal SSh trigger can be modeled at the particle level by assuming that an event is triggered if the event contains a photon (mainly from π^0 decays) in the EMCal acceptance with energy larger than 3 GeV. The second type of uncertainty is evaluated by comparing PYTHIA and HERWIG calculations of trigger turn-on curves at the particle level. As shown in Fig. 113, the uncertainty is 6% for $R = 0.2$ jets and 10% for $R = 0.4$ jets at 20 GeV/c, and is negligible above 70 GeV/c.

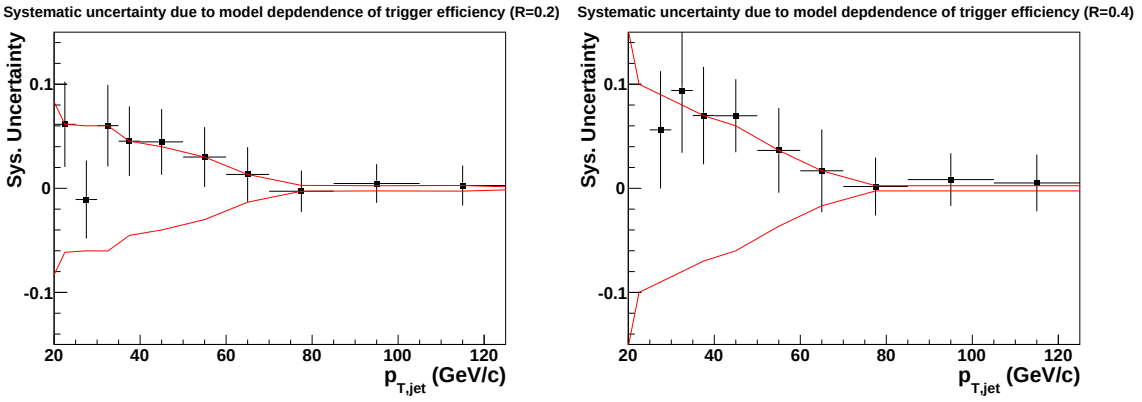

Figure 113: Systematic uncertainty of the inclusive jet spectrum due to the modeling of jet fragmentation into neutral particles for $R = 0.2$ (left) and $R = 0.4$ (right) jets as a function of jet p_{T}. Uncertainty is the difference between PYTHIA and HERWIG calculations at the particle level (see text).

The third source is assessed via varying the EMCal cluster energy in detector-level simulation by $\pm 2\%$, which is equivalent to a 2% uncertainty of the online trigger threshold, and looking at the variation of the trigger turn-on curves. As shown in Fig. 114, the uncertainty decreases as jet p_{T} increases, and is $\sim 3\%$ at the lowest p_{T} bin.

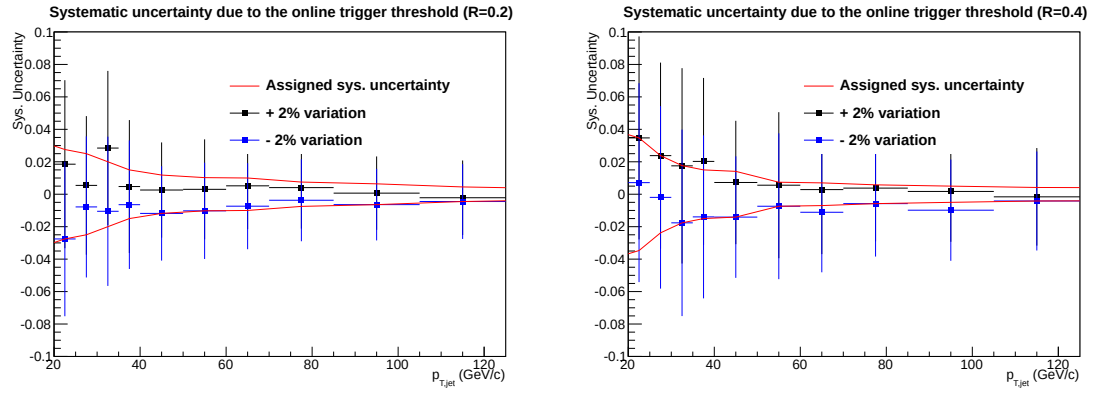

Figure 114: Systematic uncertainty of the inclusive jet spectrum due to the variations of the online threshold for $R = 0.2$ (left) and $R = 0.4$ (right) jets as a function of jet p_{T}.

The relative scaling of SSh-triggered and MB cross sections is:

$$S = \frac{F_{\mathrm{rejection}}}{A_{\mathrm{trigger}}} \tag{72}$$

where the uncertainties on $F_{\mathrm{rejection}}$ and A_{trigger} are 1.5% (see Fig. 99) and 0.4% (see Fig.

72) respectively, which results in a total of 1.55% uncertainty on the relative scaling factor.

10.2.3 Track p_{T} resolution

The p_{T} resolution of charged tracks is derived from the covariance matrix of the Kalman track model, and its uncertainty is estimated by the difference between data and simulation. To assess its effect on the inclusive jet spectrum, tracks are smeared at the MC detector level by an additional 50%, and the variation on the final cross section is taken as the uncertainty. Figure 115 shows that the uncertainty is 2% for $R = 0.2$ (left) jets and 3% for $R = 0.4$ (right) jets.

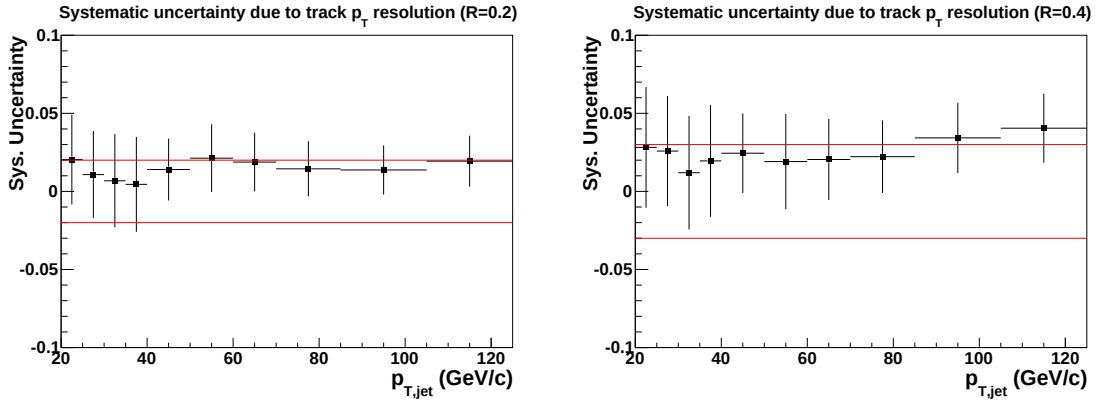

Figure 115: Systematic uncertainty of the inclusive jet spectrum due to track p_{T} resolution for $R = 0.2$ (left) and $R = 0.4$ (right) jets as a function of jet p_{T}.

10.2.4 EMCal energy resolution

The uncertainty of EMCal energy resolution is estimated to be $\sim 10\%$ based on the comparison of the π^0 and electron E/p analyses between data and simulation. The corresponding uncertainty on the final spectrum is evaluated via smearing the cluster energy in simulation by an additional 10%, and the results are shown in Fig. 116, where 1% uncertainty for both $R = 0.2$ and $R = 0.4$ jets is assigned.

10.2.5 Cross section normalization

The uncertainty on the MB cross section is determined to be 1.9% by a van der Meer scan [101].

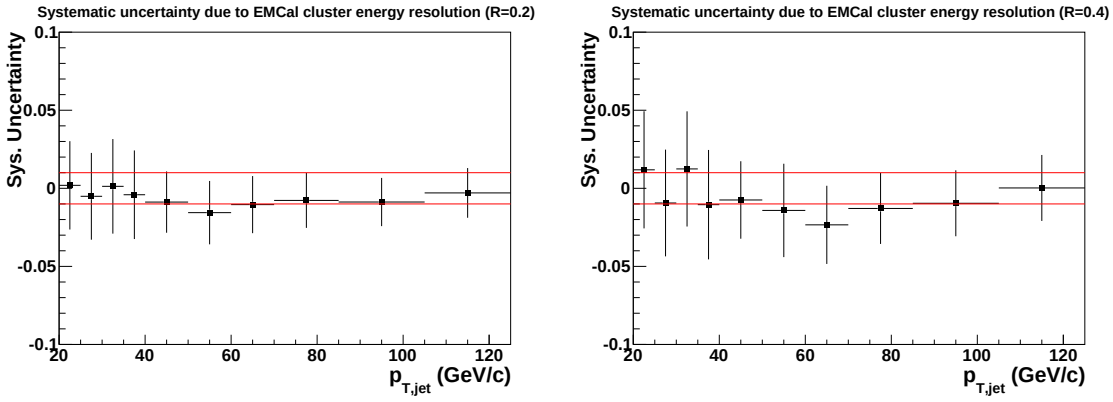

Figure 116: Systematic uncertainty of the inclusive jet spectrum due to EMCal energy resolution for $R = 0.2$ (left) and $R = 0.4$(right) jets as a function of jet p_{T}.

10.3 Total uncertainty

All the components of the systematic uncertainties, discussed in the previous two subsections, are summarized in Table 2 for two representative jet p_{T} bins at 25 GeV/c and 100 GeV/c. Systematic uncertainties at different p_{T} are largely correlated. The components are added in quadrature to generate the total uncertainty.

Table 2: Systematic uncertainties of the jet cross section measurements. Data at 25 GeV/c are from the MB data set, whereas data at 100 GeV/c are from the EMCal-triggered data set.

Source of systematic uncertainty	Jets $R = 0.2$		Jets $R = 0.4$	
	25 GeV/c	100 GeV/c	25 GeV/c	100 GeV/c
Tracking efficiency	7%	10.5%	9.1%	11.7%
Momentum scale of charged tracks	negligible	negligible	negligible	negligible
Charged hadron showering in EMCal	3.6%	7.1%	2.8%	7.8%
Energy scale of EMCal cluster	3%	3%	4%	4%
EMCal non-linearity	1.5%	negligible	3%	negligible
EMCal clustering algorithm	5%	5%	5%	5%
Underlying event	1%	negligible	4.8%	1.3%
Fragmentation model dependence	8.7%	8.7%	8.7%	8.7%
Input PYTHIA6 spectrum shape	4%	6%	4%	7%
Momentum resolution of charged track	2%	2%	3%	3%
Energy resolution of EMCal cluster	1%	1%	1%	1%
EMCal-SSh trigger efficiency	none	1.7%	none	1.8%
Cross section normalization	1.9%	1.9%	1.9%	1.9%
Spectrum total systematic uncertainty	14%	18%	16%	20%

11 Corrected pp jet cross section

In order to limit the sensitivity to the large systematic uncertainty of the EMCal trigger efficiency at low $p_{\mathrm{T,jet}}$ (section 10.2.2), MB data are used for $p_{\mathrm{T}} < 30$ GeV/c, whereas EMCal-triggered data are used for $p_{\mathrm{T}} > 30$ GeV/c in constructing the final jet cross section.

11.1 Comparison to pQCD calculations

Figure 117 shows the inclusive differential jet cross section corrected to particle level at mid-rapidity for resolution parameters $R = 0.2$ (left) and $R = 0.4$ (right) in pp collisions at $\sqrt{s} = 2.76$ TeV. The data points are the black squares, spanning over four orders of magnitude. The error bars and black boxes around the data points are statistical errors and systematic uncertainties, respectively.

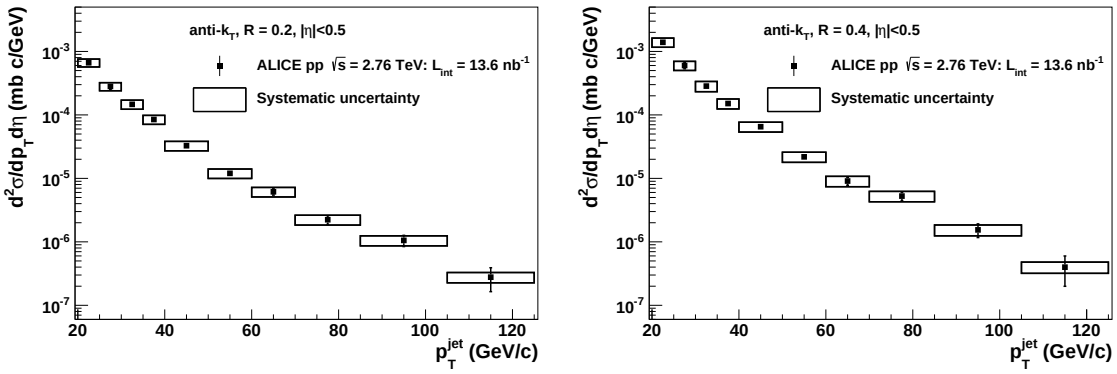

Figure 117: Inclusive differential jet cross sections for $R = 0.2$ (left) and $R = 0.4$ (right). Vertical bars show the statistical error, while boxes show the systematic uncertainty. Data points are placed at the center of each bin.

Results of Next-to-Leading Order (NLO) pQCD calculations at different levels of parton shower are shown in Fig. 118 for comparison. The Armesto calculation [102, 103, 104] is carried out at the parton level using MSTW08 PDF [105]. The Soyez calculation utilizes CTEQ6.6 PDFs [106] and is carried out at both the partonic and hadronic levels [107]. The bands indicate the theoretical uncertainty estimated by varying the renormalization and factorization scales between 0.5 p_{T} and 2.0 p_{T}. The middle panels of Fig. 118 show the ratio of the NLO pQCD calculations at partonic level to data. This comparison has to be interpreted with care since the hadronization process is *only* present in data, which tends to

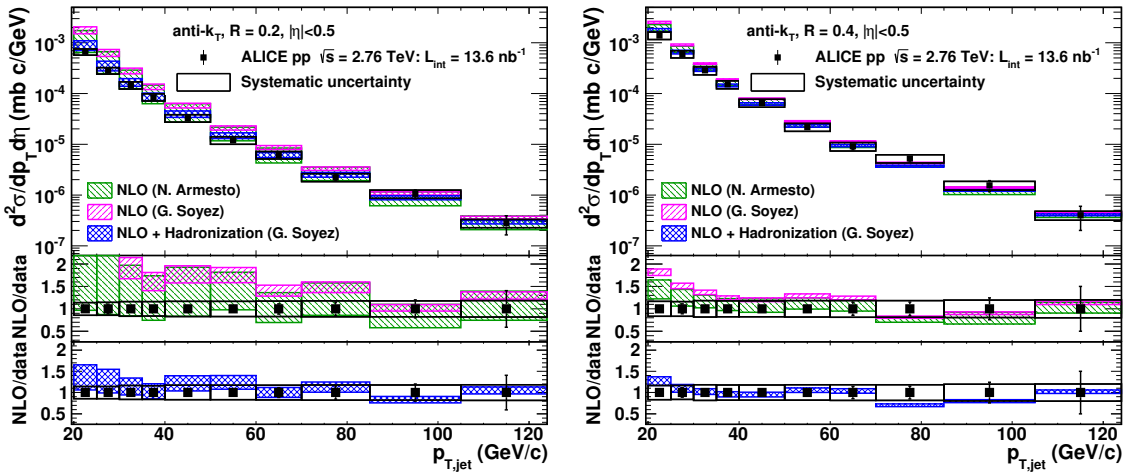

Figure 118: Upper panels: inclusive differential jet cross sections for $R = 0.2$ (left) and $R = 0.4$ (right). The bands show the NLO pQCD calculations discussed in the text [104, 107]. Lower panels: ratio of NLO pQCD calculations to data. Data points are placed at the center of each bin.

spread out the parton fragments via gluon bremsstrahlung. Therefore, the jet cross section at a fixed p_{T} is expected to be larger at the parton level than at the particle level, and the difference becomes smaller for larger cone radius and higher jet p_{T} ("jet collimation"). This is confirmed in the middle panels where the pQCD calculations overshoot data at low p_{T}, but reproduce data reasonably well at high p_{T}. Furthermore, the deviations at low p_{T} are larger for $R = 0.2$ (left) than for $R = 0.4$ (right) jets. Interestingly, the systematic uncertainties on the theoretical calculations increase as jet p_{T} decreases, mainly due to the increasing uncertainty associated with the PDFs at low x. On the contrary, the systematic uncertainties on data increase mildly as jet p_{T} increases, driven by the increasing uncertainty on the jet energy scale. By including the hadronization effects, parametrized as a fixed downward shift on parton-level jet p_{T}, the agreement between theoretical calculations and data is restored at low p_{T} for both $R = 0.2$ and $R = 0.4$ jets as shown in the bottom panels of Fig. 118.

The current measurement validates the state-of-the-art pQCD calculations at NLO, confirming that hard probes are indeed well understood in fundamental theories. It also nicely fills the gap for jet cross section measurements done at lower ($\sqrt{s}$= 1.96 TeV) and higher ($\sqrt{s}$= 7 TeV) energies [108, 109, 59, 60]. More importantly, the measurement serves

as a reference for a similar measurement in the Pb–Pb collisions, where jet R_{AA} is extracted as a function of jet p_{T} for 0-10% most central collisions [110]. It puts a constraint on any models describing parton energy loss in the QGP.

11.2 Jet cross section ratio

The ratio of jet cross sections for different jet resolutions is defined as:

$$\mathcal{R}(p_{\mathrm{T}}; R_1, R_2) = \frac{d\sigma(R = R_1)/p_{\mathrm{T,jet}}}{d\sigma(R = R_2)/p_{\mathrm{T,jet}}} \tag{73}$$

which probes the transverse structure of jets. In this analysis, $R_1 = 0.2$ and $R_2 = 0.4$ are chosen, and the result is shown in Fig. 119. A full covariant matrix has to be calculated and reported if the entire data set were used for both numerator and denominator, which is highly non-trivial. For simplicity, the numerator and denominator of the ratio are built using disjoint subsets of the data, to ensure that they are statistically independent. The kinematic reach of this measurement is therefore less than that of the inclusive spectra themselves as shown in Fig. 118. The systematic uncertainties of the ratio are estimated by directly measuring the variations on the ratio itself with respect to each contribution discussed in Chapter 10. For the uncertainties that are common or highly correlated in the inclusive spectra, for instance, tracking efficiency, trigger efficiency, normalization, etc, their contribution to the ratio is largely reduced. The total uncertainties are 8%, as listed in Table 3, for two representative jet p_{T} bins, which are much smaller than the $\sim$ 20% uncertainties on the individual cross sections at corresponding p_{T}. Therefore, the ratio allows a more stringent comparison of data and calculations than the individual inclusive cross sections.

The figure also shows parton-level pQCD calculations at Leading-Order (LO), NLO and NLO with hadronization correction [107]. The calculation considers the ratio directly, rather than each distribution separately, making the calculated ratio effectively one perturbative order higher than the individual cross sections (e.g. the curve labelled "NLO" is effectively NNLO). By going to higher orders or including the hadronization process, the ratio decreases at a fixed p_{T}, suggesting that both effects tend to move part of the parton energy out of

Table 3: Systematic uncertainties of the jet cross section ratio. Data at 25 GeV/c are from the MB data set, whereas data at 100 GeV/c are from the EMCal-triggered data set.

Source of systematic uncertainty	25 GeV/c	100 GeV/c
Tracking efficiency	1.5%	1.5%
Momentum scale of charged tracks	negligible	negligible
Charged hadron showering in EMCal	2.8%	4.5%
Energy scale of EMCal cluster	1.0%	1.0%
EMCal non-linearity	1.0%	negligible
EMCal clustering algorithm	3.0%	3.0%
Underlying event	3.7%	0.9%
Fragmentation model dependence	5.2%	5.2%
Input PYTHIA6 spectrum shape	negligible	negligible
Momentum resolution of charged track	2%	2%
Energy resolution of EMCal cluster	1%	1%
EMCal-SSh trigger efficiency	negligible	negligible
Cross section normalization	none	none
Total systematic uncertainty	8%	8%

the jet cone, and the influence is more significant for a smaller cone radius than a larger one. The NLO calculation of the ratio agrees within uncertainties with the measurement if hadronization effects are taken into account, indicating that the distribution of radiation within the jet is well-described by the calculation. Also shown in the figure is a predication from the PYTHIA model, which overlaps with the data very nicely. Even though only the LO matrix is included in PYTHIA, the implemented partonic shower mimics the higher order effects quite well.

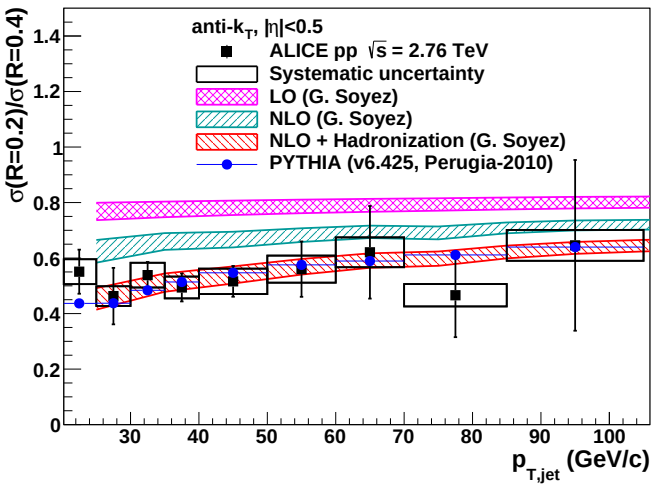

Figure 119: Ratio of inclusive jet cross sections for $R = 0.2$ and $R = 0.4$, with pQCD calculations and PYTHIA predication. Data points are placed at the center of each bin.

The cross section ratio presented here can be applied in the study of jet quenching in heavy-ion collisions.

12 Hadron-jet coincidence measurements in Pb–Pb collisions

12.1 Motivation

Jet reconstruction has been proven to work well in the elementary pp collisions as elaborated in Chapters 5 to 11. However, it is not transparent to directly transfer the analysis strategy employed in pp collisions to Pb–Pb collisions due to the large underlying background. As shown in Fig. 4, the charged particle multiplicity at mid-rapidity is about 1600, most of which are from soft processes, thus comprising background. On the other hand, the jet-finding algorithm has no *a prior* knowledge about whether a track is from a hard jet or background. It simply takes all the charged tracks in the event and groups them into jet candidates according to their positions in phase space. Therefore, we can symbolically write the components of the charged jet candidates as:

$$p_{\mathrm{T,jet}}^{\mathrm{ch}} = \sum_{\mathrm{jet}} p_{\mathrm{T,h}}^{\mathrm{ch}} + \sum_{\mathrm{bkg}} p_{\mathrm{T,h}}^{\mathrm{ch}} \tag{74}$$

where $\sum_{\mathrm{jet}} p_{\mathrm{T,h}}^{\mathrm{ch}}$ is the contribution of charged tracks from true hard jets, and $\sum_{\mathrm{bkg}} p_{\mathrm{T,h}}^{\mathrm{ch}}$ is from background tracks. Distortions to the true jet energies are present in heavy-ion collisions due to the background, which have to be accounted for in order to extract physics messages:

- $\sum_{\mathrm{bkg}} p_{\mathrm{T,h}}^{\mathrm{ch}} > 0$: true jet p_{T} is shifted
- $\sum_{\mathrm{bkg}} p_{\mathrm{T,h}}^{\mathrm{ch}}$ varies: true jet p_{T} is smeared
- $\sum_{\mathrm{jet}} p_{\mathrm{T,h}}^{\mathrm{ch}} = 0$: these jet candidates consist of only particles from incoherent soft processes (combinatorial jets), and thus contaminate the true jet population.

Background density: the average background contribution to the jet energy is corrected on an event-wise basis:

$$p_{\mathrm{T,ch\ jet}}^{\mathrm{corr}} = p_{\mathrm{T,jet}}^{\mathrm{ch}} - \langle \sum_{\mathrm{bkg}} p_{\mathrm{T,h}}^{\mathrm{ch}} \rangle = p_{\mathrm{T,jet}}^{\mathrm{ch}} - \rho \cdot A_{\mathrm{jet}} \tag{75}$$

where $A_{\rm jet}$ is the jet area, and ρ is the average background energy density of the event. The standard FastJet procedure to calculate ρ is to reconstruct the same event using the $\rm k_T$ algorithm and to equate ρ to the median of the distribution of jet $p_{\rm T}$ over area, for all jets, except the two leading ones, in the event [111]:

$$\rho = median\{\frac{p^i_{\rm T,jet}}{A^i_{\rm jet}}\} \tag{76}$$

where $p^i_{\rm T,jet}$ and $A^i_{\rm jet}$ are the $p_{\rm T}$ and area of the $i^{\rm th}$ $\rm k_T$ jet in the event. Since ρ is the *median* energy density of the event, there are necessarily regions in the event where the background density is less than ρ. If such a region does not contain an energetic hard jet, then with significant probability $p^{\rm corr}_{\rm T,ch\ jet} < 0$. As the area of the jets reconstructed using the anti-$k_{\rm T}$ algorithm does not vary significantly within the jet population [112], there are approximately half of the reconstructed jet candidates having $p^{\rm corr}_{\rm T,ch\ jet} < 0$, which are dominated by the combinatorial jets.

Background fluctuations: since the background contribution is corrected on average, the remaining region-to-region fluctuations smear the jet energies, which is quantified as the $\delta p_{\rm T}$ distribution:

$$\delta p_{\rm T} = \sum_{\rm bkg} p^{\rm ch}_{\rm T,h} - \langle \sum_{\rm bkg} p^{\rm ch}_{\rm T,h} \rangle \tag{77}$$

It can be extracted using a Random Cone (RC) technique [113], namely placing a rigid cone of same radius (R) as the signal jets randomly in real Pb–Pb events. $\delta p_{\rm T}$ is extracted by taking the difference between the sum of $p_{\rm T}$ of all the particles within the cone and the expected mean background energy:

$$\delta p_{\rm T} = \sum_{\rm cone} p^{\rm ch}_{\rm T,h} - \rho \cdot \pi R^2 \tag{78}$$

The $\delta p_{\rm T}$ distribution is then used to unfold the raw spectrum to correct for background smearing.

Combinatorial jets: given that the rate of the combinatorial jets is much greater than that of the true hard jets, an attempt to measure the hard jet distribution by unfolding background fluctuations without prior removal of the combinatorial jets is not a mathe-

matically well-posed problem, leading to unstable and wildly incorrect results [36]. There have been some proposals to overcome this issue by either requiring signal jets to contain high p_{T} constituents, or excluding jets below a certain p_{T} threshold [114], or removing the average background prior to jet finding [115]. However, all these strategies involve either specific fragmentation biases in jet population or limiting the kinematic range. This motivates the "h+jet" coincidence measurement, in which the combinatorial jets are removed on an ensemble basis [36]. The configuration for the h+jet coincidence is illustrated in the left panel of Fig. 120, where high p_{T} charged tracks are used as triggers. Such a high p_{T} hadron trigger effectively isolates a single hard partonic interaction (i.e. high Q^2 process) in the event. We then want to measure the properties of the recoil jets generated in the same interaction, i.e. the jet population in coincidence with the hadron trigger. To illustrate how the combinatorial jets are removed, we turn to the semi-inclusive differential p_{T} distribution of jets in the recoil azimuth $|\varphi_{\mathrm{trig}} - \varphi_{\mathrm{ch,jet}} - \pi| < 0.6$, normalized by the number of trigger tracks, as shown in the right panel of Fig. 120 for two exclusive Trigger Track (TT) p_{T} intervals. The spectrum at $p_{\mathrm{T,ch\ jet}}^{\mathrm{corr}} < 0$ is dominated by the combinatorial jets

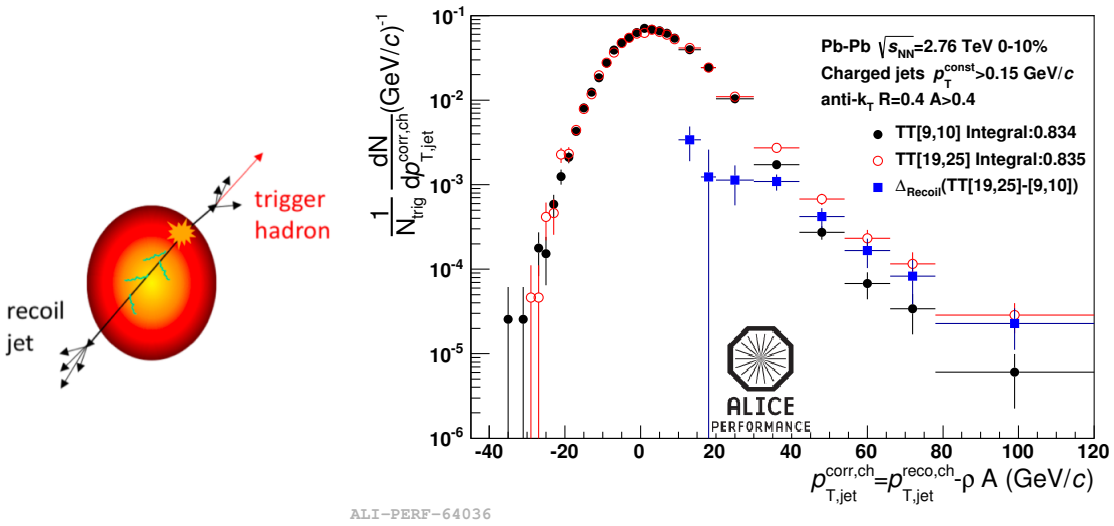

Figure 120: Left: "h+jet" configuration. Right: p_{T} distribution of jets recoiling from two distinct trigger p_{T} intervals: $9 < \mathrm{TT} < 10$ GeV/c (black) and $19 < \mathrm{TT} < 25$ GeV/c (red), in 0-10% most central Pb–Pb collisions. The difference of the red and black spectra is shown as the blue squares.

since the average background density is already subtracted. As the combinatorial jets are

created from incoherent interactions other than the hard scattering producing the trigger track, they should be *uncorrelated* to the trigger track. This is confirmed by the fact that the two spectra match each other nicely in the $p_{\mathrm{T,ch\ jet}}^{\mathrm{corr}} < 0$ region. The combinatorial jets can therefore be removed by subtracting the recoil jet spectrum for the lower p_{T} triggers ("reference") from that for the higher p_{T} triggers ("signal"). Inevitably, part of the true jet signal is also subtracted away, which renders the resulting distribution an evolution from lower to higher p_{T} triggers. In this thesis, we will focus on the azimuthal correlation between trigger tracks and recoil jets to address the question if jets are deflected further in the medium compared to in the vacuum, since jet quenching may induce acoplanarity in a jet pair, resulting in a broadening in the azimuthal correlation.

12.2 Azimuthal correlation from data

The observable under study is the difference azimuthal correlation, defined as:

$$\Delta_{\mathrm{recoil}}(\Delta\varphi) = (\frac{1}{N_{\mathrm{trig}}}\frac{\mathrm{d}N}{\mathrm{d}\Delta\varphi})_{\mathrm{signal}} - (\frac{1}{N_{\mathrm{trig}}}\frac{\mathrm{d}N}{\mathrm{d}\Delta\varphi})_{\mathrm{reference}} \tag{79}$$

where $\frac{1}{N_{\mathrm{trig}}}\frac{\mathrm{d}N}{\mathrm{d}\Delta\varphi}$ is the azimuthal correlation between the trigger tracks and recoil jets, normalized by the number of triggers. The subtraction between signal and reference triggers is to remove the uncorrelated background contribution. Two signal and reference trigger intervals are used: $16 < \mathrm{TT}_{\mathrm{sig}} < 19$ GeV/c, $19 < \mathrm{TT}_{\mathrm{sig}} < 25$ GeV/c, and $8 < \mathrm{TT}_{\mathrm{ref}} < 9$ GeV/c, $9 < \mathrm{TT}_{\mathrm{ref}} < 10$ GeV/c, to perform two independent measurements. The trigger p_{T} for both signal and reference classes is chosen to be high with the following considerations:

- Geometrical considerations of quenched jet production [116] indicate that high p_{T} hadrons tend to come from jets generated at the surface of the collision geometry and heading outward. The recoil jets are therefore biased towards larger path length in medium than the fully inclusive jet population.

- The bias induced in centrality and reaction plane orientation by the signal and reference triggers should be similar, which thereby is removed by taking the difference.

In total, 64 Pb–Pb runs[17] taken in 2010 are used for the analysis. In 36 runs ("SEMI-GOOD"), a TPC sector (IRCO13) was off during data taking, causing non-uniformity in azimuth for reconstructed charged tracks. The remaining 28 runs ("GOOD") have uniform tracking efficiency in azimuth. Only the 0-10% most central Pb–Pb collisions are used for analysis. Since both signal and reference triggers can appear in the same event, the entire data set is divided into two exclusive sub-sets, for building correlations in signal and reference classes separately in order not to double-count jets. 80% of the statistics is assigned to the signal class in order to maximize the total number of available signal triggers due to its lower production rate, and 20% of the statistics is used for the reference class to maintain sufficient statistical precision in estimating the combinatorial jet distribution. If more than one trigger shows up in an event, only one is chosen randomly to avoid, again, double-counting jets.

Only charged tracks are used for jet reconstruction since the statistics will be largely reduced if neutral particles measured in the small acceptance EMCal are included. The same track quality cuts as for the pp analysis (see Chapter 6.2) are used except that all the accepted tracks are required to contain at least three hits in the ITS.

The anti-k_{T} algorithm is used to reconstruct jets with radius of $R = 0.4$, by using all the selected charged tracks within $|\eta| < 0.9$. Jet candidates are only accepted if their centroid lies within $|\eta| < 0.5$. The average background for each event is also estimated using only charged tracks, and is subtracted for all the jet candidates in the event. The mean ρ in the 0-10% central Pb–Pb collisions is about 110 GeV/c per area. An additional cut of $40 < p_{\mathrm{T,ch\ jet}}^{\mathrm{corr}} < 60$ GeV/c on the recoil jet population is used to maximize the signal-to-background ratio while retaining sufficient statistics. The resulting azimuthal correlations between trigger tracks and recoil jets are shown in Fig. 121 for all four trigger classes. The yield of the distributions depends strongly on the trigger p_{T}, indicating that higher p_{T} triggers sample on average higher Q^2 processes, and thus have larger yield for the recoil

[17]Run list: 168311, 168322, 168325, 168341, 168361, 168362, 168458, 168460, 168461, 168992, 169091,169094, 169138, 169143, 169167, 169417, 169835, 169837, 169838, 169846, 169855, 169858, 169859, 169923, 169956, 170027, 170036, 170081, 167813, 167988, 168066, 168068, 168069, 168076, 168104, 168212, 169975, 169981, 170038, 170040, 170083, 170084, 170085, 170088, 170089, 170091, 170152, 170155, 170159, 170163, 170193, 170195, 170203, 170204, 170205, 170228, 170230, 170264, 170268, 170269, 170270, 170306, 170308, 170309

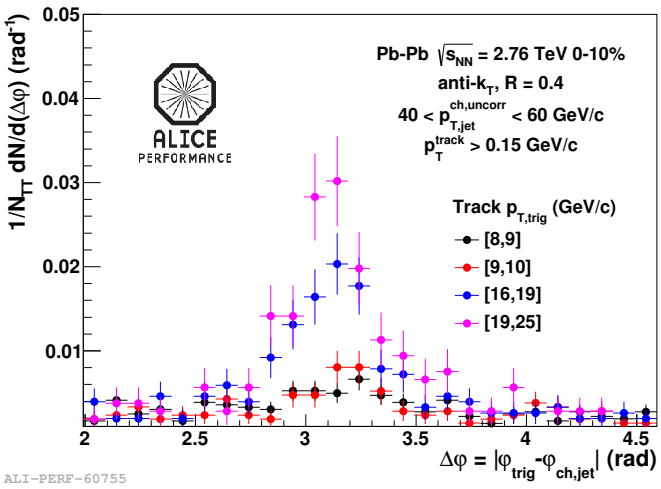

Figure 121: Azimuthal correlations between trigger tracks and recoil jets for four trigger classes: TT[8,9], TT[9,10], TT[16,19], TT[19,25] in the 0-10% most central Pb–Pb collisions.

jets of selected kinematics. The difference azimuthal correlations ($\Delta_{\text{recoil}}(\Delta\varphi)$) are shown in Fig. 122 for the choices of TT[16,19]-[8,9] and TT[19,25]-[9,10], respectively. A function

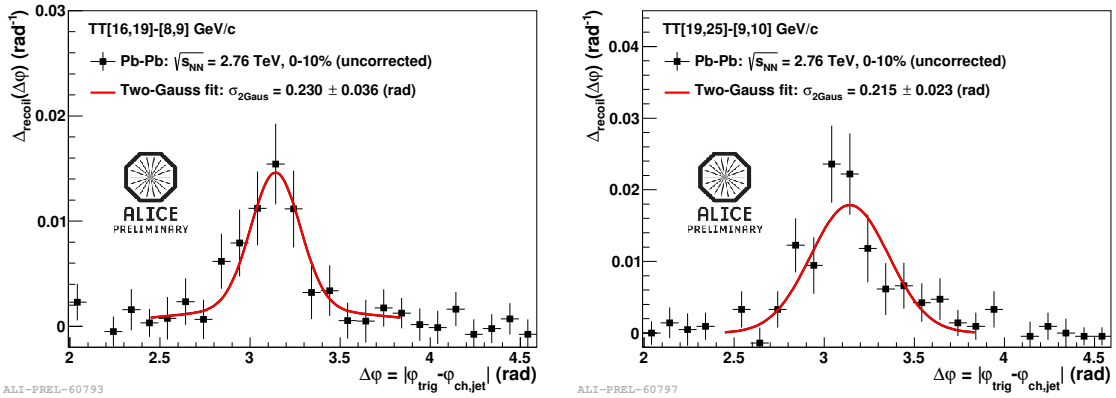

Figure 122: $\Delta_{\text{recoil}}(\Delta\varphi)$ distributions for the choices of TT[16,19]-[8,9] (left) and TT[19,25]-[9,10] (right) in the 0-10% most central Pb–Pb collisions (black points). A fit consisting of two Gaussian functions to the data is shown in red lines.

consisting of two Gaussian distributions centered at π is fitted to the data in the range $[\pi - 0.7, \pi + 0.7]$, and shown as the red lines in Fig. 122:

$$f(x) = a \times e^{(x-\pi)^2/2b^2} + c \times e^{(x-\pi)^2/2d^2} \tag{80}$$

The variance of the fitted function ($\sigma_{2\text{Gaus}}$) is used to quantify the width of the raw distributions. The statistical error on the variance is estimated as the following:

- Vary all the data points of the raw distributions independently and randomly within their respective errors.
- Fit the varied distribution with Eq. 80 and extract corresponding σ_{2Gaus}
- Repeat the above exercise 1000 times to obtain a distribution of σ_{2Gaus}
- Fit the σ_{2Gaus} distribution with a single Gaussian function, and use the standard deviation of the fitted Gaussian as the statistical error for σ_{2Gaus}

The resulting variances and their statistical errors are also listed in Fig. 122.

12.3 PYTHIA reference

Due to the limited statistics, unfolding the raw distributions (Fig. 122) to correct for background fluctuations and instrumental effects [114] is unreliable. We therefore fold detector effects and background fluctuations into the PYTHIA model (pp collisions) to build the references for comparison. PYTHIA events are propagated through a simulation of the detectors using GEANT under the same conditions[18] as the real data. After throwing away randomly 5% of reconstructed tracks to mimic the efficiency drop in Pb–Pb collisions due to the increased multiplicity, detecter-level PYTHIA events are then embedded into real Pb–Pb events to further incorporate background fluctuations. The resulting $\Delta_{\mathrm{recoil}}(\Delta\varphi)$ distributions after embedding are shown in Fig. 123 for the choices of TT[16,19]-[8,9] and TT[19,25]-[9,10]. The same approach in the analysis of the data is used to extract the widths of the distributions and the associated statistical errors.

12.4 Systematic uncertainties

Tracking efficiency: the jet axis is determined by all the constituents, but the tracking efficiency affects the fraction of the constituents that are measured. The uncertainty of the tracking efficiency is 5%, and its influence on the width of $\Delta_{\mathrm{recoil}}(\Delta\varphi)$ distribution is evaluated by comparing the $\Delta_{\mathrm{recoil}}(\Delta\varphi)$ distributions using detector-level PYTHIA events with three configurations: (i) throwing away 5% of tracks as default (Pb–Pb efficiency);

[18]The corresponding detector conditions are used for "GOOD" and "SEMIGOOD" runs, respectively.

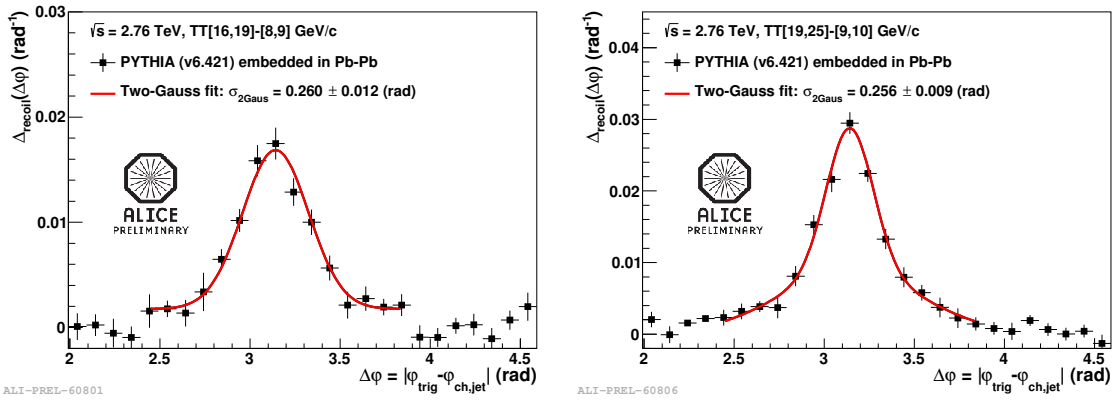

Figure 123: $\Delta_{\rm recoil}(\Delta\varphi)$ distributions for the choices of TT[16,19]-[8,9] (left) and TT[19,25]-[9,10] (right) using detector-level PYTHIA events embedded into the 0-10% most central Pb–Pb collisions (black points). A fit consisting of two Gaussian functions to the distributions is shown in red lines.

(ii) not throwing away any tracks (Pb–Pb efficiency + 5%); (iii) throwing away 10% of the tracks (Pb–Pb efficiency - 5%). To disentangle the statistical fluctuations and systematic effects, the exercise of throwing away tracks is repeated 50 times with a randomly different set of tracks discarded each time. The width difference of $\Delta_{\rm recoil}(\Delta\varphi)$ distribution for the above three configurations is taken as the systematic uncertainty.

Track $p_{\rm T}$ resolution: the $p_{\rm T}$ resolution of the tracks may also influence the determination of the jet axis, as the axis is calculated via a $p_{\rm T}$-weighted sum of (η,φ) of its constituents. Tracks in the detector-level PYTHIA events are smeared by an additional 100% of its original resolution, and the resulting variation on the width of $\Delta_{\rm recoil}(\Delta\varphi)$ distribution is taken as the uncertainty.

Track φ resolution: since we are studying the correlation between trigger hadrons and recoil jets in azimuth, the φ resolution of the charged tracks can affect both the trigger hadrons, which define "$\varphi = 0$" in the correlation, and the recoil jets. Jets are multiple-particle objects, so the effect of the φ resolution of a single track on the determination of the jet axis is reduced significantly. Therefore, the uncertainty due to the track φ resolution only enters through the determination of the trigger hadron φ. The uncertainty is estimated to be the difference of the φ resolution extracted from PYTHIA (pp) and HIJING (Pb–Pb) simulations.

Background density: the inclusive background density in the Pb–Pb events is used in the default analysis. The background density in the recoil region of high p_{T} trigger hadrons is about 1 GeV/c higher than the inclusive density due to the flow effects. However, this 1 GeV/c is probably an over-estimate since the influence of the true recoil jets is not completely taken away in the estimation. To assess the systematic uncertainty, the 1 GeV/c-higher background density is used instead, which effectively shifts the jet sample entering the azimuthal correlations due to the rigid kinematic cut on the recoil jets, and the entire analysis is repeated. The resulting difference in the width of the $\Delta_{\mathrm{recoil}}(\Delta\varphi)$ distribution is taken as the uncertainty.

Fitting function: the sensitivity to the choice of fitting functions is estimated by using a different one:

$$f(x) = p_0 \times e^{(x-\pi)^2/2p_2^2} + p_3 + p_4 \times (x-\pi)^2 \tag{81}$$

The resulting difference is taken as the uncertainty.

Fitting ranges: the fitting ranges are varied by ± 0.5 on both boundaries to check the effects on the width of $\Delta_{\mathrm{recoil}}(\Delta\varphi)$ distributions.

All the systematic uncertainties are summarized in Table 4, where the influences of the detector effects are seen to be negligible for this particular observable, partially because they are not corrected in the raw data. The total uncertainty is the quadrature sum of all the individual contributions assuming that the sources are independent.

Table 4: Systematic uncertainties for the width of $\Delta_{\mathrm{recoil}}(\Delta\varphi)$ distributions given on an absolute scale.

Sources of systematic uncertainties	TT[16,19]-[8,9]	TT[19,25]-[9,10]
Tracking efficiency	negligible	negligible
Track p_{T} resolution	negligible	negligible
Track φ resolution	negligible	negligible
Background density	0.023	0.011
Fitting function	0.001	0.025
Fitting range	0.013	0.015
Total uncertainty	0.026	0.031

12.5 Comparison between data and PYTHIA reference

A comparison for the widths of $\Delta_{\text{recoil}}(\Delta\varphi)$ distributions between data and PYTHIA references is shown in Fig. 124. The widths are seen to be consistent within statistical and

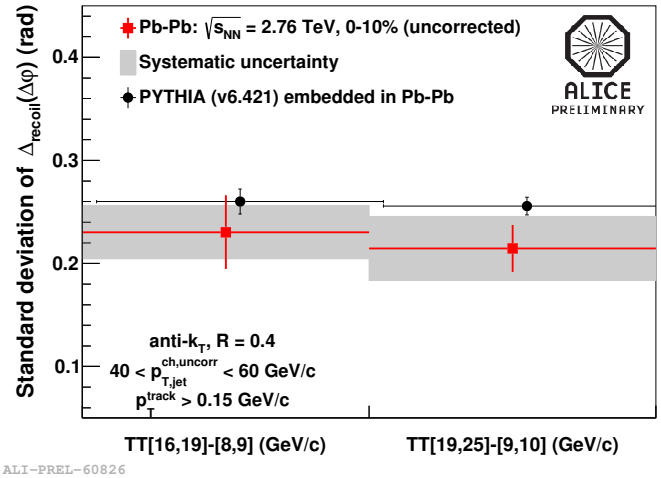

Figure 124: Width of $\Delta_{\text{recoil}}(\Delta\varphi)$ distributions from data (red square) and PYTHIA embedding (black circle). The error bars on the points are statistical, and the grey bands around the data points are the systematic uncertainties.

systematic uncertainties, implying that there is no medium-induced deflection of the jet axis for the selected kinematics. This is consistent with the mechanism that partons lose energy by radiating multiple relatively soft gluons [117]. However, this conclusion is weakened by the fact that the Q^2 processes sampled by the triggers in the same kinematic ranges are higher in Pb–Pb than in PYTHIA, due to the quenching effects on the jets that contain the triggers [118], which could lead to different underlying azimuthal correlations. To make a fair comparison between Pb–Pb and PYTHIA, one needs to select the same Q^2 processes sampled using different trigger kinematics, which of course requires guidance from models. The current analysis is limited by statistics, partially because of the selection of the "h+jet" configuration in certain kinematic ranges. Better precision in data is needed to make more conclusive statements. It is worth mentioning that this analysis serves nicely as a complementary study to the jet-jet and gamma-jet azimuthal correlation studies performed at higher jet energies, where no additional deflection of jet axis is observed in Pb–Pb collisions either [119, 120].

13 Summary & discussion

Jet quenching originates from the interactions between the hard partons and the dense medium through which the partons traverse. The essential nature of jet quenching is determined by the properties of the QGP, which still remains an open question, despite more than a decade of experimental exploration. Full jet reconstruction is a promising experimental approach to reconstruct the parton kinematics, study the quenching effects, and thus deduce the QGP properties.

The first measurement of the inclusive jet cross section in pp collisions at $\sqrt{s} = 2.76$ TeV using the ALICE detector is presented in this thesis. It serves as a proof-of-principle measurement that using only a tracking system and electromagnetic calorimetry can achieve a satisfactory level of uncertainties on the jet energy scale. When confronted with state-of-the-art pQCD calculations at NLO, the good agreement confirms that jets are well calibrated probes for use in heavy-ion collisions. The measurement is also an essential baseline for the same analysis performed in the more complex Pb–Pb system at the same $\sqrt{s_{\mathrm{NN}}}$ [110]. However, the inclusive jet measurement in Pb–Pb collisions turns out to be very challenging due to the presence of the overwhelming background, which renders the corrections to the raw jet spectrum quite difficult. Suppression of the combinatorial jets becomes necessary in such analyses. But the commonly employed techniques impose specific fragmentation biases or limit the kinematic range of the true hard jets while suppressing the background jets. A novel method is used in this thesis to remove the combinatorial jets by utilizing a subset of the total jet population that recoil from a high p_{T} hadron trigger. Specifically, the azimuthal correlations between trigger hadrons and recoil jets are built for signal (relatively high p_{T}) and reference (relatively low p_{T}) trigger classes. By taking the difference of the two azimuthal correlations, the contribution from the underlying background is taken out since it is uncorrelated with the trigger. The observable developed is actually an evolution of the azimuthal correlations with respect to the triggers. Compared to the PYTHIA reference, which approximates pp collisions, no medium-induced acoplanarity is observed for the selected kinematics within the current precision. It will be very insightful to check if the same conclusion holds for other choices of trigger hadrons and recoil jets, when more

data is available in the future. Nevertheless, a lot more analyses are needed to reveal a complete picture of the jet quenching mechanism.

How strong is the jet quenching? Preliminary analyses of $R_{\rm AA}$ for $R = 0.2$ jets from CMS and ALICE collaborations show that $R_{\rm AA} \sim 0.5$ above 100 GeV/c, and drops down to about 0.3 at 30 GeV/c [110, 121]. A theoretical calculation has successfully described the data by using $\hat{q} \sim 1 - 2$ GeV^2/fm [122]. Non-zero v_2 for $R = 0.2$ jets above 50 GeV/c is extracted by looking at the jet yield with respect to the reaction plane, which is interpreted as a result of the path-length dependence of the energy loss [123]. However, these analyses are limited by the small cone radius as well as certain fragmentation biases. Within the "h+jet" framework where the combinatorial jets are removed, the suppression of the recoil jet spectrum can be measured up to $R = 0.5$, and down to $p_{\rm T} \sim 20$ GeV/c. More interestingly, one can change the $p_{\rm T}$ interval of the trigger hadrons to alter the amount of surface bias introduced by the trigger, thus sampling different in-medium path lengths for the recoil jets. This provides an opportunity to study the jet quenching mechanism systematically in a controlled fashion.

How does the jet structure change in medium if any? Di-jet pairs originating from hard scatterings are expected to be balanced in momentum according to the conservation law. However, unbalanced di-jet pairs are observed in Pb–Pb collisions due to quenching effects. A close check of the energy flow in these events reveals that the lost energy is scattered to large angles relative to the jet axis in the form of low $p_{\rm T}$ hadrons [115]. Furthermore, jets seem not to be further deflected in the medium while suffering energy loss. A mechanism of radiating multiple relatively soft gluons is consistent with both large energy loss and mild deflection of jet axis [117]. By comparing the jet fragmentation in vacuum and medium within the jet cone, there seems to be slightly more particles at small z and more particles away from the jet centroid for jets above 100 GeV/c in heavy ion collisions [124, 125, 126]. It will be very interesting to check if this mild modification to jet structure still holds for jets at lower $p_{\rm T}$, where the ALICE collaboration is expected to make unique contributions due to its excellent tracking down to very low $p_{\rm T}$. As is the case for the $R_{\rm AA}$ measurements, these analyses suffer from certain biases when removing the underlying background. A systematically different approach to deal with the background

contribution in measuring the jet fragmentation is proposed in [127], which could shed new insight in the study of jet structure.

With the increase in the cross section of hard probes and the higher luminosity at the LHC, jet physics has progressed very rapidly since the LHC start-up in 2010, and provided insights into the QGP properties. Also jet physics at RHIC has gained more recent interest, since the techniques to deal with the underlying background have matured in the last few years. In the future, the hard sector of the heavy-ion physics should continue to make significant contributions in understanding the QGP with the complementary analyses from both RHIC and LHC.

Appendices

A Analysis setup for measurement of the jet cross section in pp collisions

- Event selection
  - Data set: lhc11a/pass4; without SDD in the reconstruction
  - Run list: 146746, 146747, 146748, 146801, 146802, 146803, 146804, 146805, 146806, 146807, 146817, 146824, 146856, 146858, 146859, 146860
  - Trigger selection: AliVEvent::kMB for MB events and AliVEvent::kEMC1 for EMCal triggered events. AliVEvent::kFastOnly is excluded.
  - List of masked TRU's for the EMCal trigger:
    * TRU SMC1RCU1B ($-0.7 < \eta < 0, 100^\circ < \varphi < 106.7^\circ$): the trigger information is missing even though this TRU seems to send valid triggers.
    * TRU SMA1RCU1A ($0 < \eta < 0.7, 106.7^\circ < \varphi < 113.3^\circ$): the TRU is not stable during most of the data taking period.
    * TRU SMA2RCU0B ($0.23 < \eta < 0.7, 120^\circ < \varphi < 126.7^\circ$): the event sequence is wrong, namely this TRU is processing signals from other events.
    * TRU SMA2RCU1A ($0 < \eta < 0.7, 126.7^\circ < \varphi < 133.3^\circ$): this TRU is not functioning during data taking.
  - Pile-up rejection: AliVEvent::IsPileupFromSPD()
  - Vertex cut: the primary vertex, with $|z| < 10$ cm, is required to have at least one contributor.
- Track selection
  - $p_{\mathrm{T}} > 0.15$ GeV/c
  - $|\eta| < 0.9$
  - Quality cuts for global tracks

        * SetRequireTPCStandAlone(kTRUE)
        * SetMinNClustersTPCPtDep(f1,20.); f1 = new TFormula("f1","70.+30./20.*x");
        * SetMaxChi2PerClusterTPC(4)
        * SetRequireTPCRefit(kTRUE)
        * SetMaxFractionSharedTPCClusters(0.4)
        * SetAcceptKinkDaughters(kFALSE)
        * SetRequireITSRefit(kTRUE)
        * SetMaxChi2PerClusterITS(36)
        * SetClusterRequirementITS(AliESDtrackCuts::kSPD, AliESDtrackCuts::kAny)
        * SetMaxDCAToVertexZ(3.0)
        * SetMaxDCAToVertexXY(2.4)
        * SetDCAToVertex2D(kTRUE)
        * SetMaxChi2TPCConstrainedGlobal(36)
        * SetRequireSigmaToVertex(kFALSE)
    - Quality cuts for complementary tracks: the same as for the global tracks, except the following two cuts are used:
        * SetRequireITSRefit(kFALSE)
        * SetClusterRequirementITS(AliESDtrackCuts::kSPD, AliESDtrackCuts::kNone)

- Cluster selection
    - Hot towers identified offline: 74, 103, 152, 917, 1059, 1175, 1276, 1288, 1376, 1382, 1595, 2022, 2026, 2210, 2540, 2778, 2793, 3135, 3764, 5767, 6481, 7371, 7878, 9769.
    - "v2" clusterizer
    - Tender is used to recalibrate EMCal clusters.
    - E > 0.3 GeV
    - $F_{\text{cross}} < 0.97$
    - Cluster energy is scaled up by 2% in the analysis after recalibration.

- Residual cuts for track matching: $|\Delta\varphi| < 0.03$, $|\Delta\eta| < 0.015$
- Hadronic correction with $f_{\mathrm{sub}} = 1$

- Jet finding
  - Anti-$\mathrm{k_T}$ algorithm
  - Recombination scheme: boost invariant p_{T} scheme (BIpt-scheme)
  - Resolution parameters: $R = 0.2$ and 0.4
  - $p_{\mathrm{T,jet}} > 20$ GeV/c
  - $|\eta_{\mathrm{jet}}| < 0.7 - R,\ 1.4 + R < \varphi_{\mathrm{jet}} < 3.14 - R$
  - $z_{\mathrm{leading}} < 0.98$

- Simulation production: lhc12a15a

B Analysis setup for hadron+jet coincidence measurement in Pb–Pb collisions

- Event selection
  - Data set: lhc11h/AOD115
  - Run list: 168311, 168322, 168325, 168341, 168361, 168362, 168458, 168460, 168461, 168992, 169091,169094, 169138, 169143, 169167, 169417, 169835, 169837, 169838, 169846, 169855, 169858, 169859, 169923, 169956, 170027, 170036, 170081, 167813, 167988, 168066, 168068, 168069, 168076, 168104, 168212, 169975, 169981, 170038, 170040, 170083, 170084, 170085, 170088, 170089, 170091, 170152, 170155, 170159, 170163, 170193, 170195, 170203, 170204, 170205, 170228, 170230, 170264, 170268, 170269, 170270, 170306, 170308, 170309.
  - Trigger and centrality: kMB+kCentral+kSemiCentral for 0-10% central events
  - Vertex cut: the primary vertex, with $|z| < 10$ cm, is required to have at least one contributor.

- Track selection

  - $p_{\mathrm{T}} > 0.15$ GeV/c
  - $|\eta| < 0.9$
  - Quality cuts for global tracks
    * SetMinNCrossedRowsTPC(70)
    * SetMinRatioCrossedRowsOverFindableClustersTPC(0.8)
    * SetMaxChi2PerClusterTPC(4)
    * SetRequireTPCRefit(kTRUE)
    * SetAcceptKinkDaughters(kFALSE)
    * SetRequireITSRefit(kTRUE)
    * SetMaxChi2PerClusterITS(36)
    * SetClusterRequirementITS(AliESDtrackCuts::kSPD, AliESDtrackCuts::kAny)
    * SetMaxDCAToVertexZ(3.2)
    * SetMaxDCAToVertexXY(2.4)
    * SetDCAToVertex2D(kTRUE)
    * SetMaxChi2TPCConstrainedGlobal(36)
    * SetRequireSigmaToVertex(kFALSE)
  - Quality cuts for complementary tracks: the same as for the global tracks, except the following cut is used:
    * SetClusterRequirementITS(AliESDtrackCuts::kSPD, AliESDtrackCuts::kNone)

- Jet finding
  - Anti-k_{T} algorithm
  - Recombination scheme: boost invariant p_{T} scheme (BIpt-scheme)
  - Resolution parameter: $R = 0.4$
  - $A_{\mathrm{jet}} > 0.4$

- Simulation production: lhc12a15e_fix

C Acronyms

AdS/CFT Anti-de Sitter/Conformal Field Theory. AdS/CFT is a duality between quantum field theory and quantum gravity.

AGS Alternating Gradient Synchrotron. AGS is located at BNL.

ALICE A Large Ion Collider Experiment.

APD Avalanche PhotoDiode.

ASW Armesto, Salgado and Wiedemann. They calculate the parton energy loss in the medium using quenching weights.

ATLAS A Toroidal LHC Apparatus

BDMPS Baier, Dokshitzer, Mueller, Peigne, and Schiff. They developed an energy loss mechanism for partons in the medium in terms of multiple soft scatterings.

BNL Brookhaven National Laboratory.

CERN European Organization for Nuclear Research.

CMS Compact Muon Solenoid.

DAQ Data Acquisition.

DCA Distance of Closest Approach.

DGLAP Dokshitzer, Gribov, Landau, Alterelli, and Parisi. DGLAP equations are the QCD evolution equations.

EMCal ElectroMagnetic Calorimeter. Photons and electrons are measured and identified in the EMCal at mid-rapidity.

FF Fragmentation Function. FF governs the parton fragmentation pattern.

FMD Forward Multiplicity Detector. FMD measures charged-particle multiplicity in the pseudo-rapidity ranges $-3.4 < \eta < -1.7$ and $1.7 < \eta < 5.1$.

HBT Hanbury Brown and Twiss. HBT correlations are the correlation effects in intensity.

HERWIG Hadron Emission Reactions With Interfering Gluons. HERWIG is a general-purpose particle physics event generator.

HIJING Heavy Ion Jet INteraction Generator. HIJING is an event generator for heavy-ion collisions.

HMPID High-Momentum Particle Identification Detector. HMPID is designed to identify hadrons above 1 GeV/c at mid-rapidity.

IC Iterative Cone jet algorithm.

IC-PR Iterative Cone-Progressive Removal jet algorithm.

IC-SM Iterative Cone-Split Merge jet algorithm.

IP Interaction Point. IP is located at the center of the ALICE detector.

IRC InfraRed and Collinear. IRC safety is a fundamental requirement for jet algorithms.

ITS Inner Tracking System. ITS consists of six layers of silicon detectors at mid-rapidity, and is used to reconstruct collision vertex and measure the trajectory of charged particles.

JER Jet Energy Resolution.

JES Jet Energy Scale. JES is equivalent to jet energy or jet p_{T}.

LED Light-Emitting Diode.

LEIR Low Energy Ion Ring. LEIR is specifically built to process ion beams at CERN.

LEP Large Electron-Positron collider.

LHC Large Hadron Collider. LHC is located at CERN.

LHCb Large Hadron Collider beauty

LINAC Linear accelerator.

LO Leading-Order.

LQCD Lattice Quantum ChromoDynamics. LQCD is a non-perturbative approach to solve the strong interactions.

MC Monte Carlo.

MIP Minimum Ionizing Particle. A MIP deposits minimum energy in matter.

MWPC Multiple Wire Proportional Chambers. MWPC is used for the TPC readout.

NEF Neutral Energy Fraction. NEF is the fraction of the jet energy carried by the EMCal clusters.

NLO Next-to-Leading Order.

PDF Parton Distribution Function. PDF is the distribution of partons in a nucleus in terms of momentum fraction. It can be measured in deep inelastic scattering.

PHOS PHOton Spectrometer. PHOS is a high-resolution electromagnetic spectrometer at mid-rapidity.

PMD Photon Multiplicity Detector. PMD measures the multiplicity and spatial distribution of photons in the range $2.3 < \eta < 3.5$.

pQCD perturbative QCD. QCD becomes perturbative at high energies.

PS Proton Synchrotron.

PS Booster Proton Synchrotron booster.

QCD Quantum ChromoDynamics. QCD is the fundamental theory for strong interactions.

QD Defocusing Quadrupole. A QD focuses the beam horizontally, but defocuses the beam vertically.

QED Quantum ElectroDynamics. QED is the theory for electromagnetic interactions.

QF Focusing Quadrupole. A QF defocuses the beam horizontally, but focuses the beam vertically.

QGP Quark Gluon Plasma. QGP is a new state of matter created in heavy ion collisions.

RF Radio Frequency. RF system is used to accelerate particles.

RHIC Relativistic Heavy Ion Collider. RHIC is located at BNL.

SDD Silicon Drift Detector. SDD comprises the intermediate two layers of the ITS.

SISCone Seedless Infrared-Safe Cone jet algorithm

SM Super Module. A SM in the EMCal consists of 1152 towers.

SPD Silicon Pixel Detector. SPD comprises the inner two layers of the ITS.

SPS Super Proton Synchrotron. SPS is located at CERN.

SSD Silicon Strip Detector. SSD comprises the outer two layers of the ITS.

SSh Single Shower. The EMCal SSh trigger checks for the energy deposition of the overlapping groups of 4×4 adjacent towers.

T0 T0 covers $-5 < \eta < -4.5$ and $2.9 < \eta < 3.3$, and measures the starting time of a collision.

TOF Time-Of-Flight. TOF is used to measure the time-of-flight of particles at mid-rapidity.

TPC Time Projection Chamber. TPC is a gaseous three-dimensional tracking chamber at mid-rapidity measuring the trajectory of charged particles.

TRD Transition Radiation Detector. TRD is mainly used to identify electrons above 1 GeV/c at mid-rapidity.

TRU Trigger Region Units. TRU is used to process the EMCal trigger.

UE Underlying Event. UE refers to the soft processes in the collision.

VZERO VZERO covers $2.8 < \eta < 5.1$ and $-3.7 < \eta < -1.7$, and is mainly used to provide interaction triggers and measure centralities of heavy-ion collisions.

ZDC Zero-Degree Calorimeter. ZDC detects the spectator neutrons at zero degrees.

References

[1] M. E. Peskin and D. V. Schroeder, *An Introduction To Quantum Field Theory.* Westview Press, 1995.

[2] S. B. Ruester, V. Werth, M. Buballa, I. A. Shovkovy, and D. H. Rischke, "The Phase diagram of neutral quark matter: Self-consistent treatment of quark masses," *Phys.Rev.* **D72** (2005) 034004, arXiv:hep-ph/0503184 [hep-ph].

[3] S. Hands, "The Phase diagram of QCD," *Contemp.Phys.* **42** (2001) 209–225, arXiv:physics/0105022 [physics.ed-ph].

[4] F. Karsch, "The Phase transition to the quark gluon plasma: Recent results from lattice calculations," *Nucl.Phys.* **A590** (1995) 367C–382C, arXiv:hep-lat/9503010 [hep-lat].

[5] R. Stock, "The Parton hadron phase transition in central nuclear collisions at the CERN SPS," *Prog.Part.Nucl.Phys.* **42** (1999) 295–309, arXiv:hep-ph/9901415 [hep-ph].

[6] R. Stock, "Relativistic Nucleus-Nucleus Collisions and the QCD Matter Phase Diagram," arXiv:0807.1610 [nucl-ex].

[7] **STAR** Collaboration, J. Adams *et al.*, "Experimental and theoretical challenges in the search for the quark gluon plasma: The STAR Collaboration's critical assessment of the evidence from RHIC collisions," *Nucl.Phys.* **A757** (2005) 102–183, arXiv:nucl-ex/0501009 [nucl-ex].

[8] J. Bjorken, "Highly Relativistic Nucleus-Nucleus Collisions: The Central Rapidity Region," *Phys.Rev.* **D27** (1983) 140–151.

[9] **ALICE** Collaboration, B. Abelev *et al.*, "Centrality determination of Pb-Pb collisions at sqrt(sNN) = 2.76 TeV with ALICE," *Phys.Rev.* **C88** (2013) 044909, arXiv:1301.4361 [nucl-ex].

[10] **ALICE** Collaboration, K. Aamodt *et al.*, "Charged-particle multiplicity density at mid-rapidity in central Pb-Pb collisions at $\sqrt{s_{NN}} = 2.76$ TeV," *Phys.Rev.Lett.* **105** (2010) 252301, arXiv:1011.3916 [nucl-ex].

[11] B. Alver, M. Baker, C. Loizides, and P. Steinberg, "The PHOBOS Glauber Monte Carlo," arXiv:0805.4411 [nucl-ex].

[12] P. Stankus, "Direct photon production in relativistic heavy-ion collisions," *Ann.Rev.Nucl.Part.Sci.* **55** (2005) 517–554.

[13] ALICE Collaboration, "Measurement of direct photons in pp at 7 TeV and in Pb-Pb at 2.76 TeV via Conversions,". https://aliceinfo.cern.ch/Notes/node/87.

[14] S. Voloshin and Y. Zhang, "Flow study in relativistic nuclear collisions by Fourier expansion of Azimuthal particle distributions," *Z.Phys.* **C70** (1996) 665–672, arXiv:hep-ph/9407282 [hep-ph].

[15] **ALICE** Collaboration, K. Aamodt *et al.*, "Elliptic flow of charged particles in Pb-Pb collisions at 2.76 TeV," *Phys.Rev.Lett.* **105** (2010) 252302, arXiv:1011.3914 [nucl-ex].

[16] P. Kovtun, D. Son, and A. Starinets, "Viscosity in strongly interacting quantum field theories from black hole physics," *Phys.Rev.Lett.* **94** (2005) 111601, arXiv:hep-th/0405231 [hep-th].

[17] B. Schenke, S. Jeon, and C. Gale, "Anisotropic flow in $\sqrt{s} = 2.76$ TeV Pb+Pb collisions at the LHC," *Phys.Lett.* **B702** (2011) 59–63, arXiv:1102.0575 [hep-ph].

[18] Z. Qiu, C. Shen, and U. Heinz, "Hydrodynamic elliptic and triangular flow in Pb-Pb collisions at $\sqrt{s} = 2.76$ATeV," *Phys.Lett.* **B707** (2012) 151–155, arXiv:1110.3033 [nucl-th].

[19] B. Alver and G. Roland, "Collision geometry fluctuations and triangular flow in heavy-ion collisions," *Phys.Rev.* **C81** (2010) 054905, arXiv:1003.0194 [nucl-th].

[20] **ALICE** Collaboration, K. Aamodt *et al.*, "Harmonic decomposition of two-particle angular correlations in Pb-Pb collisions at $\sqrt{s_{NN}} = 2.76$ TeV," *Phys.Lett.* **B708** (2012) 249–264, arXiv:1109.2501 [nucl-ex].

[21] P. Braun-Munzinger, K. Redlich, and J. Stachel, "Particle production in heavy ion collisions," arXiv:nucl-th/0304013 [nucl-th].

[22] ALICE Collaboration, "A thermal fit of alice hadron yields,". https://aliceinfo.cern.ch/Notes/node/98.

[23] E. Schnedermann, J. Sollfrank, and U. W. Heinz, "Thermal phenomenology of hadrons from 200-A/GeV S+S collisions," *Phys.Rev.* **C48** (1993) 2462–2475, arXiv:nucl-th/9307020 [nucl-th].

[24] U. W. Heinz, "Concepts of heavy ion physics," arXiv:hep-ph/0407360 [hep-ph].

[25] **ALICE** Collaboration, B. Abelev *et al.*, "Pion, Kaon, and Proton Production in Central Pb–Pb Collisions at $\sqrt{s_{NN}} = 2.76$ TeV," *Phys.Rev.Lett.* **109** (2012) 252301, arXiv:1208.1974 [hep-ex].

[26] **ALICE** Collaboration, B. Abelev *et al.*, "Centrality dependence of π, K, p production in Pb-Pb collisions at $\sqrt{s_{NN}} = 2.76$ TeV," arXiv:1303.0737 [hep-ex].

[27] M. A. Lisa, S. Pratt, R. Soltz, and U. Wiedemann, "Femtoscopy in relativistic heavy ion collisions," *Ann.Rev.Nucl.Part.Sci.* **55** (2005) 357–402, arXiv:nucl-ex/0505014 [nucl-ex].

[28] **ALICE** Collaboration, K. Aamodt *et al.*, "Two-pion Bose-Einstein correlations in central Pb-Pb collisions at $sqrt(s_N N) = 2.76$ TeV," *Phys.Lett.* **B696** (2011) 328–337, arXiv:1012.4035 [nucl-ex].

[29] **PHENIX** Collaboration, S. Adler *et al.*, "Systematic studies of the centrality and s(NN)**(1/2) dependence of the d E(T) / d eta and d (N(ch) / d eta in heavy ion collisions at mid-rapidity," *Phys.Rev.* **C71** (2005) 034908, arXiv:nucl-ex/0409015 [nucl-ex].

[30] **PHENIX** Collaboration, A. Adare *et al.*, "Enhanced production of direct photons in Au+Au collisions at $\sqrt{s_{NN}} = 200$ GeV and implications for the initial temperature," *Phys.Rev.Lett.* **104** (2010) 132301, arXiv:0804.4168 [nucl-ex].

[31] **STAR** Collaboration, B. Abelev *et al.*, "Centrality dependence of charged hadron and strange hadron elliptic flow from s(NN)**(1/2) = 200-GeV Au + Au collisions," *Phys.Rev.* **C77** (2008) 054901, arXiv:0801.3466 [nucl-ex].

[32] **STAR** Collaboration, J. Adams *et al.*, "Identified particle distributions in pp and Au+Au collisions at s(NN)**(1/2) = 200 GeV," *Phys.Rev.Lett.* **92** (2004) 112301, arXiv:nucl-ex/0310004 [nucl-ex].

[33] **STAR** Collaboration, B. Abelev *et al.*, "Pion Interferometry in Au+Au and Cu+Cu Collisions at RHIC," *Phys.Rev.* **C80** (2009) 024905, arXiv:0903.1296 [nucl-ex].

[34] **ALICE** Collaboration, K. Aamodt *et al.*, "The ALICE experiment at the CERN LHC," *JINST* **3** (2008) S08002.

[35] **ALICE** Collaboration, B. Abelev *et al.*, "Measurement of the inclusive differential jet cross section in *pp* collisions at $\sqrt{s} = 2.76$ TeV," *Phys.Lett.* **B722** (2013) 262–272, arXiv:1301.3475 [nucl-ex].

[36] G. de Barros, B. Fenton-Olsen, P. Jacobs, and M. Ploskon, "Data-driven analysis methods for the measurement of reconstructed jets in heavyion collisions at RHIC and LHC," arXiv:1208.1518 [hep-ex].

[37] S. Bethke, "α_s 2002," *Nucl.Phys.Proc.Suppl.* **121** (2003) 74–81, arXiv:hep-ex/0211012 [hep-ex].

[38] J. C. Collins, D. E. Soper, and G. F. Sterman, "Factorization of Hard Processes in QCD," *Adv.Ser.Direct.High Energy Phys.* **5** (1988) 1–91, arXiv:hep-ph/0409313 [hep-ph].

[39] R. Placakyte, "Parton Distribution Functions," arXiv:1111.5452 [hep-ph].

[40] V. Gribov and L. Lipatov, "Deep inelastic e p scattering in perturbation theory," *Sov.J.Nucl.Phys.* **15** (1972) 438–450.

[41] Y. L. Dokshitzer, "Calculation of the Structure Functions for Deep Inelastic Scattering and e+ e- Annihilation by Perturbation Theory in Quantum Chromodynamics.," *Sov.Phys.JETP* **46** (1977) 641–653.

[42] G. Altarelli and G. Parisi, "Asymptotic Freedom in Parton Language," *Nucl.Phys.* **B126** (1977) 298.

[43] N. Armesto, "Nuclear shadowing," *J.Phys.* **G32** (2006) R367–R394, arXiv:hep-ph/0604108 [hep-ph].

[44] S. Peigne and A. Peshier, "Collisional energy loss of a fast heavy quark in a quark-gluon plasma," *Phys.Rev.* **D77** (2008) 114017, arXiv:0802.4364 [hep-ph].

[45] R. Baier, Y. L. Dokshitzer, A. H. Mueller, S. Peigne, and D. Schiff, "Radiative energy loss of high-energy quarks and gluons in a finite volume quark - gluon plasma," *Nucl.Phys.* **B483** (1997) 291–320, arXiv:hep-ph/9607355 [hep-ph].

[46] D. d'Enterria, "Jet quenching," arXiv:0902.2011 [nucl-ex].

[47] C. A. Salgado and U. A. Wiedemann, "Calculating quenching weights," *Phys.Rev.* **D68** (2003) 014008, arXiv:hep-ph/0302184 [hep-ph].

[48] G. P. Salam, "Towards Jetography," *Eur.Phys.J.* **C67** (2010) 637–686, arXiv:0906.1833 [hep-ph].

[49] G. F. Sterman and S. Weinberg, "Jets from Quantum Chromodynamics," *Phys.Rev.Lett.* **39** (1977) 1436.

[50] G. L. Bayatian *et al.*, "Cms physics: Technical design report," Tech. Rep. CMS-TRD-008-1, CERN, Geneva, 2006.

[51] M. Cacciari, G. P. Salam, and G. Soyez, "The Anti-k(t) jet clustering algorithm," *JHEP* **0804** (2008) 063, arXiv:0802.1189 [hep-ph].

[52] G. C. Blazey, J. R. Dittmann, S. D. Ellis, V. D. Elvira, K. Frame, *et al.*, "Run II jet physics," arXiv:hep-ex/0005012 [hep-ex].

[53] M. Seymour, "Jet shapes in hadron collisions: Higher orders, resummation and hadronization," *Nucl.Phys.* **B513** (1998) 269–300, arXiv:hep-ph/9707338 [hep-ph].

[54] G. P. Salam and G. Soyez, "A Practical Seedless Infrared-Safe Cone jet algorithm," *JHEP* **0705** (2007) 086, arXiv:0704.0292 [hep-ph].

[55] S. Catani, Y. L. Dokshitzer, M. Seymour, and B. Webber, "Longitudinally invariant K_t clustering algorithms for hadron hadron collisions," *Nucl.Phys.* **B406** (1993) 187–224.

[56] Y. L. Dokshitzer, G. Leder, S. Moretti, and B. Webber, "Better jet clustering algorithms," *JHEP* **9708** (1997) 001, arXiv:hep-ph/9707323 [hep-ph].

[57] M. Wobisch and T. Wengler, "Hadronization corrections to jet cross-sections in deep inelastic scattering," arXiv:hep-ph/9907280 [hep-ph].

[58] **ATLAS** Collaboration, G. Aad *et al.*, "Measurement of the inclusive jet cross section in pp collisions at $\sqrt{s}$=2.76 TeV and comparison to the inclusive jet cross section at $\sqrt{s}$=7 TeV using the ATLAS detector," arXiv:1304.4739 [hep-ex].

[59] **ATLAS** Collaboration, G. Aad *et al.*, "Measurement of inclusive jet and dijet production in *pp* collisions at $\sqrt{s} = 7$ TeV using the ATLAS detector," *Phys.Rev.* **D86** (2012) 014022, arXiv:1112.6297 [hep-ex].

[60] **CMS** Collaboration, S. Chatrchyan *et al.*, "Measurement of the Inclusive Jet Cross Section in *pp* Collisions at $\sqrt{s} = 7$ TeV," *Phys.Rev.Lett.* **107** (2011) 132001, arXiv:1106.0208 [hep-ex].

[61] M. Cacciari, G. P. Salam, and G. Soyez, "FastJet User Manual," *Eur.Phys.J.* **C72** (2012) 1896, arXiv:1111.6097 [hep-ph].

[62] M. Cacciari and G. P. Salam, "Dispelling the N^3 myth for the k_t jet-finder," *Phys.Lett.* **B641** (2006) 57–61, arXiv:hep-ph/0512210 [hep-ph].

[63] **CMS** Collaboration, S. Chatrchyan *et al.*, "The CMS experiment at the CERN LHC," *JINST* **3** (2008) S08004.

[64] **ATLAS** Collaboration, G. Aad *et al.*, "The ATLAS Experiment at the CERN Large Hadron Collider," *JINST* **3** (2008) S08003.

[65] **LHCb** Collaboration, J. Alves, A. Augusto *et al.*, "The LHCb Detector at the LHC," *JINST* **3** (2008) S08005.

[66] CERN. http://lhc-machine-outreach.web.cern.ch/lhc-machine-outreach/images/lhc-schematic.jpg.

[67] O. S. Brning, P. Collier, P. Lebrun, S. Myers, R. Ostojic, J. Poole, and P. Proudlock, *LHC Design Report.* CERN, Geneva, 2004.

[68] S. Baird, "Accelerators for pedestrians," Tech. Rep. CERN-AB-Note-2007-014, CERN, Geneva, Feb, 2007.

[69] D. W. Kerst and R. Serber, "Electronic orbits in the induction accelerator," *Phys. Rev.* **60** (Jul, 1941) 53–58.

[70] **ALICE** Collaboration, K. Aamodt *et al.*, "Rapidity and transverse momentum dependence of inclusive J/psi production in pp collisions at $\sqrt{s} = 7$ TeV," *Phys.Lett.* **B704** (2011) 442–455, arXiv:1105.0380 [hep-ex].

[71] **ALICE** Collaboration, K. Aamodt *et al.*, "Alignment of the ALICE Inner Tracking System with cosmic-ray tracks," *JINST* **5** (2010) P03003, arXiv:1001.0502 [physics.ins-det].

[72] J. Alme, Y. Andres, H. Appelshauser, S. Bablok, N. Bialas, *et al.*, "The ALICE TPC, a large 3-dimensional tracking device with fast readout for ultra-high multiplicity events," *Nucl.Instrum.Meth.* **A622** (2010) 316–367, arXiv:1001.1950 [physics.ins-det].

[73] **ALICE** Collaboration, M. Kweon, "The Transition Radiation Detector for ALICE at LHC," *Nucl.Phys.* **A830** (2009) 535–538, arXiv:0907.3380 [nucl-ex].

[74] A. Akindinov, A. Alici, A. Agostinelli, P. Antonioli, S. Arcelli, *et al.*, "Performance of the ALICE Time-Of-Flight detector at the LHC," *Eur.Phys.J.Plus* **128** (2013) 44.

[75] **ALICE** Collaboration, G. De Cataldo, "The high momentum particle identification detector in ALICE at LHC," *Nucl.Phys.Proc.Suppl.* **177-178** (2008) 273–275.

[76] **ALICE** Collaboration, G. Dellacasa *et al.*, "ALICE technical design report of the photon spectrometer (PHOS)," Tech. Rep. CERN-LHCC-99-04, 1999.

[77] P. Cortese *et al.*, "Alice electromagnetic calorimeter technical design report," Tech. Rep. ALICE-TDR-14, CERN, Geneva, Aug, 2008.

[78] **ALICE EMCal** Collaboration, J. Allen *et al.*, "Performance of prototypes for the ALICE electromagnetic calorimeter," *Nucl.Instrum.Meth.* **A615** (2010) 6–13, arXiv:0912.2005 [physics.ins-det].

[79] C. H. Christensen, J. J. Gaardhoje, K. Gulbrandsen, B. S. Nielsen, and C. Sogaard, "The ALICE Forward Multiplicity Detector," *Int.J.Mod.Phys.* **E16** (2007) 2432–2437, arXiv:0712.1117 [nucl-ex].

[80] ALICE Collaboration, *ALICE Photon Multiplicity Detector (PMD): Technical Design Report*. CERN, Geneva, 1999.

[81] P. Cortese *et al.*, *ALICE forward detectors: FMD, TO and VO: Technical Design Report*. CERN, Geneva, 2004.

[82] M. Gallio, W. Klempt, L. Leistam, J. De Groot, and J. Schkraft, *ALICE Zero-Degree Calorimeter (ZDC): Technical Design Report*. CERN, Geneva, 1999.

[83] **ALICE** Collaboration, A. Rashevsky *et al.*, "Characteristics of the ALICE silicon drift detector," *Nucl.Instrum.Meth.* **A461** (2001) 133–138.

[84] A. Boucham *et al.*, "Performances of double-sided ssds in high multiplicity environment of alice," Tech. Rep. ALICE-INT-1999-53, CERN, Geneva, 2000.

[85] C. Caso *et al.*, "Review of Particle Physics," *The European Physical Journal C - Particles and Fields* **3** (1998) 1–783.

[86] F. Sauli, "Principles of operation of multiwire proportional and drift chambers," CERN, Geneva, 1977.

[87] S. Palestini, G. Barr, A. Ceccucci, J. Cogan, D. Cundy, *et al.*, "Space charge in ionization detectors and the NA48 electromagnetic calorimeter," *Nucl.Instrum.Meth.* **A421** (1999) 75–89.

[88] **Particle Data Group** Collaboration, J. Beringer *et al.*, "Review of Particle Physics (RPP)," *Phys.Rev.* **D86** (2012) 010001.

[89] **Particle Data Group** Collaboration, R. L. Kelly *et al.*, "Review of particle properties," *Rev. Mod. Phys.* **52** (1980) 1–286.

[90] E. Longo and I. Sestili, "Monte carlo calculation of photon-initiated electromagnetic showers in lead glass," *Nucl.Instrum.Meth.* **128** (1975) 283 – 307.

[91] G. Bathow, E. Freytag, M. Koebberling, K. Tesch, and R. Kajikawa, "Measurements of the longitudinal and lateral development of electromagnetic cascades in lead, copper and aluminum at 6 gev," *Nucl.Phys.* **B20** (1970) 592–602.

[92] C. W. Fabjan and F. Gianotti, "Calorimetry for particle physics," *Rev. Mod. Phys.* **75** (2003) 1243–1286.

[93] R. Fruhwirth, "Application of Kalman filtering to track and vertex fitting," *Nucl.Instrum.Meth.* **A262** (1987) 444–450.

[94] **ALICE** Collaboration, G. Alessandro *et al.*, "ALICE: Physics performance report, volume II," *J.Phys.* **G32** (2006) 1295–2040.

[95] T. Sjostrand, S. Mrenna, and P. Z. Skands, "PYTHIA 6.4 Physics and Manual," *JHEP* **0605** (2006) 026, `arXiv:hep-ph/0603175 [hep-ph]`.

[96] R. Brun, F. Bruyant, M. Maire, A.C. McPherson, and P. Zanarini, "GEANT3 User Guide," *CERN Data Handling Division DD/EE/84-1* (1985) .

[97] CMS Collaboration, "Commissioning of the Particle-Flow reconstruction in Minimum-Bias and Jet Events from pp Collisions at 7 TeV," *CMS-PAS-PFT-10-002* (2010) .

[98] G. Cowan, "A Survey of Unfolding Methods for Particle Physics," *Proc. Advanced Statistical Techniques in Particle Physics, Durham* (2002) .

[99] **CDF** Collaboration, A. Cruz *et al.*, "Using MAX/MIN Transverse Regions to Study the Underlying Event in Run 2 at the Tevatron," *CDF/ANAL/CDF/CDFR/7703* (2005) .

[100] G. D'Agostini, "A Multidimensional unfolding method based on Bayes' theorem," *Nucl.Instrum.Meth.* **A362** (1995) 487–498.

[101] **ALICE** Collaboration, B. Abelev *et al.*, "Measurement of inelastic, single- and double-diffraction cross sections in proton–proton collisions at the LHC with ALICE," *Eur.Phys.J.* **C73** (2013) 2456, `arXiv:1208.4968 [hep-ex]`.

[102] S. Frixione, Z. Kunszt, and A. Signer, "Three jet cross-sections to next-to-leading order," *Nucl.Phys.* **B467** (1996) 399–442, `arXiv:hep-ph/9512328 [hep-ph]`.

[103] S. Frixione, "A General approach to jet cross-sections in QCD," *Nucl.Phys.* **B507** (1997) 295–314, `arXiv:hep-ph/9706545 [hep-ph]`.

[104] N. Armesto *Private communication. Calculations based on [102, 103]* (2012) .

[105] A. Martin, W. Stirling, R. Thorne, and G. Watt, "Parton distributions for the LHC," *Eur.Phys.J.* **C63** (2009) 189–285, `arXiv:0901.0002 [hep-ph]`.

[106] P. M. Nadolsky, H.-L. Lai, Q.-H. Cao, J. Huston, J. Pumplin, *et al.*, "Implications of CTEQ global analysis for collider observables," *Phys.Rev.* **D78** (2008) 013004, `arXiv:0802.0007 [hep-ph]`.

[107] G. Soyez, "A Simple description of jet cross-section ratios," *Phys.Lett.* **B698** (2011) 59–62, `arXiv:1101.2665 [hep-ph]`.

[108] **CDF** Collaboration, T. Aaltonen *et al.*, "Measurement of the Inclusive Jet Cross Section at the Fermilab Tevatron p anti-p Collider Using a Cone-Based Jet Algorithm," *Phys.Rev.* **D78** (2008) 052006, arXiv:0807.2204 [hep-ex].

[109] **D0** Collaboration, V. Abazov *et al.*, "Measurement of the inclusive jet cross-section in $p\bar{p}$ collisions at $\sqrt{s}$ =1.96 TeV," *Phys.Rev.Lett.* **101** (2008) 062001, arXiv:0802.2400 [hep-ex].

[110] ALICE Collaboration, "Fully Reconstructed Jets in$\sqrt{s_{NN}} = 2.76$ TeV Pb-Pb Collisions,". https://aliceinfo.cern.ch/Notes/node/100.

[111] M. Cacciari and G. P. Salam, "Pileup subtraction using jet areas," *Phys.Lett.* **B659** (2008) 119–126, arXiv:0707.1378 [hep-ph].

[112] **STAR** Collaboration, P. Jacobs, "Background Fluctuations in Heavy Ion Jet Reconstruction," arXiv:1012.2406 [nucl-ex].

[113] **ALICE** Collaboration, B. Abelev *et al.*, "Measurement of Event Background Fluctuations for Charged Particle Jet Reconstruction in Pb-Pb collisions at $\sqrt{s_{NN}} = 2.76$ TeV," *JHEP* **1203** (2012) 053, arXiv:1201.2423 [hep-ex].

[114] **ALICE** Collaboration, B. Abelev *et al.*, "Measurement of charged jet suppression n Pb-Pb collisions at sqrt(sNN)=2.76TeV," arXiv:1311.0633 [nucl-ex].

[115] **CMS** Collaboration, S. Chatrchyan *et al.*, "Observation and studies of jet quenching in PbPb collisions at nucleon-nucleon center-of-mass energy = 2.76 TeV," *Phys.Rev.* **C84** (2011) 024906, arXiv:1102.1957 [nucl-ex].

[116] T. Renk, "Energy dependence of the dijet imbalance in Pb-Pb collisions at 2.76 ATeV," *Phys.Rev.* **C86** (2012) 061901, arXiv:1204.5572 [hep-ph].

[117] J. Casalderrey-Solana, J. G. Milhano, and U. A. Wiedemann, "Jet Quenching via Jet Collimation," *J.Phys.* **G38** (2011) 035006, arXiv:1012.0745 [hep-ph].

[118] **ALICE** Collaboration, K. Aamodt *et al.*, "Particle-yield modification in jet-like azimuthal di-hadron correlations in Pb-Pb collisions at $\sqrt{s_{NN}} = 2.76$ TeV," *Phys.Rev.Lett.* **108** (2012) 092301, arXiv:1110.0121 [nucl-ex].

[119] **CMS** Collaboration, S. Chatrchyan *et al.*, "Jet momentum dependence of jet quenching in PbPb collisions at $\sqrt{s_{NN}} = 2.76$ TeV," *Phys.Lett.* **B712** (2012) 176–197, arXiv:1202.5022 [nucl-ex].

[120] **CMS** Collaboration, S. Chatrchyan *et al.*, "Studies of jet quenching using isolated-photon+jet correlations in PbPb and *pp* collisions at $\sqrt{s_{NN}} = 2.76$ TeV," *Phys.Lett.* **B718** (2013) 773–794, arXiv:1205.0206 [nucl-ex].

[121] CMS Collaboration, "Nuclear modification factor of high transverse momentum jets in PbPb collisions at sqrt(sNN) = 2.76 TeV," *CMS-PAS-HIN-12-004* (2012) .

[122] K. Tywoniuk, "2013 International Conference on the Initial Stages in High-Energy Nuclear Collisions,".

[123] **ATLAS** Collaboration, G. Aad *et al.*, "Measurement of the Azimuthal Angle Dependence of Inclusive Jet Yields in Pb+Pb Collisions at $\sqrt{s_{NN}}$= 2.76 TeV with the ATLAS detector," *Phys.Rev.Lett.* **111** (2013) 152301, arXiv:1306.6469 [hep-ex].

[124] **CMS** Collaboration, S. Chatrchyan *et al.*, "Modification of jet shapes in PbPb collisions at $\sqrt{s_{NN}} = 2.76$ TeV," arXiv:1310.0878 [nucl-ex].

[125] **ATLAS** Collaboration, "Measurement of inclusive jet charged particle fragmentation functions in Pb+Pb collisions at sqrt(s(nn)) = 2.76 TeV with the ATLAS detector," *ATLAS-CONF-2012-115, ATLAS-COM-CONF-2012-159* (2012) .

[126] CMS Collaboration, "Detailed Characterization of Jets in Heavy Ion Collisions Using Jet Shapes and Jet Fragmentation Functions," *CMS-PAS-HIN-12-013* (2012) .

[127] M. Cacciari, P. Quiroga-Arias, G. P. Salam, and G. Soyez, "Jet Fragmentation Function Moments in Heavy Ion Collisions," *Eur.Phys.J.* **C73** (2013) 2319, arXiv:1209.6086 [hep-ph].